NUREG/CR-1978
RA, R6

State-of-the-Art Study Concerning Near-Field Earthquake Ground Motion

Manuscript Completed: December 1980
Date Published: March 1981

Prepared by
H. J. Swanger, S. M. Day, J. R. Murphy, R. Guzman

Systems, Science and Software
P. O. Box 1620
La Jolla, CA 92038

Prepared for
Division of Reactor Safety Research
Office of Nuclear Regulatory Research
U.S. Nuclear Regulatory Commission
Washington, D.C. 20555
NRC FIN No. B6491
Under Contract No. NRC-03-78-155

ABSTRACT

This report presents a summary of an investigation into the applicability of theoretical earthquake source modeling to the definition of design ground motion environments for nuclear power plants located in the near-field of potentially active faults. A variety of theoretical source models are examined to determine the characteristics of near-field ground motion predicted by such models and to isolate the sensitivities of high-frequency radiation characteristics to specific elements of the models. It is concluded that the hign frequency ground motions predicted by the models are quite sensitive to particular details of implementation for which data and theory provide rather poor constraints. Examination of dynamic earthquake models suggests guidelines for extrapolation of model parameters to new stress-drops and magnitudes which are contrary to those procedures already in use. Guidelines for future modeling efforts which may better quantify the uncertainties in such procedures are recommended. Also recommended are studies which may offer constraints useful for both empirical and theoretical modeling procedures.

TABLE OF CONTENTS

TABLE OF CONTENTS (cont'd)

TABLE OF CONTENTS (cont'd)

LIST OF TABLES

LIST OF ILLUSTRATIONS

LIST OF ILLUSTRATIONS (cont'd)

LIST OF ILLUSTRATIONS (cont'd)

LIST OF ILLUSTRATIONS (cont'd)

LIST OF ILLUSTRATIONS (cont'd)

I. INTRODUCTION

This report, together with the first annual report (Swanger, et al., 1980) present a summary of the results of a two-year investigation into the applicability of theoretical earthquake source modeling to the definition of design motion environments for nuclear power plants located in the near-field of potentially active faults. The first annual report presented results of a systematic literature search in which various empirical and theoretical models which have been proposed for use in estimating near-field earthquake ground motion parameters were reviewed, compared and evaluated. With regard to empirical models for predicting earthquake ground motion parameters, it was concluded that existing procedures are not adequately constrained by the available near-field data. This inadequacy is evidenced by the fact that the variability in near-field ground motion parameters predicted using the different procedures can exceed an order of magnitude.

Site-specific computer simulation of earthquake ground motion, based on theoretical models of both the source process and the propagation and dissipation of seismic energy in the site geologic structure, offers a second tool for the estimation of near-field ground motion. This tool has been shown to be an effective technique for predicting low-frequency ground motion (of the order of 1 Hz or less) in the near-field, provided the depth-varying elastic properties of the earth are rigorously accounted for in the modeling procedure. In contrast, the deterministic simulation of high-frequency ground motion, which is of primary concern for nuclear power plant response, is highly sensitive to the specification of the source process.

In the first annual report, the characteristics of the various proposed theoretical earthquake source models were reviewed. It was noted that all such models have in common the requirement to specify values for a variety of parameters in order to deterministically synthesize near-field ground motion. The parameters must be deduced

empirically, by applying the model to actual earthquakes and recording sites, then modifying the source model parameters to achieve agreement with the recorded data. The available empirical data may not provide very good constraints on some of the parameters (e.g., stress-drop, rupture velocity) which have a strong influence on the computed ground motion. Thus, one way of viewing the current state-of-the-art of theoretical modeling is as an extension of conventional empirical procedures. The curve-fitting approach of the conventional procedure is replaced by a complex computational procedure which is capable of incorporating in a fairly rigorous fashion the influence of fault orientation, geologic structure, and long-period source characteristics; the high-frequency source characteristics are normalized so as to fit response spectral characteristics of some near-field data set. Looked at from this point of view, the theoretical modeling is subject to uncertainties which are related to those of the conventional empirical methods. In particular, there are uncertainties associated with (1) scatter in the data relative to the model prediction, (2) extrapolation to geometrical circumstances for which little data exists, (3) extrapolation to geologic structures for which little data exists, and (4) application to hypothetical earthquakes which may differ greatly in their source characteristics from those to which the model was fit.

With respect to (2) and (3), the theoretical approach has a substantial degree of independence from the purely empirical approach, because of its ability to incorporate some well-established geometrically- and geologically-controlled phenomena into the extrapolation process. Furthermore, the theoretical approach admits parameter studies to delineate the sensitivity of ground motion predictions to the various geometrical and geological parameters (e.g., intrinsic attenuation, surface layering, fault orientation).

This degree of independence from the purely empirical approach renders theoretical modeling a potentially useful adjunct to the empirical method, even though large uncertainties in the

high-frequency source characteristics remain. However, the usefulness of a given theoretical procedure depends upon its ability to predict observed trends in ground motion data. Moreover, in view of its semi-empirical nature, it is essential to critically examine the applicability of the theoretical model to earthquakes which may be expected to differ substantially in source characteristics from those to which the model was normalized.

During the past year, our research effort has centered on the analysis of various theoretical earthquake models and the characteristics of near-field motion suggested by these models. Our objectives are to determine the applicability of the models for simulation of near-field ground motions and to assess the uncertainties in applying such models to new situations, i.e., to hypothetical design earthquakes which differ substantially in source characteristics from the recorded earthquakes to which the model was normalized. This report provides a summary of the research conducted in support of these objectives during the second year of this contract.

Four distinct classes of source models were examined to determine to which features of each source model the near-field high-frequency ground motion is sensitive. In Section II, the characteristics of the near-field ground motion predicted by constant dislocation kinematic models were examined. In particular, the dependence of ground motion predictions on the degree of rupture coherence, mode of stopping, and earthquake magnitude are considered. In Section III, this kinematic approach is extended to a consideration of the predicted near-field ground motions associated with isloated sources of radiation which may arise as a result of local stress concentrations. This is followed in Section IV by an analysis of the fault slip functions predicted by fixed-rupture-velocity dynamic models with particular emphasis on their compatibility with the constant dislocation specifications generally employed in the more heuristic kinematic models. In Section V, one of the more

sophisticated spontaneous rupture, dynamic earthquake models which is currently available is described and used to examine the dependence of the spatial distribution of the predicted slip function on the assumed distribution of stress on the fault as well as on the mechanism by which the fault rupture is made to stop. This is followed in Section VI by a summary, together with a statement of conclusions and recommendations for additional research. Finally, Appendix A provides a characterization of some of the better documented near-field strong motion data.

II. CONSTANT DISLOCATION MODELS

2.1 INTRODUCTION

In this chapter we will examine the class of kinematic earthquake source models known as constant dislocation models. These models are of interest in that they have been most widely applied in seismology for purposes of seismogram synthesis. The most important characteristic of those source models is that a single slip function is specified and assumed to be constant over the entire fault surface. It is known that this assumption is unrealistic to the extent that there is no known physical process in the earth which could produce an earthquake with a uniform slip everywhere in a confined area, but for many problems constant dislocation models have proven useful at describing the radiation produced over some limited frequency band.

Here we examine the characteristics of near-field motion suggested by such models, and isolate those model parameters which appear to have the greatest influence on the predicted near-field ground motion. Some of these sensitivities are obvious. For example, the radiation produced by these models scales linearly with the spectral characteristics of the slip function. However, the dependence of the high frequency ground motions on the prescribed rupture history and fault dimensions is not obvious.

There are numerous earthquake models in the seismic literature which fit into this particular class. Here we restrict attention to simple models which contain features common to most of those which have been proposed. For example, all calculations of ground motion are for a whole space model of the earth. Now, while it is true that many of the characteristics of near-field ground motion can not be duplicated using such a model, the characteristics of the radiation which are source dependent are more easily isolated in whole-space calculations. By the same token, calculations will be

restricted to the near-field since even the most basic characteristics of high frequency ground motions beyond about 25 km are difficult to obtain without detailed structure and a reasonable knowledge of the intrinsic attenuations of earth materials.

2.2 VARIABILITY OF GROUND MOTIONS IN THE NEAR-FIELD

The manner in which ground motions vary in the near-field is particularly important in the specification of design motions where theoretical models may be used not only to synthesize ground motions, but also assist in the construction of near-field attenuation relationships. The variability of ground motions suggested by theoretical models may also help in the assessment of the representativeness of the few available near-field records. In this section, we examine the spatial variations of motion predicted by a simple constant dislocation earthquake model. We will assume a rectangular fault surface with uniform rupture propagation initiating at a corner of the fault. The slip function will be taken to be a ramp function in time.

The geometry chosen is shown in Figure 2.1. The fault has dimensions of 10 x 5 km and is buried 5 km below the receivers. Three profiles were chosen, two along the strike of the fault (A and C) and one normal to the fault (B). Rupture initiates in the lower left corner and propagates circularly toward profile A. Source parameters are summarized in Table 2.1. All seismograms computed were banded limited to 0 to 8 Hz. Energy at 8 Hz has wavelengths considerably smaller than any characteristic physical dimension of the problem, so the trends observed in the high frequencies here should adequately describe the general behavior at higher frequencies.

Horizontal accelerations normal to the fault strike for profiles A, B and C are shown in Figures 2.2 through 2.4. Note that the accelerations tend to be dominated by a few distinct phases, particularly in profile A. The one-second long ramp slip time function leads to a duplication of every arrival with opposite sign delayed one second. An obvious trend is seen where the peak motions

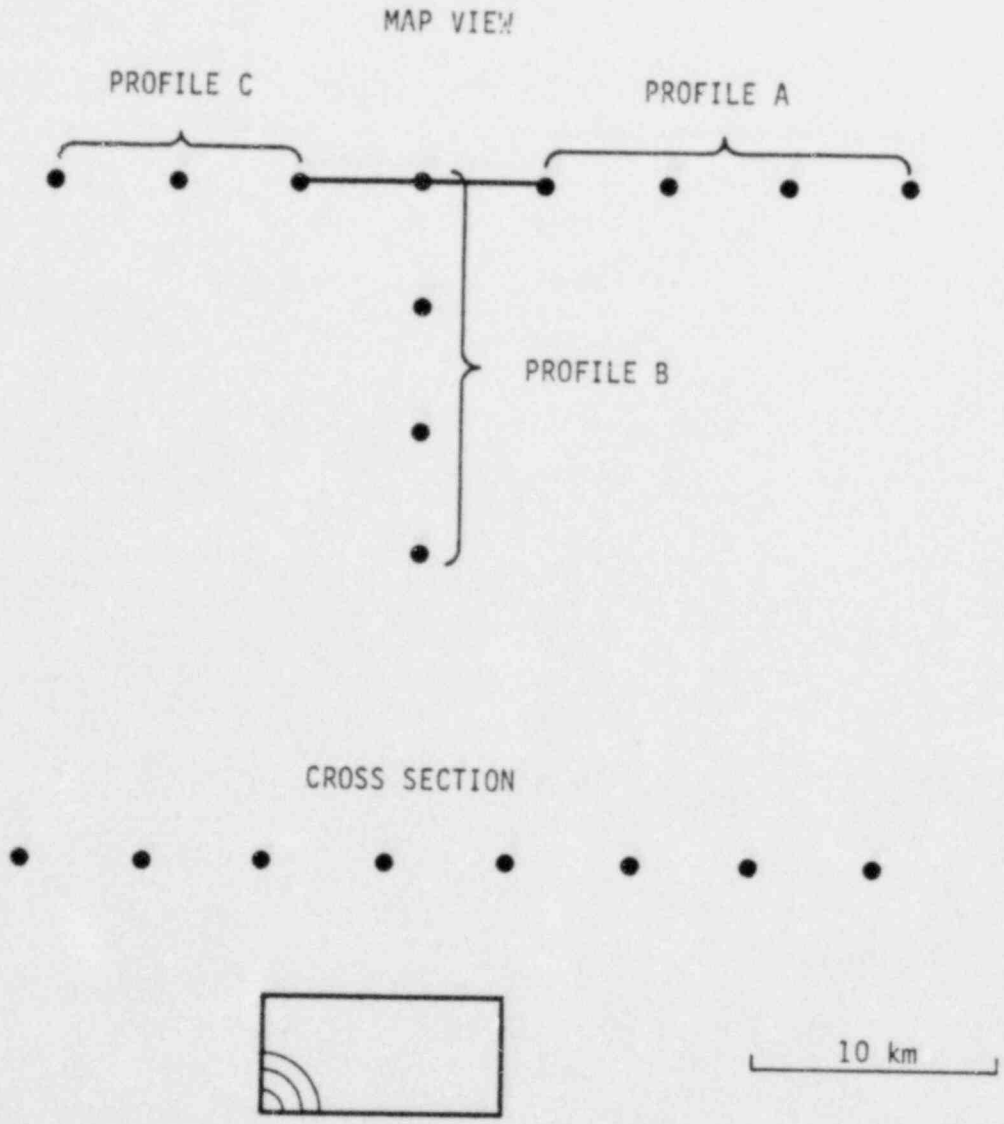

Figure 2.1. Geometry used in constant dislocation model ground motion calculations.

TABLE 2.1

FAULT AND MEDIA PARAMETERS USED IN SIMULATION

Fault Parameters:	
Fault length	10 km
Fault width	5 km
Rise time	1 sec
Slip velocity	1 m/sec
Rupture velocity	2.64 km/sec
Media Parameters:	
Compressional velocity	6.0 km/sec
Shear velocity	3.3 km/sec
Density	2.7 gm/cm^3

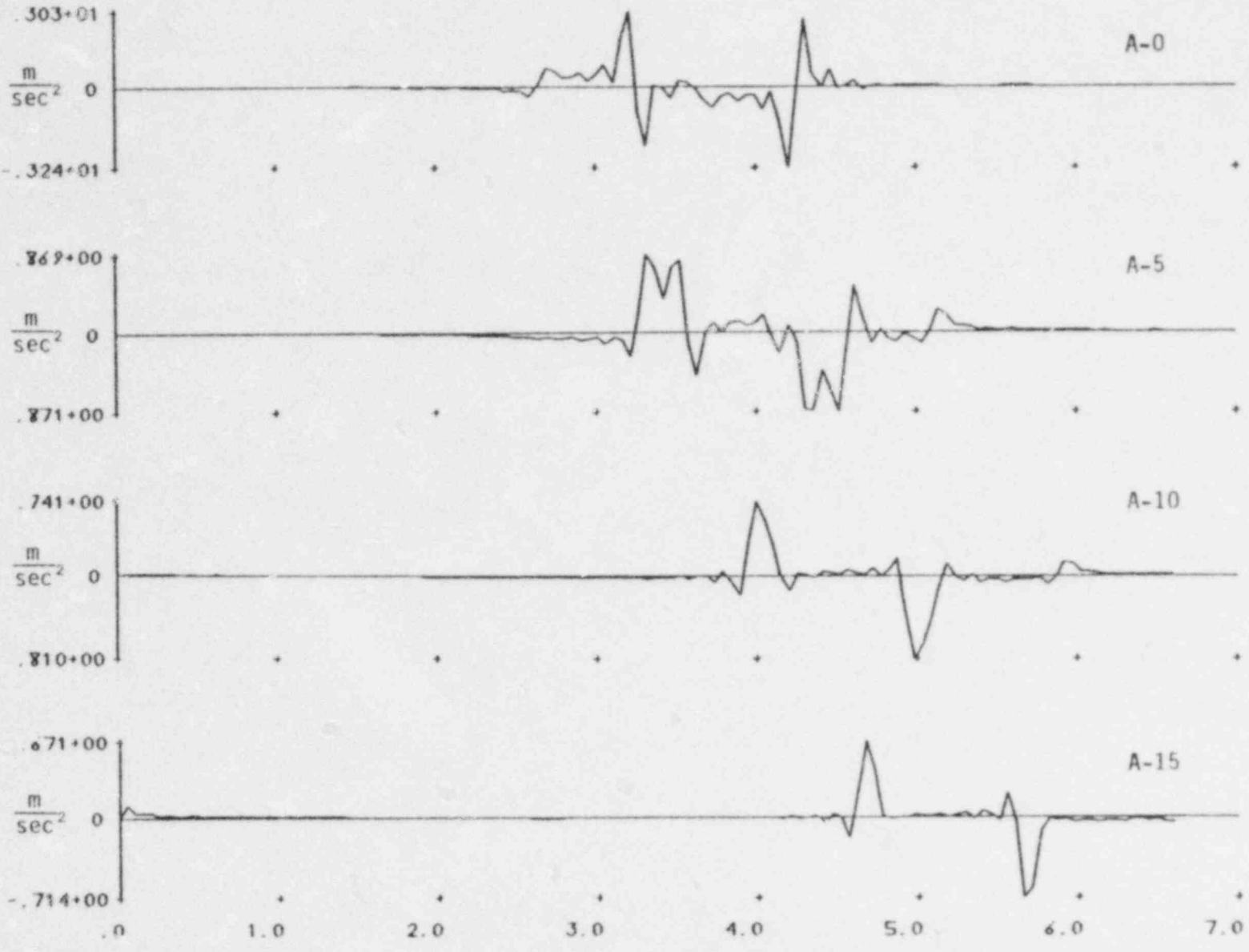

Figure 2.2. Accelerations normal to fault strike computed for Profile A.

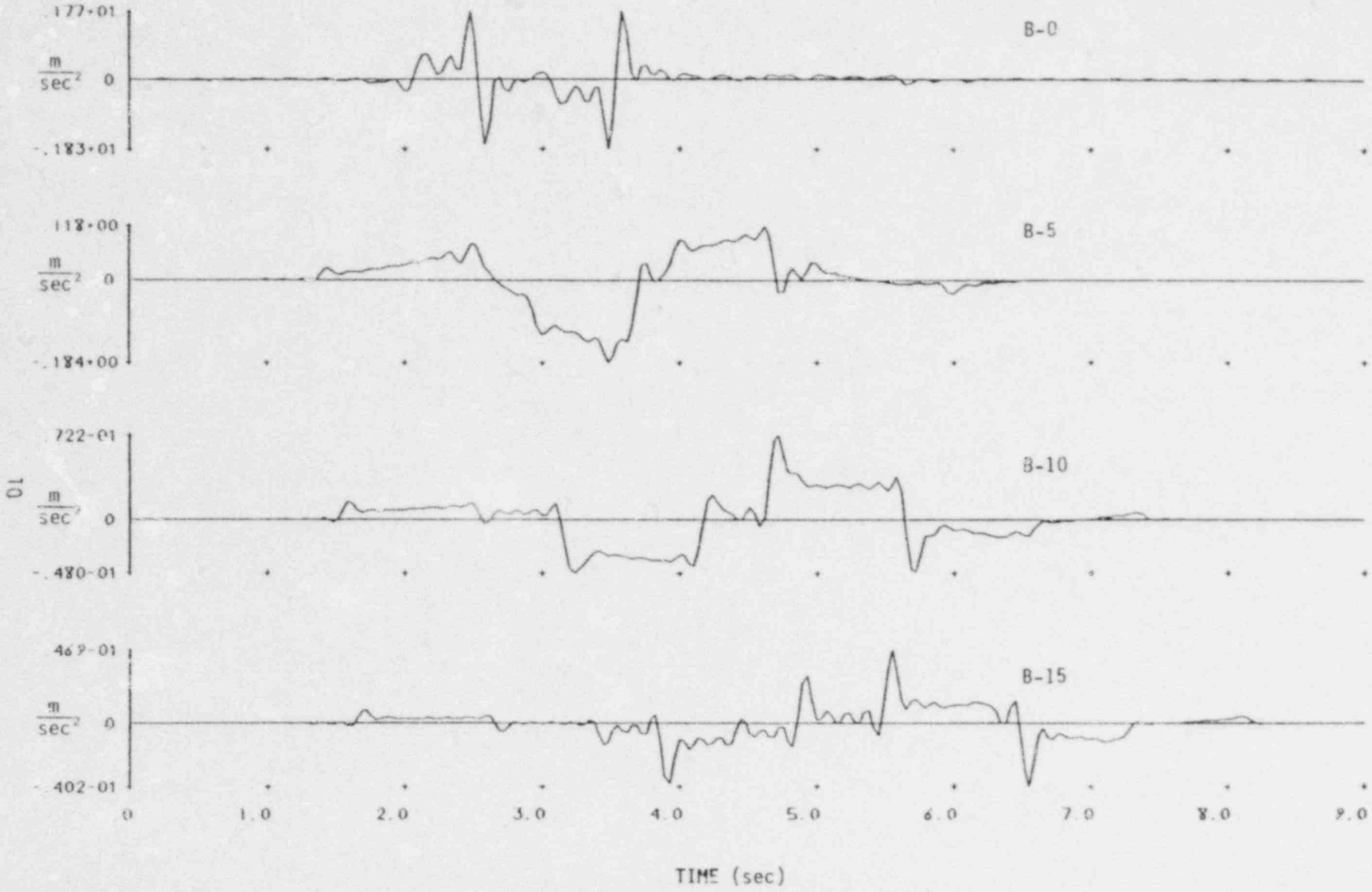

Figure 2.3 Accelerations normal to fault strike computed for Profile B.

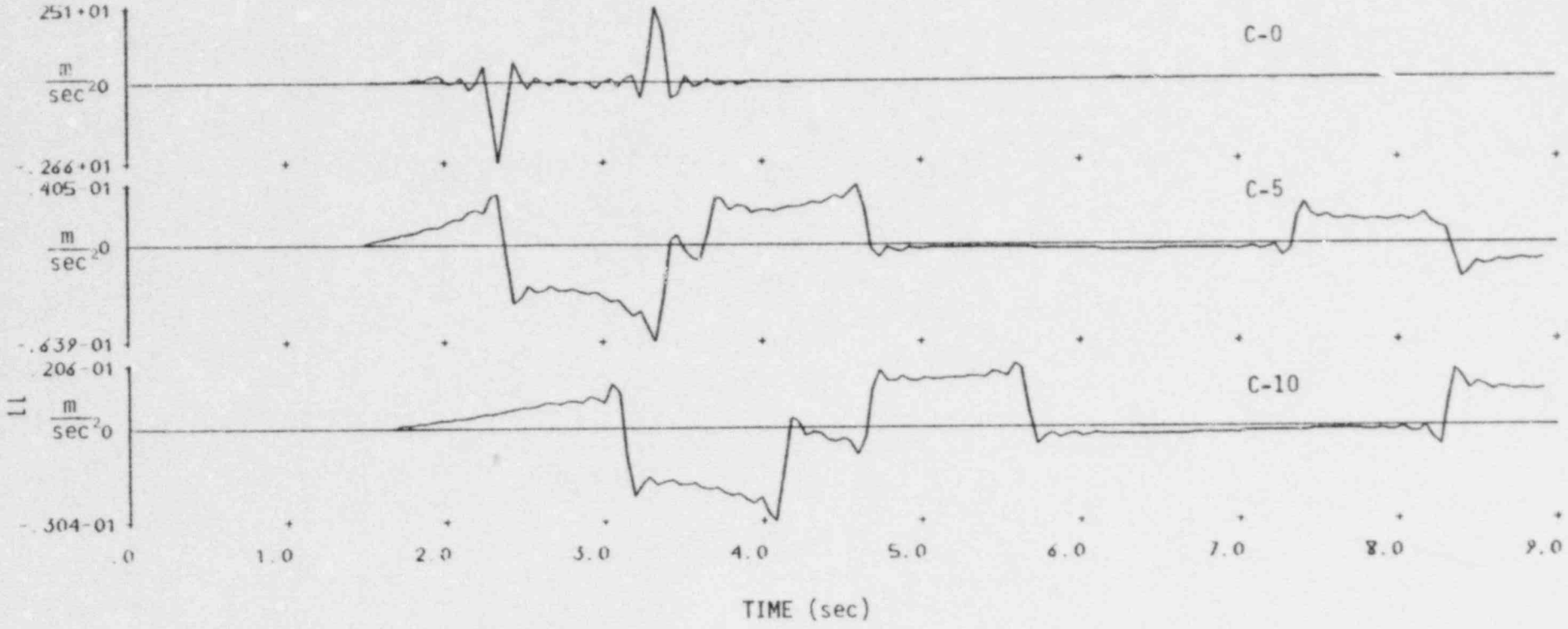

Figure 2.4. Accelerations normal to fault strike computed for Profile C.

are compared for the three profiles. The peak horizontal accelerations are shown in Figure 2.5 and peak velocities in Figure 2.6. Just above the fault there are variations of about a factor of two, but as little as 5 km away, the motion in the profiles vary by an order of magnitude. Note that all of the horizontal motion is in the direction normal to the fault strike for Profiles A and C and there is motion in both horizontal directions in Profile B. The predicted wide variation in amplitude also extends to the far-field and this appears to be in conflict with the empirical data in that such trends have not been observed.

The strong variation of motion with azimuth from the direction of primarily rupture propagation is usually referred to as seismic directivity. The basic physical principle governing directivity is that energy is focused in the direction of the propagation and hence there are larger amplitudes in that direction. With this view of the process, one would expect the dominant motions to be associated with radiation from a large area of the fault and that they would arrive at the observation point over a very short time interval. This appears to be true for the computed velocity but not necessarily for the computed acceleration. Figure 2.7 shows the accelerations computed for the nearest observation point on Profile A and notes the arrival times associated with rupture initiation and a few stopping phases. Note that the largest motions correspond to stopping phases at the top of the fault, initiating at the time of arrival of the earliest such phase. This is true from all of the stations in Profile A. It appears that directivity in acceleration should not be viewed as being due to focusing of energy from the entire fault, but rather a focusing of energy from stopping phases. Thus, the smooth rupture propagation over the fault plane contributes very little to the total motion.

The response spectra for the 10 km stations of the three profiles are shown in Figures 2.8 through 2.10. The spectral values of Profile A exceed those of Profile C by approximately an order of magnitude at all frequencies. In Profile A and B there is some

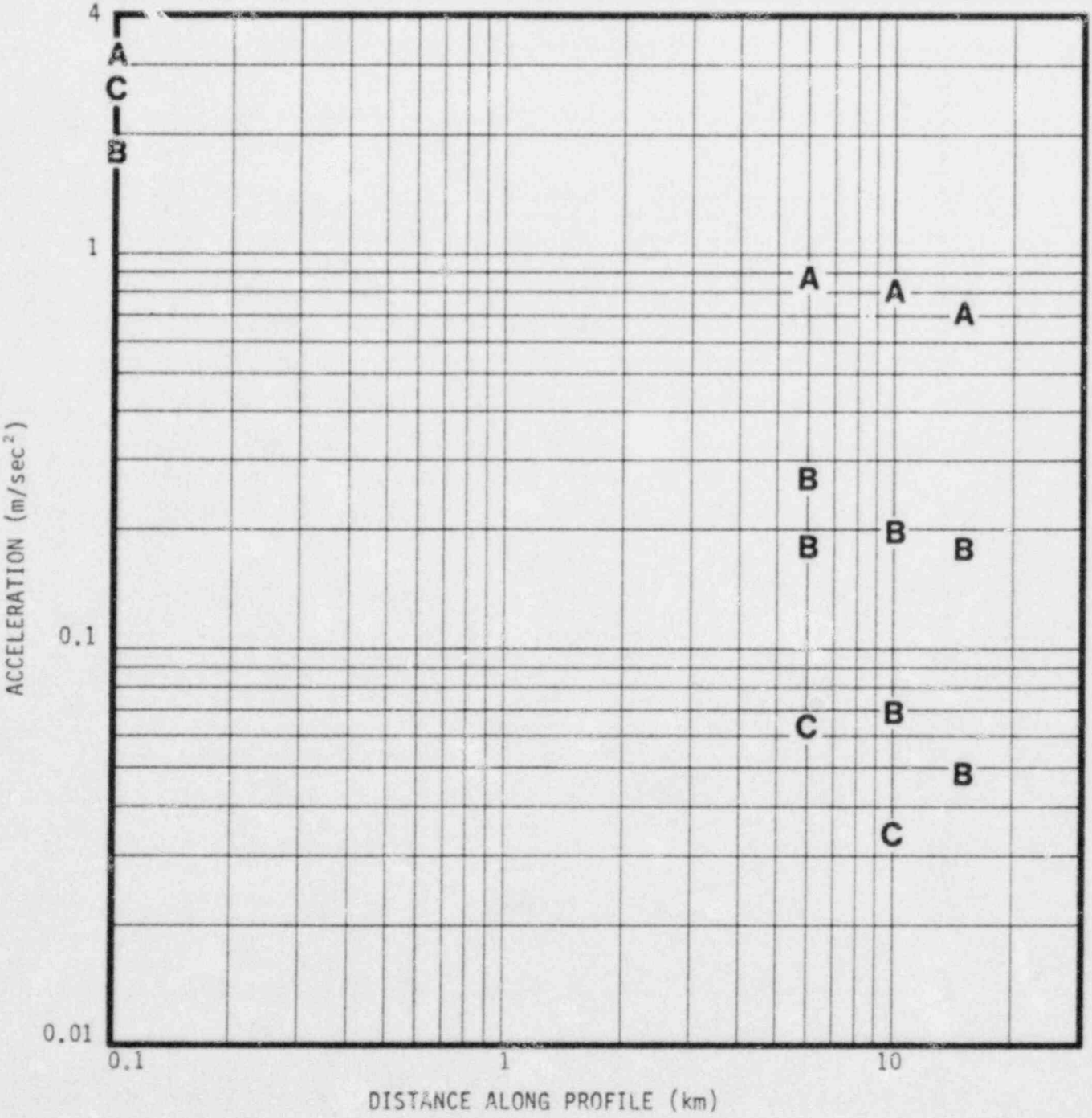

Figure 2.5. Peak accelerations for the three profiles. Both components are plotted for Profile B.

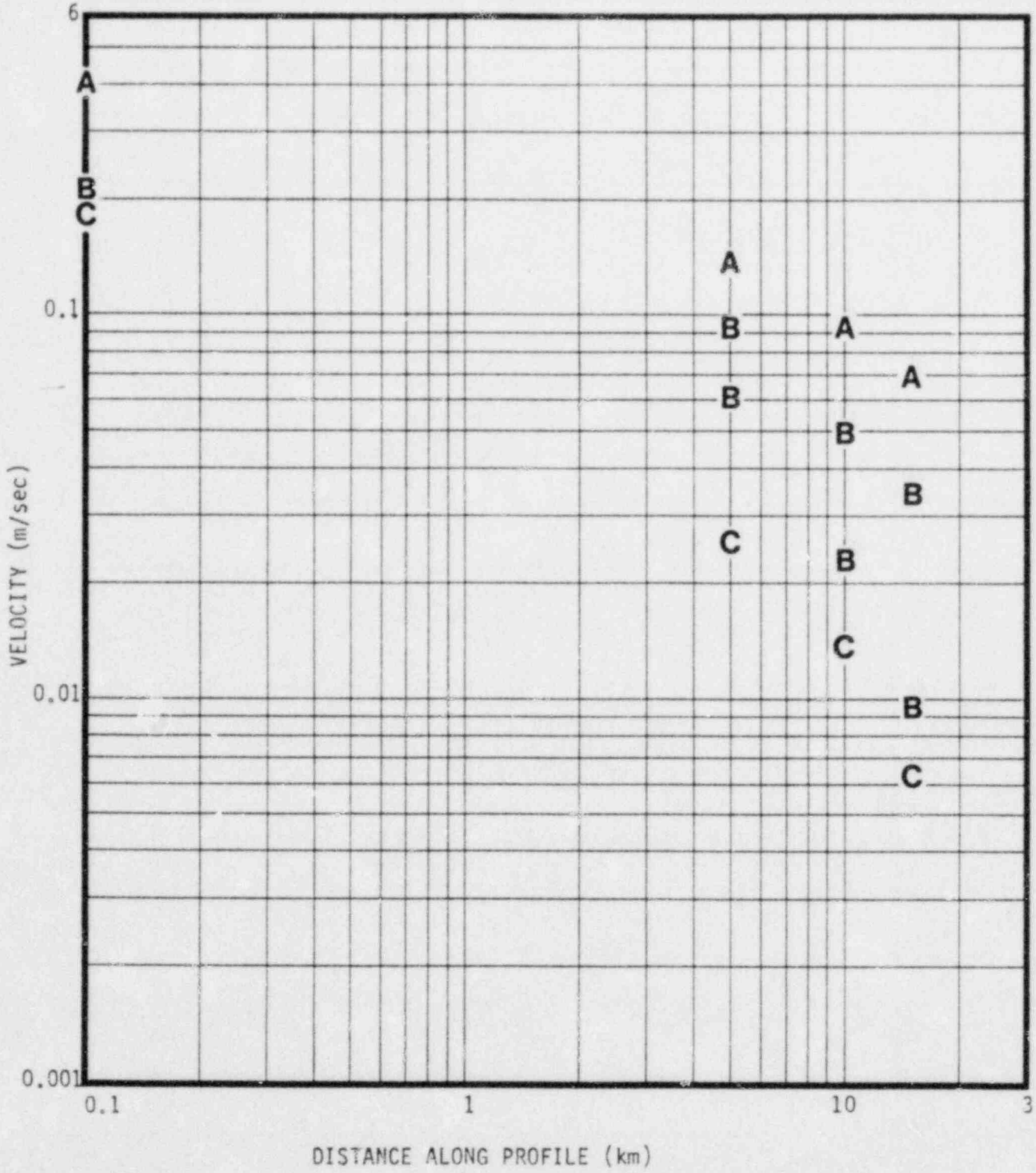

Figure 2.6. Peak velocities for the three profiles.

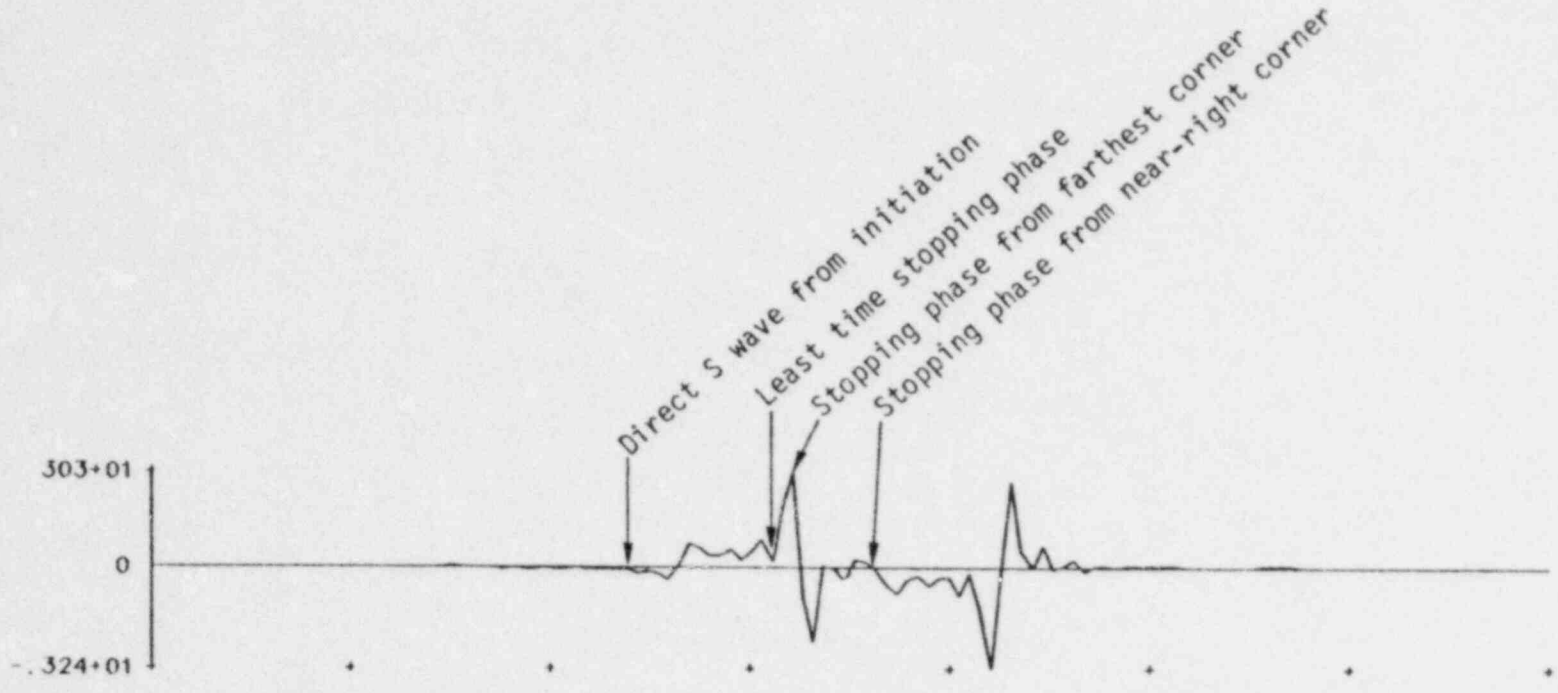

Figure 2.7. Identification of important arrivals in the acceleration computed for the closest station in Profile A. Duplication of largest phase due to the slip function used.

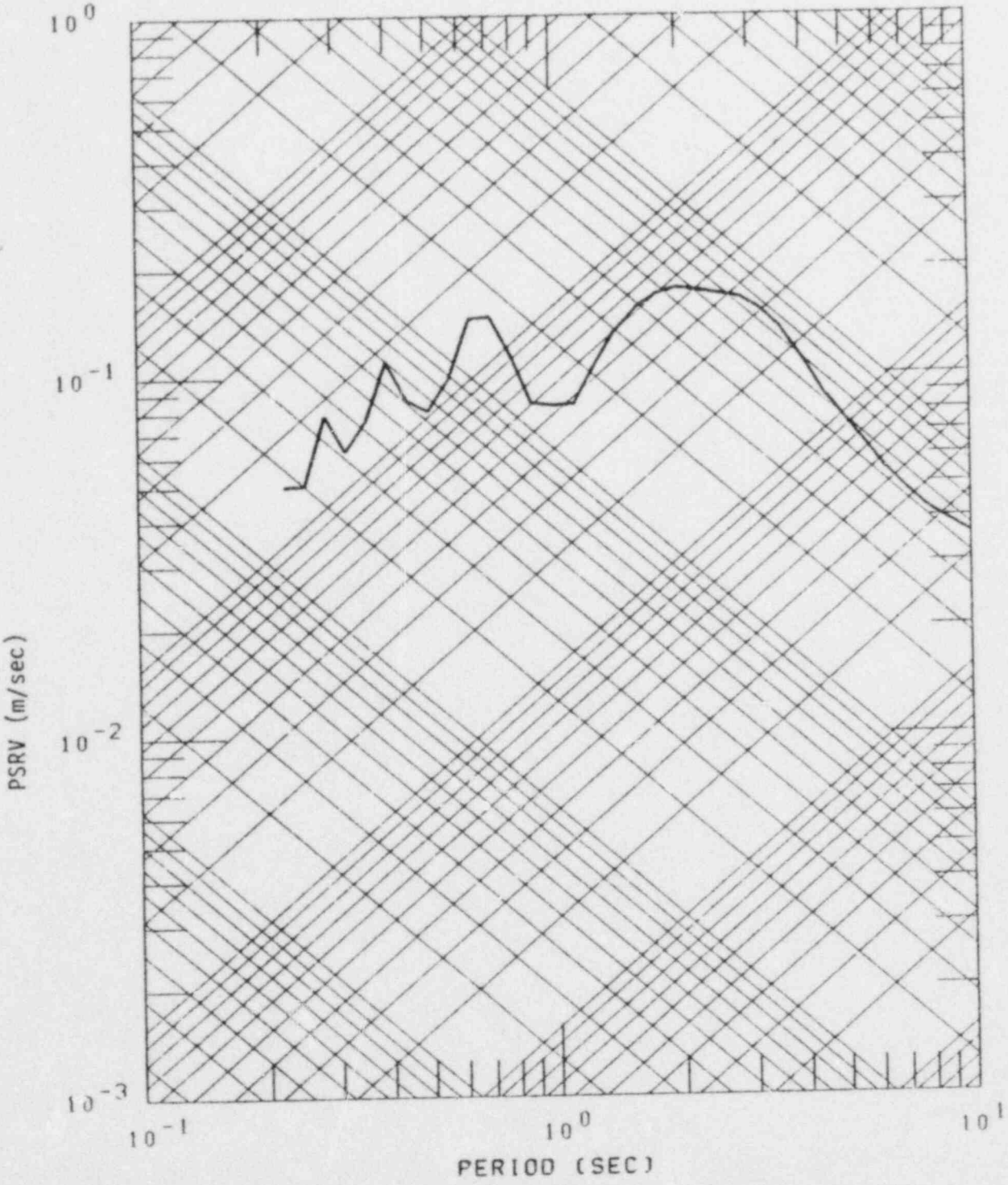

Figure 2.8. Velocity response spectrum with two percent dampling for Station A-10.

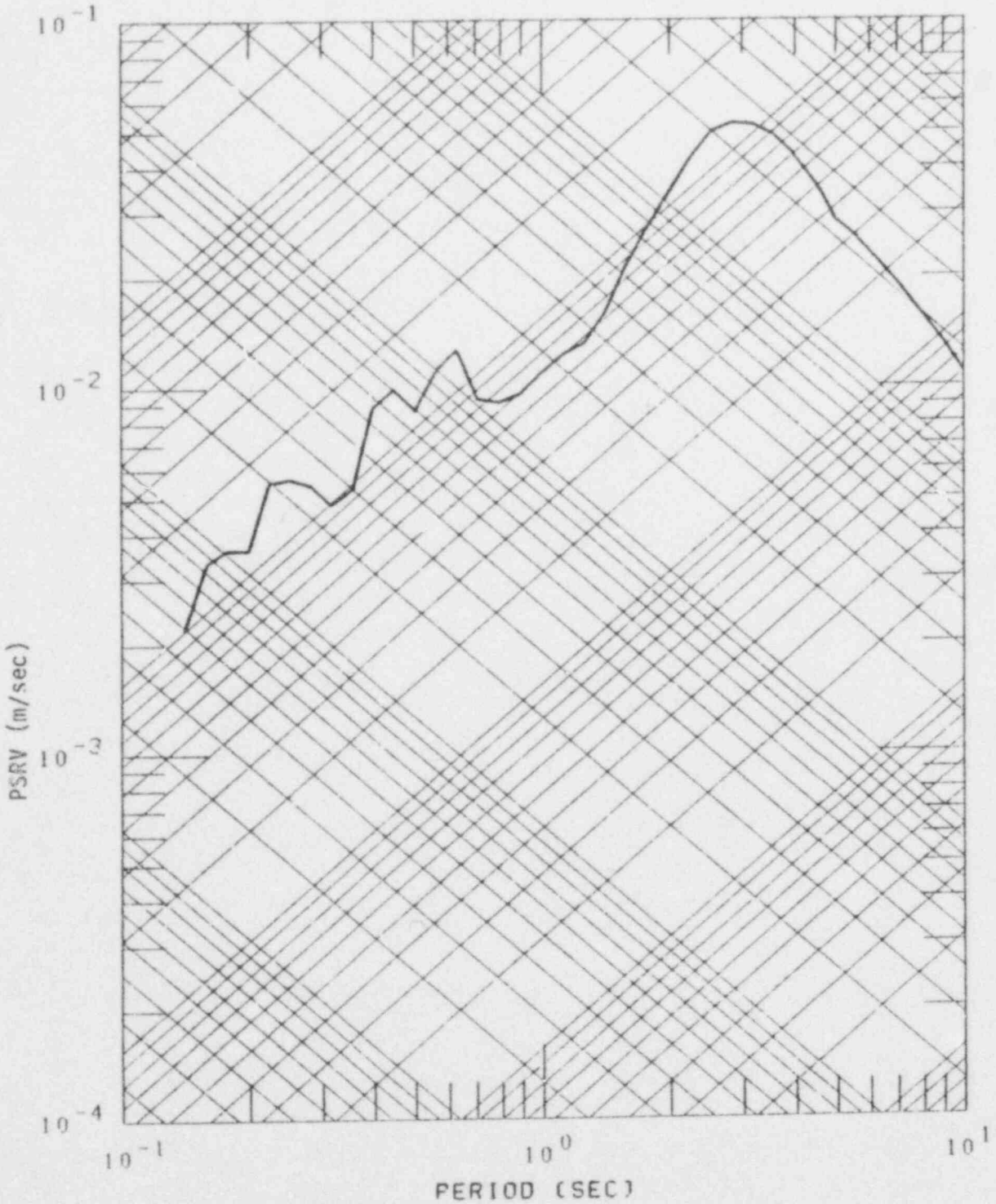

Figure 2.9. Velocity response spectrum for Station B-10.

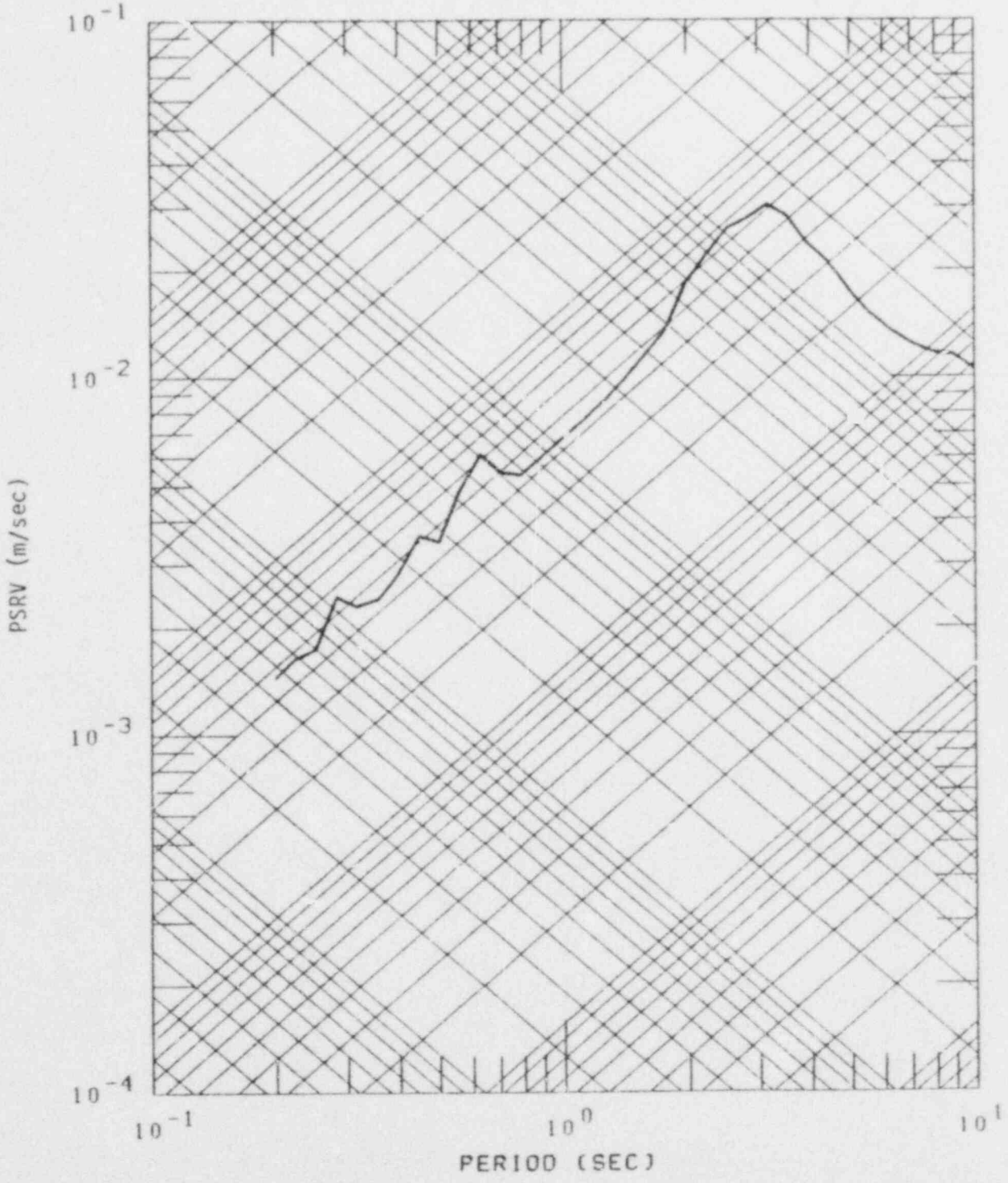

Figure 2.10. Velocity response spectrum for Station C-10.

indication that the high frequency decay is not proportional to period as it should be if the peak acceleration is finite. It is well known that in some cases, simple kinematic models will predict infinite accelerations in the near-field with ramp-like slip functions (Madariaga, 1978). This might be the case here in the focused direction if an infinite band width was considered.

The large variations in ground motions suggested by this simple model do not appear to be consistent with data sets such as the strong motion recordings for the 1979 Imperial Valley, California, earthquake. In this case, although the data set includes stations at a variety of locations with respect to the fault orientation, there is little indication of such large variations in the peak motions. To some extent the trends here may be overly exaggerated. For example, the rupture was assumed to be unilateral and, though such motion is often inferred from low frequency interpretations of earthquake source mechanisms, this may not be realistic at the high frequencies. It seems likely that any bilateral components in the rupture propagation would serve to suppress the prediction variation to some extent.

Another characteristic that may be unrealistic is the uniform sudden stopping of rupture on a prescribed boundary. This leads to the large stopping phases in the focused direction, and it is not hard to conceive of alternate physical mechanisms which would reduce the significance of these phases. For example, one could assume that the rupture decelerates gradually at the edges of the fault. In this case, the rate of deceleration will control the high frequency amplitudes. Another option would be to abandon the assumption of coherent rupture. Randomization of the rupture propagation will make the coherent effects of stopping less likely to occur. Unfortunately, there is little physical basis to guide the choice of the random parameters. Constant dislocation models employing incoherent rupture will be discussed further in Section 2.6.

2.3 RUPTURE VELOCITY

In an earlier report (Swanger, et al., 1980) it was noted that direct measurements of rupture velocity in earthquakes are few and, consequently, that this parameter is one of the least well constrained source parameters. It was also noted that the values of rupture velocity may be important in the scaling of high frequency motions. Inferred values of this parameter suggested in the literature range from about half the seismic shear velocities to the Rayleigh velocity (i.e., approximately 0.9 times the shear velocity). Theoretical studies have suggested the possibility of supersonic rupture velocities, greater than tne shear velocity (Andrews, 1976; Day, 1979).

Rupture velocities near the shear velocity are of particular interest in ground motion simulations because for such values the effects of seismic directivity will be most severe. The previous examples shown in this section employed a rupture velocity of 0.8 times the shear velocity. Figure 2.11 shows the accelerations at 10 km for profiles A, B and C computed using a rupture velocity of 0.9 times the shear velocity. The level of motion in Profiles B and C does not differ by more than 20 percent from the previous case, but the peak values in Profile A nearly double. The response spectra shown in Figures 2.12 through 2.14 also illustrate this trend. The overall level of response is enhanced relative to the slower rupture velocity case, particularly at high frequencies.

In the focused direction the value of rupture velocity can strongly affect the computed amplitudes. The contributions which are primarily affected are the stopping phases which dominate the accelerations in the plane of the fault. Variations in rupture velocity do not appear to have a significant effect on the motion computed at locations away from focused areas. Thus, it can be inferred that if the strong stopping phases were suppressed by either gradual stopping or by addition of rupture incoherence, then the dependence on rupture velocity might be expected to be less dramatic.

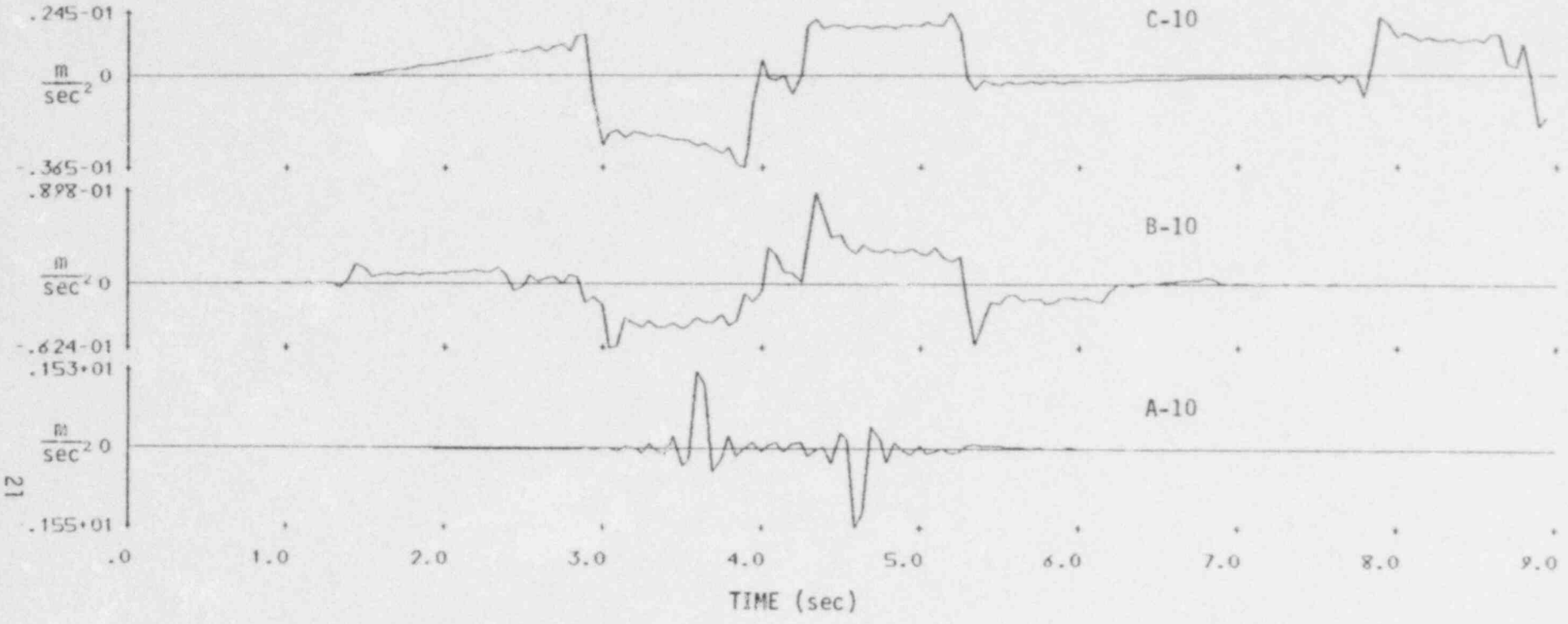

Figure 2.11. Accelerations normal to the fault strike using a rupture velocity of 0.9 times the shear velocity.

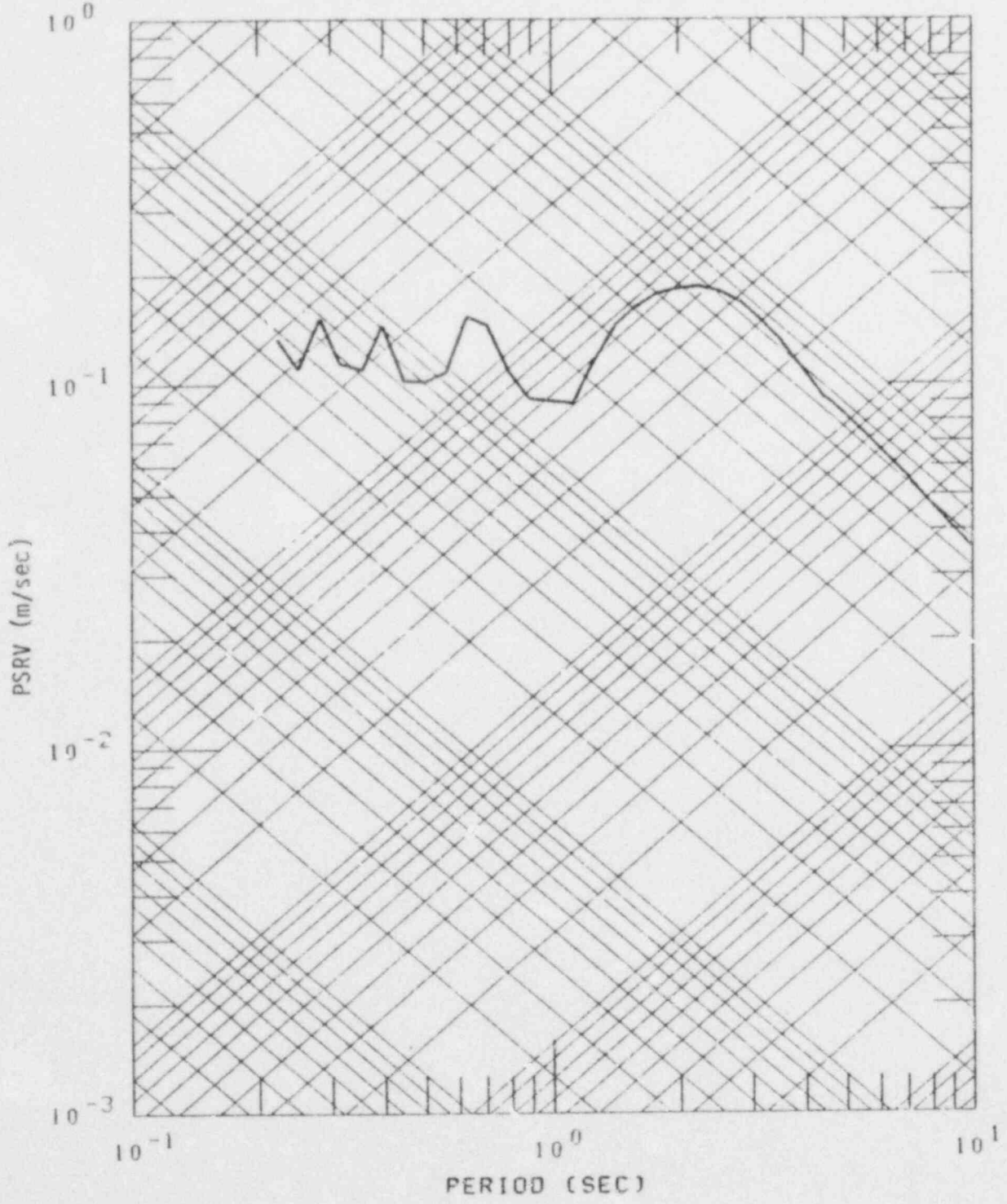

Figure 2.12. Velocity response spectrum for Station A-10 using factor rupture velocity.

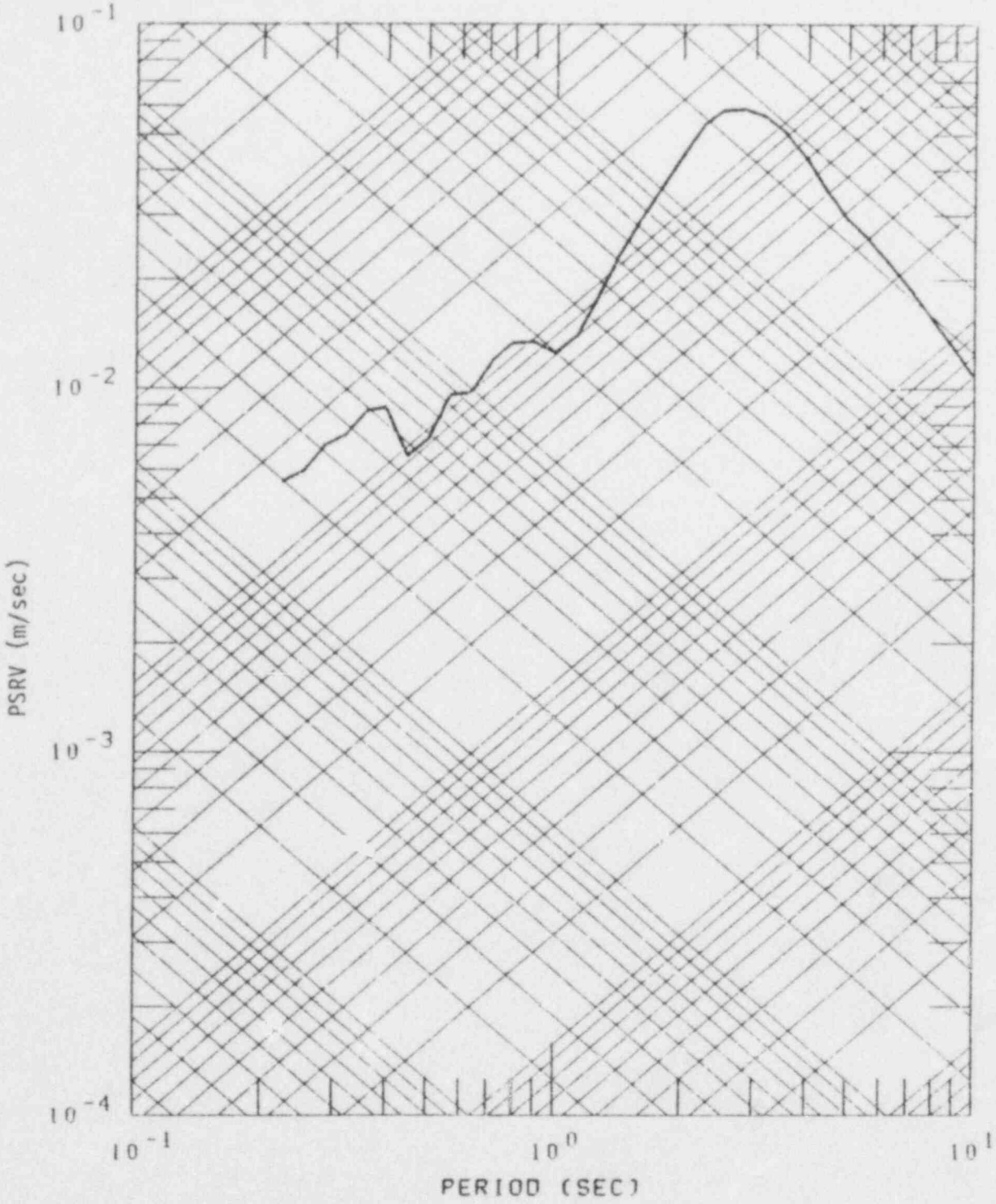

Figure 2.13. Velocity response spectrum for Station B-10 using faster rupture velocity.

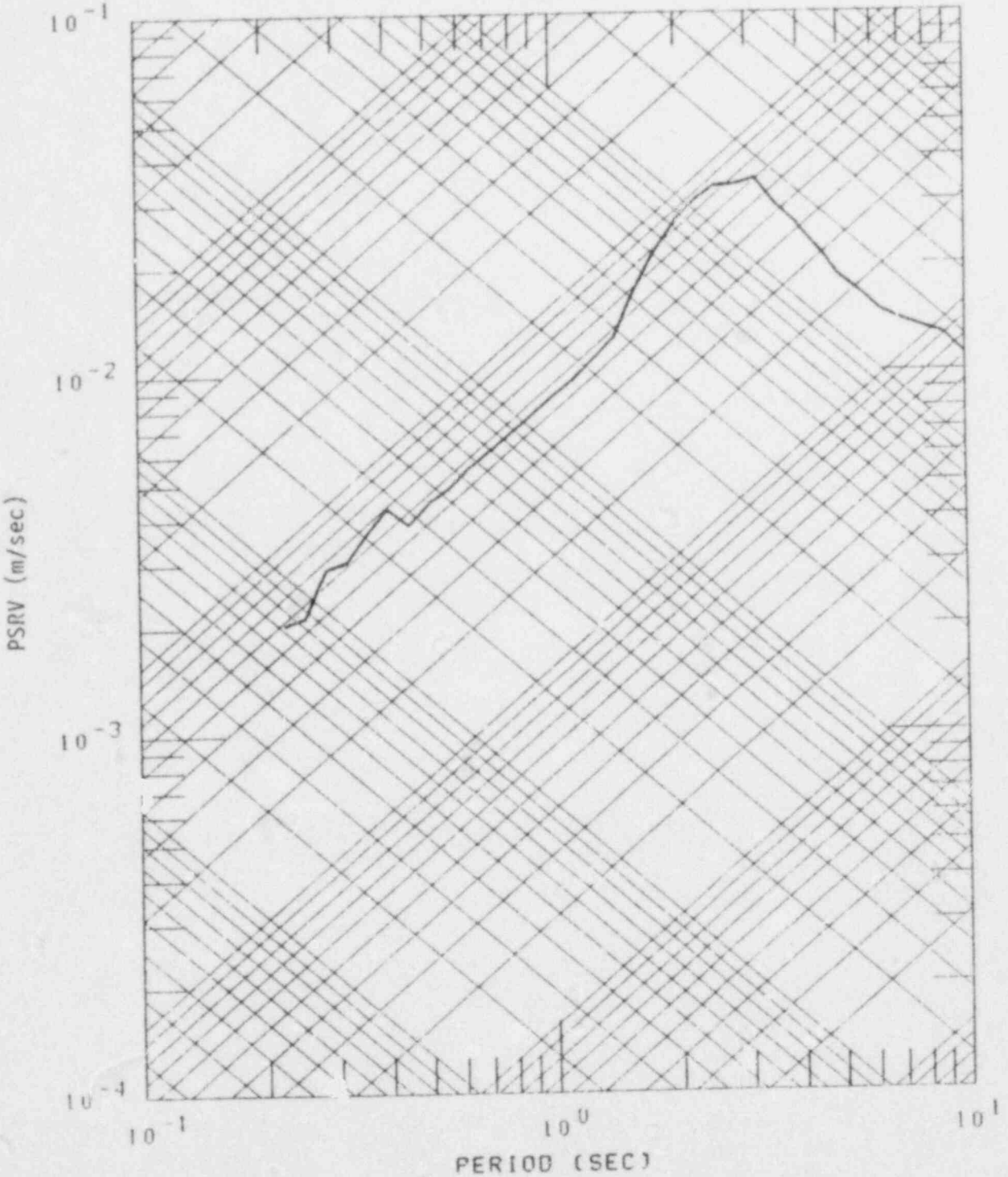

Figure 2.14. Velocity response spectrum for Station C-10 using faster rupture velocity.

Dynamic modeling studies have suggested the possibility of supersonic rupture when large regions of uniform pre-stress are present, and examples of the effects of such rupture velocities are given in Section V. Such rupture velocities are almost never considered in kinematic modeling and the consequences of such effects with respect to near-field, high frequency ground motion are not well understood.

2.4 HIGH FREQUENCY MOTION AND THE CHOICE OF SLIP FUNCTION

A constant dislocation model by definition is one which is characterized by a single slip function which acts over the entire rupture surface. The ground motion scales linearly with the nature of the slip function used. That is, the Fourier spectra of the motion is directly proportional to the Fourier spectrum of the assumed slip functions. The dependence of response spectra on the slip function is not linear, but it is a reasonable approximation to assume that it, too, will scale roughly with the Fourier spectrum of the slip, particularly for the case in which the damping is low.

Slip functions generally fall into two varieties; simple analytic forms like ramps or exponentially damped ramps, or approximations to some dynamic slip function. Several of the proposed alternatives for simple analytic forms were discussed in a previous report (Swanger et al., 1980). For ramp-like slip functions, high frequencies scale directly with the initial slip velocity for both peak motions and response spectra as long as the periods of interest are less than the duration of the ramp, which appears to be the case for most large earthquakes.

On the other hand, the scaling of motions for approximations to dynamic slip functions is much more complicated. A major feature of the models is the concentration of high frequency energy early in the slip time history. For example, constant stress drop dynamic earthquake models do not produce slip functions which are constant over the entire fault plane. With a uniform pre-stress and no rupture boundaries, the slip function is a ramp at the hypocenter

and elsewhere slip velocity contains a square-root singularity at commencement of slip whose strength increases with distance from the hypocenter. The only circumstance where the high frequency slip function characteristics are nearly constant over the entire fault surface is the case of a long, narrow fault. For this case, the early slip behavior becomes relatively uniform after the rupture has progressed a few fault widths (Madariaga, 1977; Day, 1979). The equilibrium behavior has a square-root singularity with strength directly proportional to stress-drop and approximately proportional to the square-root of the width of the fault (Day, 1979).

Approximations to dynamic slip functions can only be fairly evaluated by analysis of the assumptions behind these models and by direct comparison with the functions which they approximate. This will be examined thoroughly in Sections IV and V which summarize in detail results of dynamic earthquake simulations.

2.5 CONSIDERATIONS IN THE MAGNITUDE DEPENDENCE OF NEAR-FIELD GROUND MOTIONS

Magnitude is a measure of earthquake size obtained from the amplitudes of some instrument recording of the ground motion normalized to a particular distance and predetermined scale. The instruments used in magnitude determinations generally have somewhat lower resonant frequencies that the frequencies of interest here. The relationship between magnitude and high frequency ground motion characteristics depends very strongly upon the relationship between the high frequency spectrum and the spectrum near the frequencies passed by the instrument for which the magnitude is measured. For local magnitude this instrumental frequency is approximately one Hertz. Within the framework of constant dislocation models, there are two elements of the model which may contributed to a relationship between magnitude and the radiated ground motion. First, independent of any consideration of the slip function, there is the possibility that the increase in the size of the fault area with magnitude might produce larger motions. Second, there is the

possibility that the slip function might change with the fault dimensions (and therefore magnitude) in a manner which may affect the high frequency motion.

Considering the first case in which the slip function is assumed to be independent of source size, dimensional analysis suggests that there must be a limit to the extent which fault dimension affects the high frequency characteristics of the near-field motion. A possibility which is sometimes suggested is that a larger fault surface will cause directivity effects to be enhanced. If one assumes seismic directivity to be a focusing of energy from a large area of the fault surface, one might expect a larger fault surface to amplify this effect. In Section 2.2 an alternative view of the effect of seismic directivity on acceleration was suggested. There it was noted that the largest motions appear to be due not from focusing of radiation from the entire slip surface, but rather for stopping phases at the fault edges. If this is the case, one would not expect the degree of focusing to be very dimension dependent. As a test of this hypothesis, the fault of Figure 2.1 was extended to the left and the hypocenter relocated at the new lower left corner. Figure 2.15 shows the acceleration above the right end of the fault (Profile A) for a 20 km fault length compared to the previously calculated case of 10 km. Note that the peak motion has actually decreased. The largest motions arrive at times near the arrival of the least time stopping phase. Thus, for the longer fault, the dominant stopping phase radiates from farther away from the observer and, hence, are smaller in amplitude. A similar effect was observed when the fault width was doubled.

These results strongly suggest that the relationship between the extent of seismic directivity and fault dimension is not one of a simple focusing, at least for the simplest kinds of constant dislocation models. That is, while the low frequency components of the motion are quite sensitive to increased fault dimensions (i.e., magnitude), this is not necessarily the case for the higher frequency components which control the peak accelerations in the near-field.

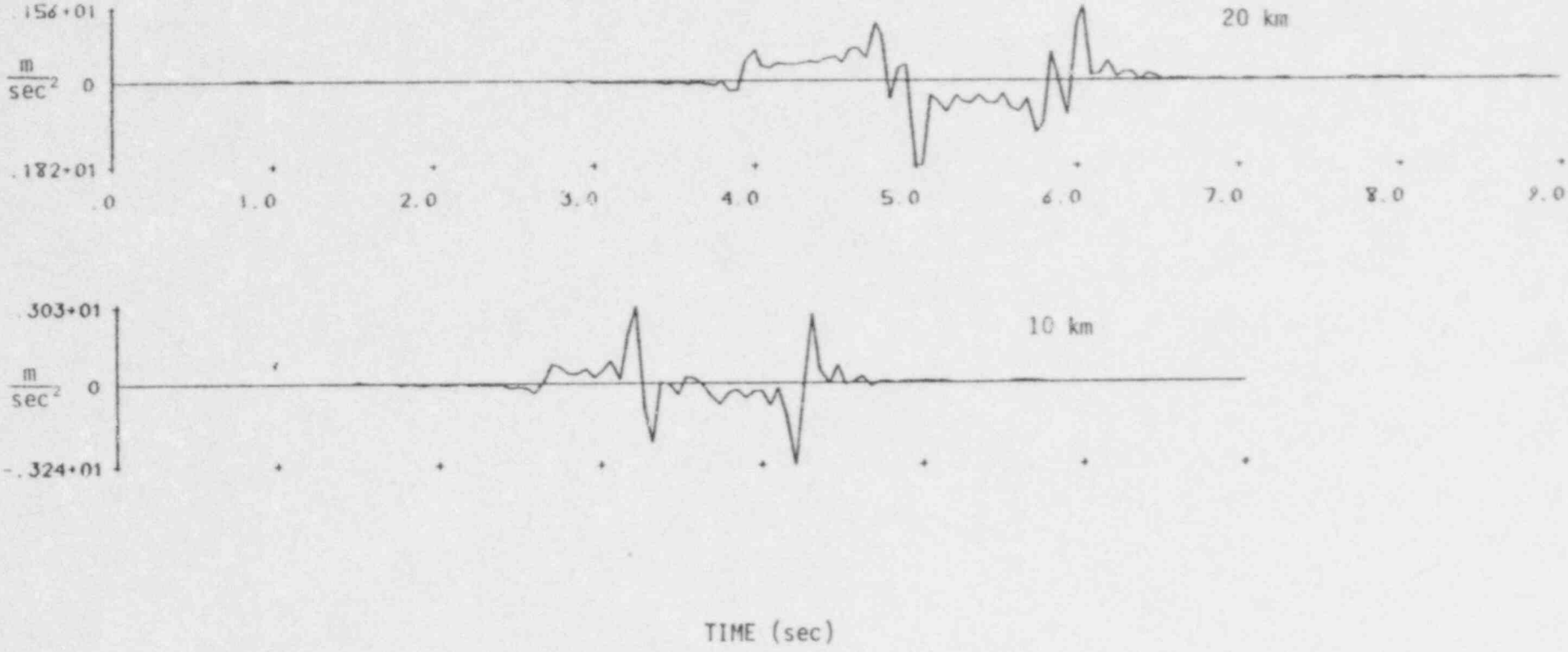

Figure 2.15. Accelerations at A-1 for extended fault length.

The remaining question concerning the possible magnitude dependence of the near-field ground motions is the potential variation of the slip function with magnitude. For example, seismic scaling studies suggest that larger final fault slip usually accompanies larger fault dimension (Kanamori and Anderson, 1975; Geller, 1976). However, there is little observational information relevant to the magnitude scaling of high frequencies in the slip function. Dynamic earthquake simulations suggest that, for uniform stress drop and uniform rupture propagation, the strength of the high frequency part of the slip function should scale with the square-root of the fault width (Day, 1979). These results were obtained allowing material strength to be unbounded.

On the other hand, Del Mar Technical Associates (1978, 1979) have argued that if a finite material strength is included, there is an upper bound to the high frequency content of the slip function, which they express as a maximum slip velocity. This assumption is based primarily on the theoretical results of Ida (1973). However, calculations by Day (1979) using a bounded material strength do not appear to support this hypothesis. This important issue will be addressed in more detail in Section V.

Another possible reason why the high frequency part of the slip function may not scale with source dimension is that rupture propagation and stress drop may not be uniform enough in large earthquakes to permit the growth of high frequencies in the slip function which are observed in dynamic earthquake simulations. That is, if a magnitude seven earthquake is in reality a superposition of a few events of smaller spatial extent occurring over a short time scale, then we would not expect the average slip function to scale with magnitude beyond a certain point. However, it is not known at the present time if there is a limit to the source dimension over which a uniform rupture can be maintained.

2.6 CONSTANT DISLOCATION MODELS WITH NONUNIFORM RUPTURE PROPAGATION

It was noted in earlier sections that constant dislocation models with uniform rupture propagation can lead to large variations

in the computed ground motions which are directly controlled by some poorly constrained model parameters. Recent models developed by Del Mar Technical Associates (1978,1979) and Hadley and Helmberger (1980) avoid the possibility of high frequency focusing by making the rupture incoherent on a small scale. In these approaches, a minimum length scale is arbitrarily chosen (usually on the order of one km) for which coherent rupture effects can exist. Incoherence is incorporated by an introduction of random perturbations on the rupture arrival time at a point or by perturbations on the travel times of the radiation to the observer, which has the same effect.

The choices for the minimum length scale and randomization parameters are arbitrary since there is little observational or theoretical evidence to assist in either choice and, in fact, the incoherence is generally prescribed with the objective of incurring that the computed ground motions are "reasonable."

Such incoherence in the rupture will lead to complicated acceleration time histories which are generally consistent with the observed data. However, there are counter-examples, such as the recording of the ground motion from the 1979 Imperial Valley earthquake at station 7. Here, the horizontal accelerations are dominated by very simple pulses and the smoothness of the signal puts a definite limit on the complexity of the rupture.

The major motivation behind rupture incoherence is to remove what are perceived as unrealistic effects of seismic directivity. As noted earlier, such effects are due not to focusing of radiation over the entire fault surface, but rather due to radiation from the abrupt stopping of rupture at the fault edges. Removal of the instantaneous stopping of rupture will also produce the desired effect. Thus, the absence of observations of strong focusing effects does not necessarily mean that rupture is generally incoherent; it could just as well be an indication that the rupture does not terminate suddenly in actual earthquakes.

2.7 CONCLUSIONS

In this chapter we have examined the behavior of simple constant dislocation earthquake source models. The models examined here also contain uniform rupture propagation terminating at a prescribed boundary. The major conclusions of this chapter are:

1. Simple constant dislocation models predict highly variable motion in the near-field due to seismic directivity.

2. In terms of high frequency radiation the large directivity effects are not caused by a focusing of radiation from a large fault area, but rather the motion is dominated by large stopping phases on the fault edges which are considerably larger in the direction of focusing than elsewhere.

3. Motion in the focused direction can be very sensitive to the choice of rupture velocity.

4. For simple models, there is not necessarily increased focusing of high frequency radiation with increased fault dimension independent of the choice of the slip function.

5. The most important issue regarding the possible dependence of the near-field motion on earthquake magnitude is whether or not the high-frequency part of the slip function is allowed to vary with magnitude. Some dynamic earthquake simulations suggest the high-frequency part of the slip functions should scale with the square-root of the fault width. Other dynamic arguments suggest that there is a limit to this increase. At present this issue is unresolved. This is an important matter since it has a significant influence on the near-field ground motions predicted by such models.

6. A few models proposed in the seismic literature have incorporated random incoherence in the rupture propagation to suppress the strong effects of seismic directivity. Lack of strong focusing in the high frequency data does not necessarily imply that rupture is incoherent on a small scale. These observations could be equally well explained by assuming that rupture does not terminate suddenly in real earthquakes.

III. KINEMATIC MODELS OF ISOLATED SOURCES OF RADIATION

3.1 INTRODUCTION

In the previous section, we examined the characteristics of ground motion produced by models with coherent rupture over large spatial dimensions. In this section we examine the characteristics of the ground motion when the rupture is incoherent or when a local feature, such as a stress concentration or fracture barrier, controls the nature of the high frequency radiation.

Several studies have noted the existence of local areas of stress concentrations in earthquakes (Hanks, 1974; McGarr, et al., 1979; Bache and Barker, 1978; Hartzell and Brune, 1979), and attempts have been made to interpret near-field accelerations in terms of these local stress fields (Hanks and Johnson, 1976). In a few events the accelerations observed have been linked to fracture barriers or localized unusual stopping behavior (Bouchon, 1978; Aki, 1979). In cases where a local phenomena is the main source of high frequency radiation, one would expect the attenuation of motion in the near-field to be quite different from that when slip and rupture is uniform over a large area.

Examination of the radiation characteristics due to local features in the fault surface may also help in the understanding of more complicated fault models which employ incoherent rupture propagation or varying slip over the fault plane. When rupture of slip characteristics vary over the fault surface, the constructive and destructive interference will not occur in the high frequency radiation produced as it does when rupture velocity and slip are uniform. As a result the ground motion at high frequencies will most likely appear to be due to radiation from many small sources rather than one large source. The accelerations produced by such models will generally be considerably more complicated than those produced by a uniform rupture propagation model. Examples of this can be found in the parametric studies conducted by Del Mar Technical Associates (1978, 1979).

In this section we will first examine the consequences of a localized source on the near-field attenuation characteristics. The relative spatial distribution of motion will be examined both with and without seismic directivity effects. The absolute levels of acceleration as a function of stress drop and rupture characteristics will be inferred using kinematic models suggested in the seismic literature.

3.2 SPATIAL VARIABILITY AND RADIATION PATTERN

The most fundamental characteristic of the radiation from an isolated dislocation source is the double-couple radiation pattern of P and S waves. As the source of seismic radiation becomes smaller, the radiation from such sources will tend to be like that from an isolated dislocation rather than that shown in the previous section of this report. No source with coherent rupture on some scale will radiate like a point double-couple, no matter how small it is but such a radiation pattern will be appropriate over some limited frequency range.

Though the double-couple radiation pattern is simple to visualize in a whole space, the projection of motion onto the surface of the earth is not, particularly in the near-field. When the observer is within a range of a few source depths of the epicenter, the attenuation of motion with range can be controlled as much by radiation pattern effects as by geometrical spreading and intrinsic attenuation in earth materials. One might expect any coherent rupture effects to add to the complications in the spatial distribution of motions in the near-field so that the variations due to radiation pattern alone could be considered to be the minimum amount of complexity expected.

Expressions for the radiation pattern due to an isolated dislocation can be found in numerous sources (Haksell, 1964; Aki and Richards, 1980, Chapter 4) and need not be reviewed here. The surface projection of the radiation pattern with r^{-1} geometric spreading was computed for strike-slip and dip-slip sources for the

geometry shown in Figure 3.1. For vertical faults the motion is symmetric about the fault plane and about the fault normal for pure strike-slip or dip-slip sources, so only one quadrant need be examined.

Figure 3.2 shows the contours of magnitude of S-wave motion projected to the surface for both types of slip. For strike-slip sources there is a node just above the source. The maximum amplitudes occur in the fault plane and fault normal at an epicentral distance of one source depth. For dip-slip sources the maximum motion occurs just above the source. The attenuation is quite sensitive to the particular azimuth chosen.

The attenuation of motion with distance for azimuths at 0, 45 and 90 degrees from the fault strike are plotted for strike-slip sources in Figure 3.3 and for dip-slip sources in Figure 3.4. For strike-slip sources the motions at azimuths of 0 and 90 degrees are the same. The smallest motions are at an angle of 45 degrees. In the far-field the difference in amplitude is roughly a factor of three. For dip-slip sources the radiation pattern is considerably more homogeneous with azimuth with the exception of the node located at one source depth normal to the fault.

3.3 CONTRIBUTIONS FROM LOCALIZED DIRECTIVITY

Localized coherent rupture on virtually any length scale results in some form of directivity effects which can significantly modify the primary radiation pattern. This is particularly true for the high frequency radiation. It was shown in the previous chapter that the near-field motion from constant dislocation models can be quite sensitive to the rupture characteristics. The same is true for the models examined in this section.

The motion due to a uniformly expanding shear crack is well known. Differences between the various models arise from how the stopping is treated. In general, analytic expressions for the characteristics of the fault slip are not available when the rupture is allowed to stop, although approximations to the behavior of the

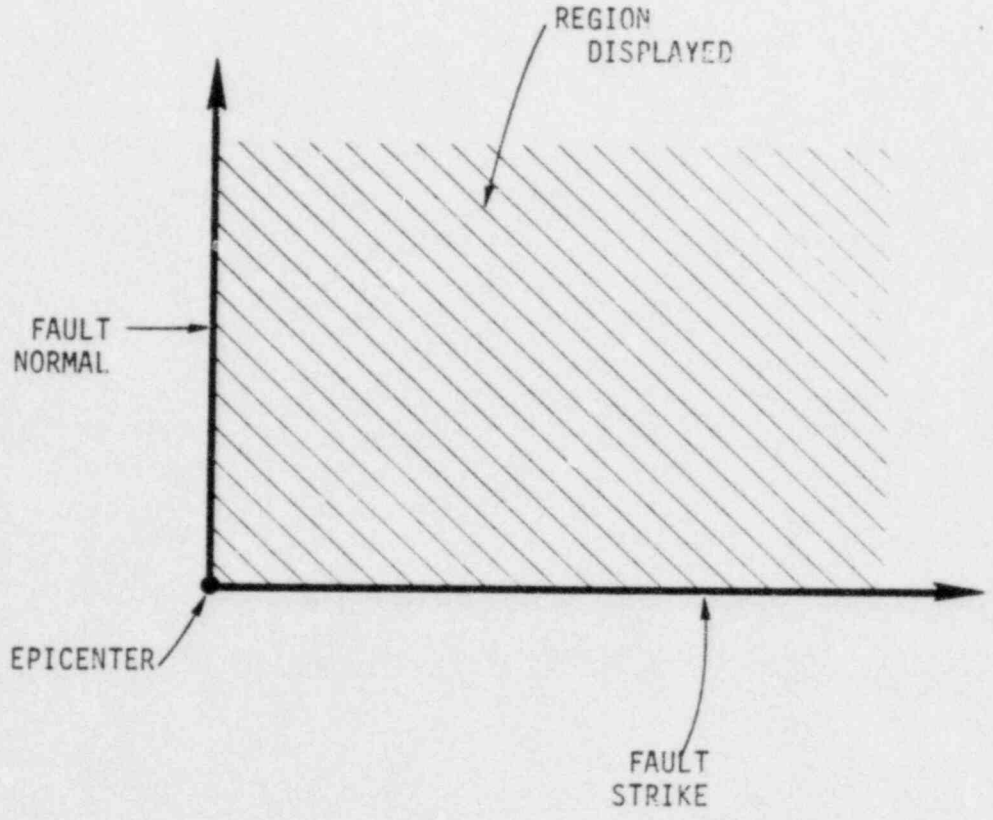

Figure 3.1. Geometry used in surface projections of radiation pattern from concentrated sources to follow.

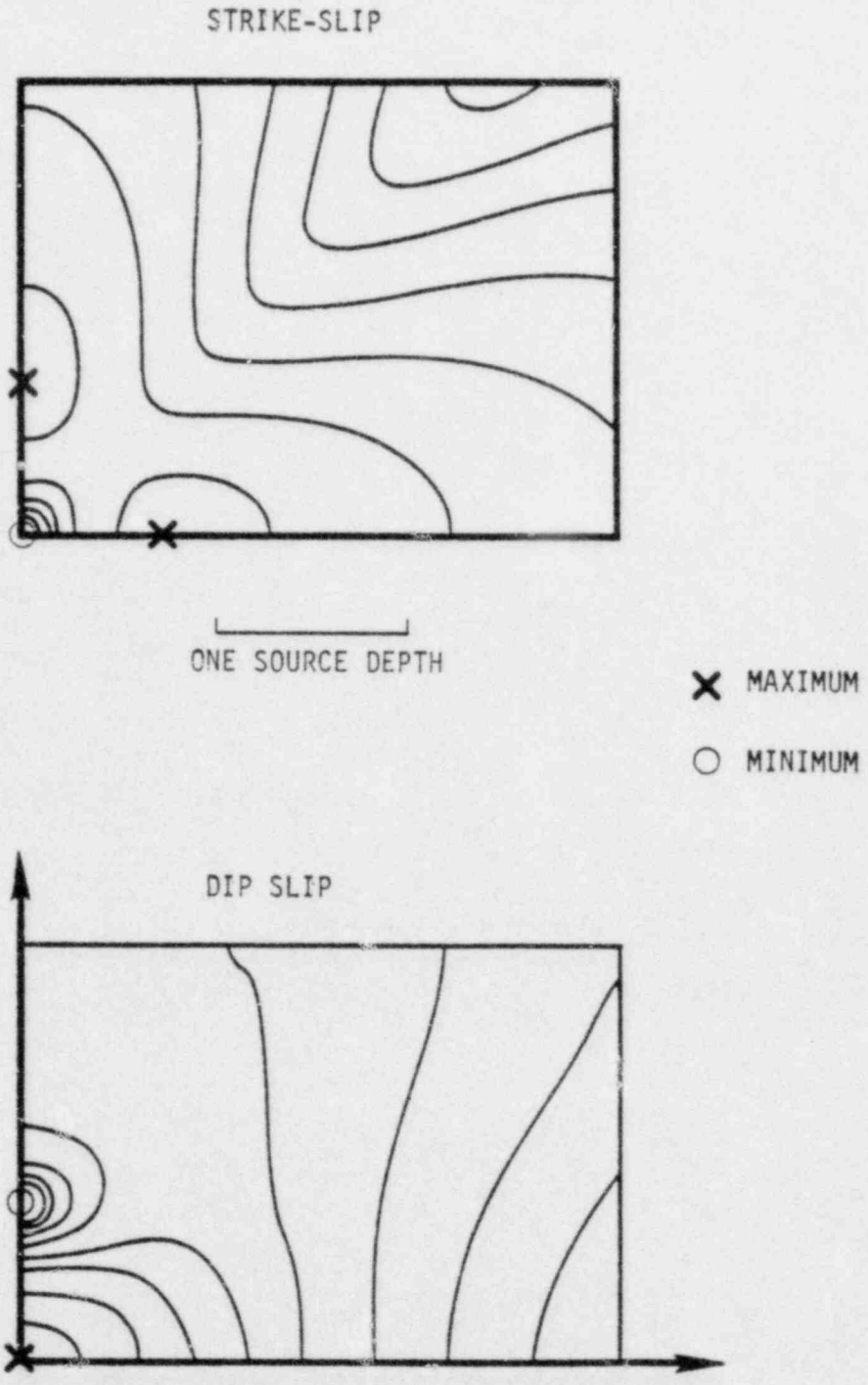

Figure 3.2. Surface project of the double-couple shear wave radiation pattern from a buried dislocation. Amplitudes contoured are the geometric sum of the three components of motion. Contours are logarithmic with every other contour representing a factor of two difference in amplitude.

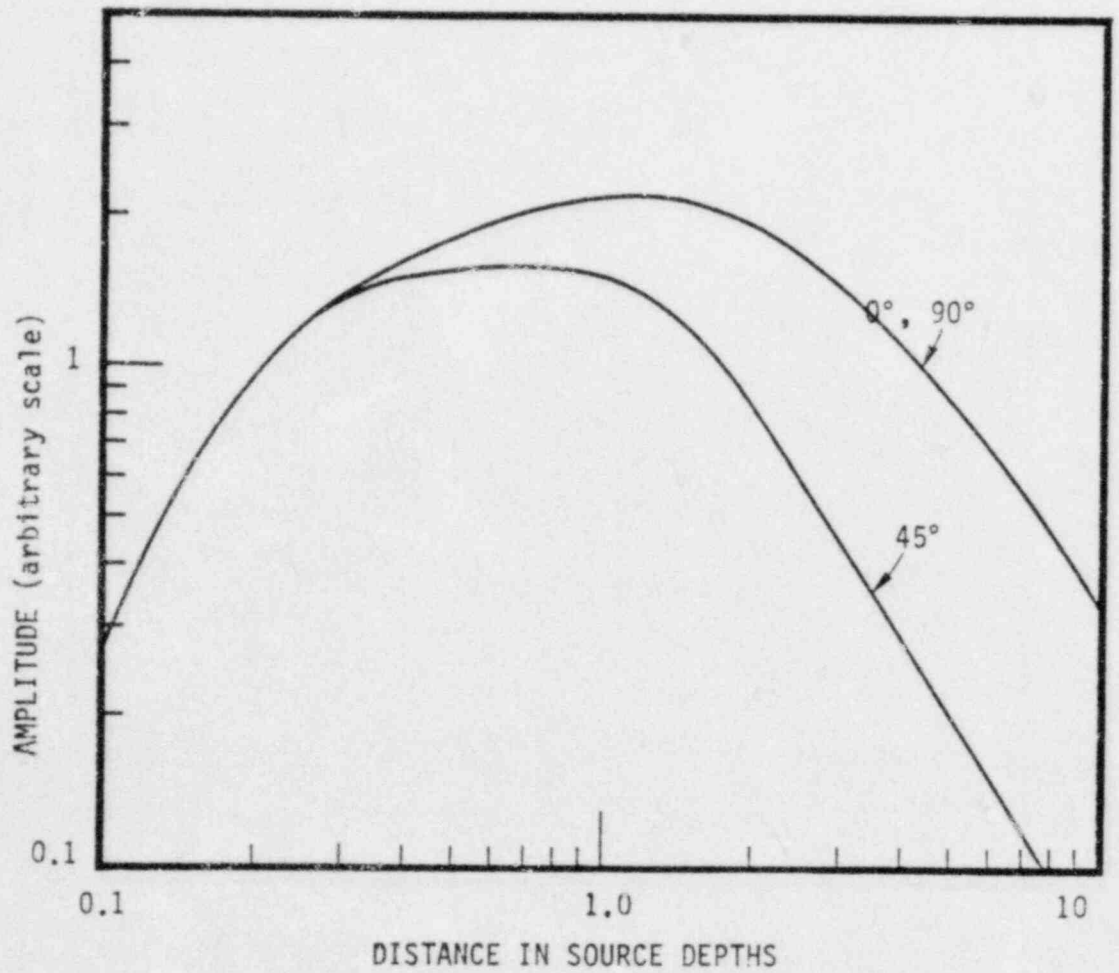

Figure 3.3. Amplitude as a function of epicentral distance from a vertical strike-slip dislocation for three azimuths from the fault strike.

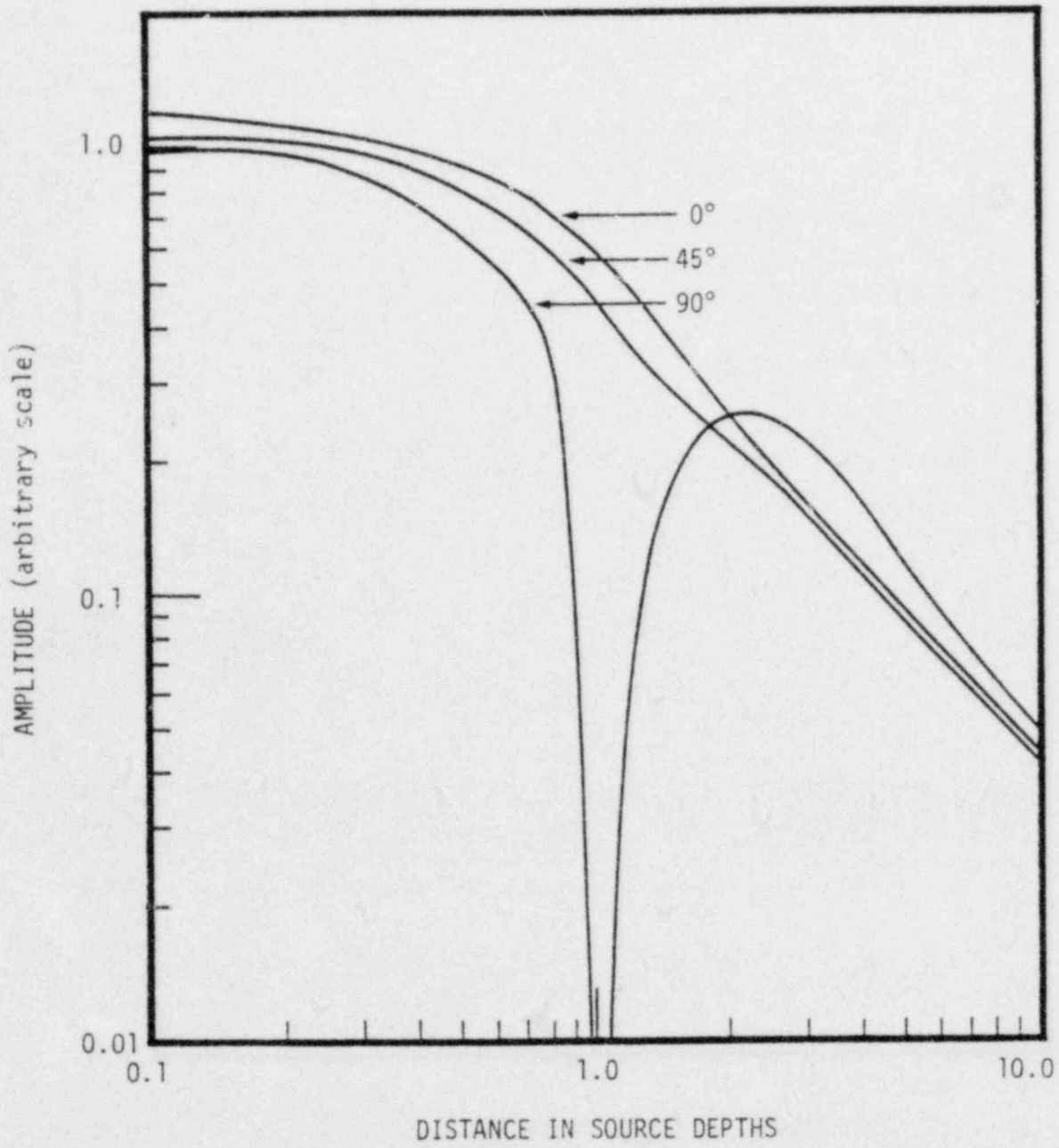

Figure 3.4. Amplitude as a function of epicentral distance from vertical dip-slip source.

faulting have been suggested (Sato and Hirasawa, 1973; Bouchon, 1978, Boatwright, 1980). In this section we will consider only the initial radiation and the effects on the resulting acceleration.

The initial shear wave acceleration from a uniformly expanding shear crack as a function of space and time can be written (Sato and Hirasawa, 1973):

$$\ddot{\vec{u}}(t) = \frac{\dot{D}_0 \, V^2 \, \vec{R}_S}{[1 - (V/\beta \sin\theta)^2]^2 \, \beta r} H(t - r/\beta)$$

where

$\dot{D}_0$ = slip velocity at the center of the crack,

V = rupture velocity,

r = hypocentral distance,

β = shear velocity,

θ = angle from the fault normal,

$\vec{R}_S$ = S-wave double-couple radiation pattern,

$H(t)$ = unit step function,

t = time.

The spatial dependence of the motion contains the double-couple radiation pattern, geometrical spreading factor, and a seismic directivity term $[1 - (V/\beta \sin\theta)^2]^{-2}$. The consequence of directivity is to enhance the motion in the plane of the fault relative to that at the fault normal. If the rupture velocity is near the shear velocity of the medium this effect is quite large. At the fault normal the amplitude dependence is the same as if there were no coherent rupture.

The surface projection of the RMS amplitudes including directivity is shown in Figure 3.5 for the strike-slip source and in Figure 3.6 for dip-slip source for two rupture velocities. For the strike-slip case the distribution of motion is skewed considerably

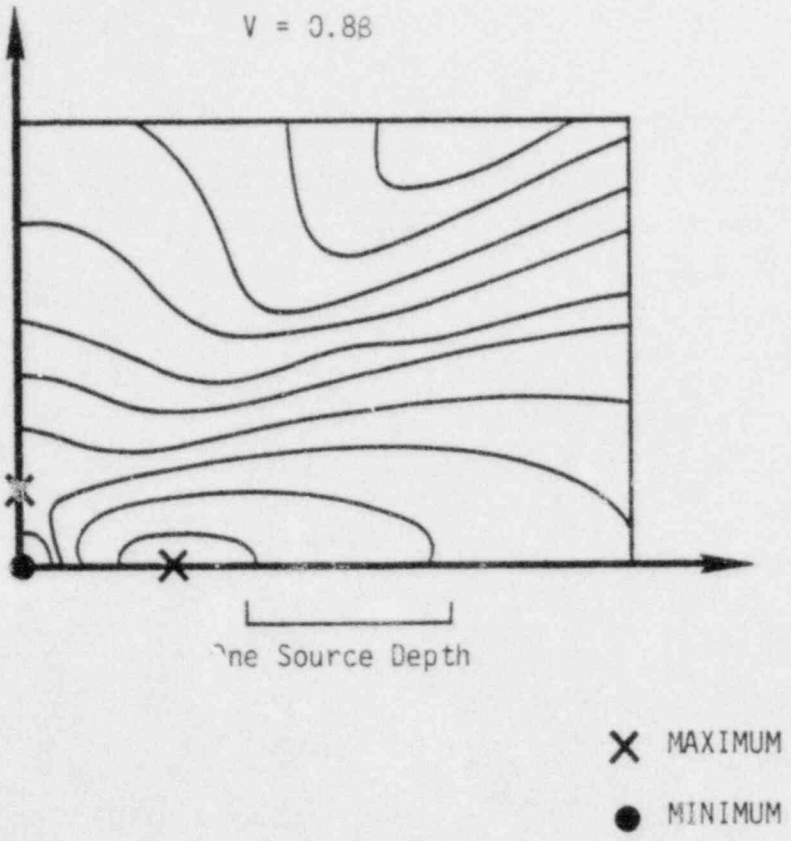

Figure 2.5. Contours of surface acceleration due to shear waves from the initiation of a vertical strike-slip circularly expanding shear crack with uniform rupture velocity. Every other contour represents a factor of two difference.

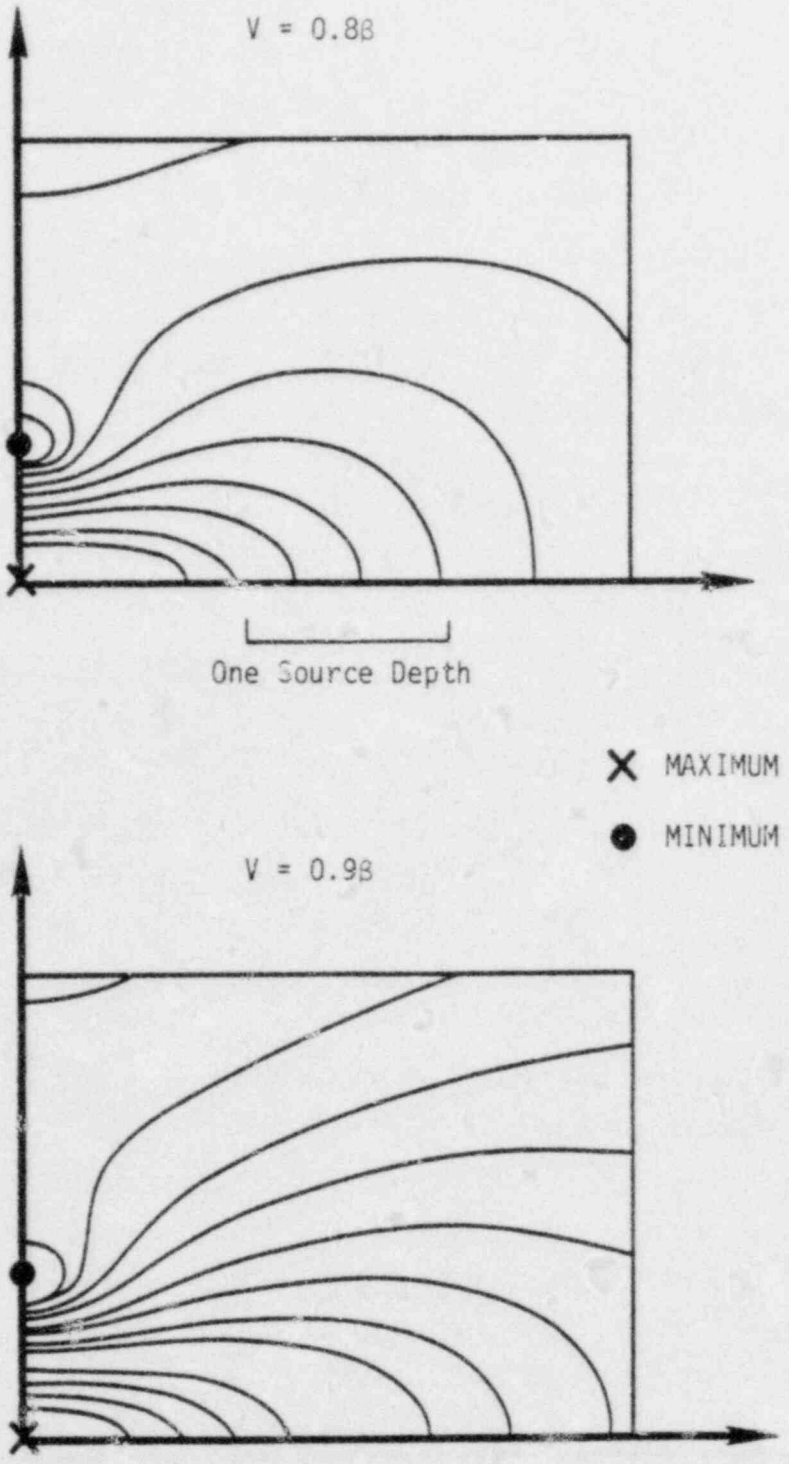

Figure 3.6. Contours of surface acceleration due to shear waves from the initiation of a vertical dip-slip circularly expanding shear crack with uniform rupture velocity. Every other contour represents a factor of two difference.

to enhance the motion in the plane of the fault. The motion in the plane of the fault at an epicentral distance of three source depths is larger than the motion at any distance in the normal direction for a rupture velocity of 0.8 β and nearly so for 0.9 β. Symmetry of amplitudes about the two horizontal axes is preserved. Similar effects are found for the dip-slip case.

Figures 3.7 and 3.8 show the attenuation of motion with distance for the two types of sources with a rupture veocity of 0.8 β. The range of variation with azimuth expected increases significantly. The large variations suggest that if large accelerations result from isolated concentrations of stress release, any coherent rupture may cause the near-field distribution of motion to be highly variable. As a consequence, one or two isolated recordings of the ground motion may not be representative of the ground motion levels at other regions in the vicinity of the source.

The spatial dependences described here are for the motions generated by the initiation of a circular shear crack with uniform rupture velocity. Additional high frequency motions are generated when the rupture is forced to stop. The characteristics of such motion will be discussed in Subsection 3.5.

3.4 PARAMETERIZATION OF DISTANCE FROM THE FAULT

The most commonly used parameterization of distance for use in attenuation relationships is the nearest distance to the rupture surface. This choice assumes that the faulting closest to the observer is the most likely source of the high frequency radiation. Though this is convenient and possibly is more reasonable than alternatives suggested, there is some doubt that evidence of permanent slip necessarily implies a source of high frequency radiation. In the 1971 San Fernando, California, earthquake, for example, static and long period dynamic studies have suggested a very large fault surface (Alewine, 1974; Heaton and Helmberger, 1979) while studies of the high frequencies tend to suggest radiation eminating from smaller, more concentrated regions (Hanks,

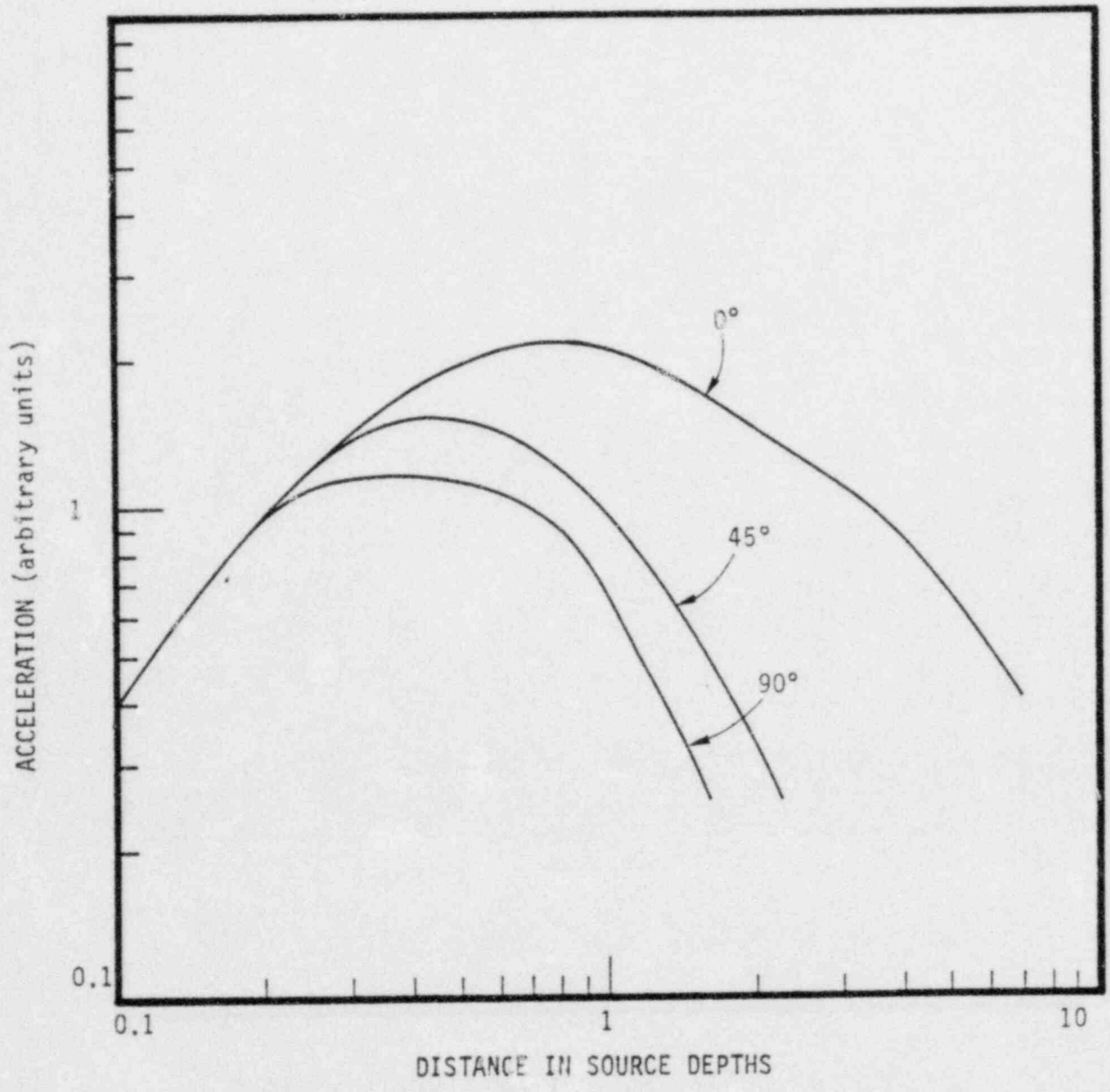

Figure 3.7. Acceleration as a function of epicentral distance from the initiation of uniformly expanding vertical strike-slip shear crack at three azimuths. Rupture velocity is 0.8β.

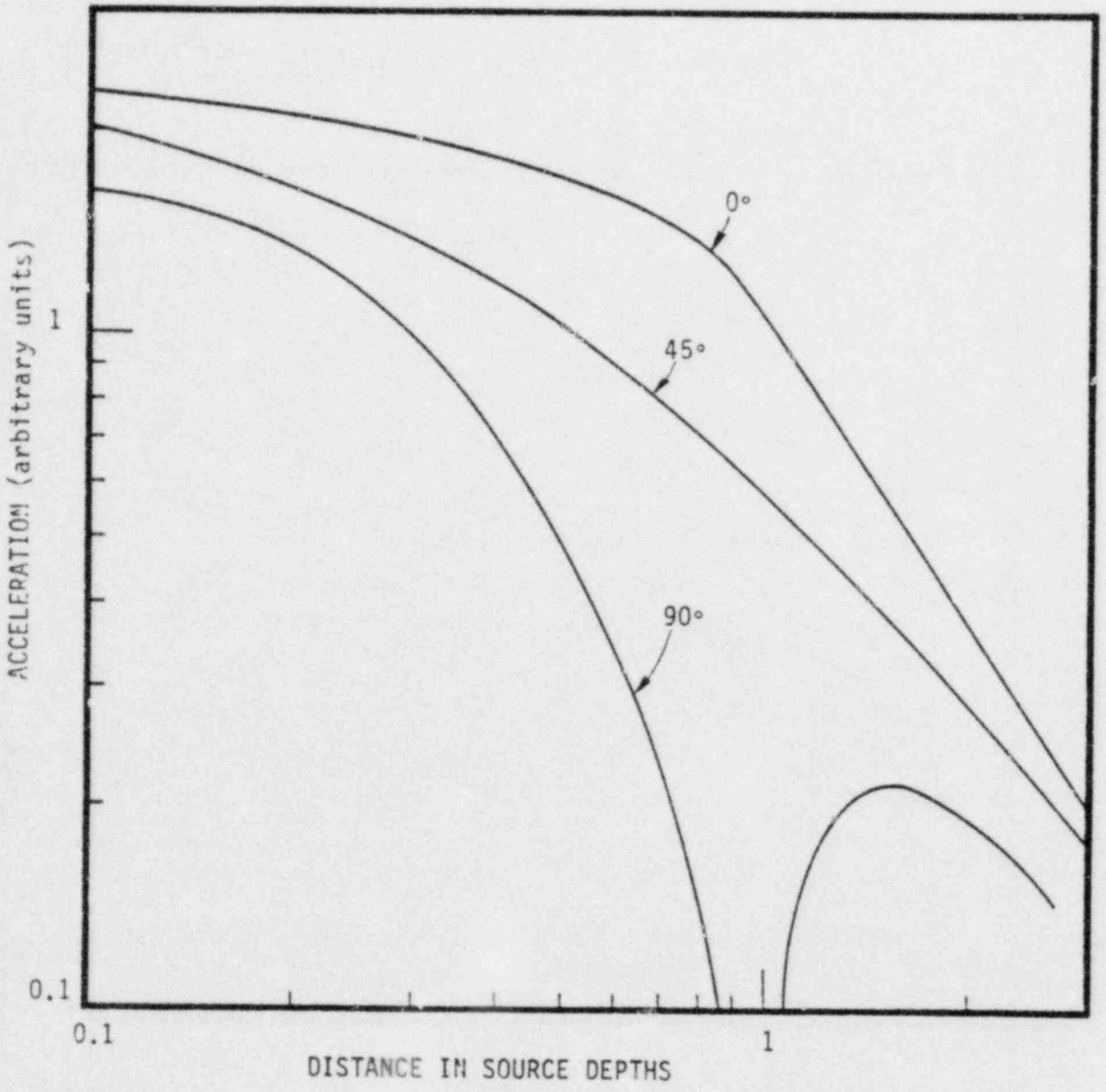

Figure 3.8. Acceleration as a function of epicentral distance from the initiation of uniformly expanding vertical dip-slip shear crack at three azimuths. Rupture velocity is 0.8β.

1974; Bache and Barker, 1978; Bouchon, 1978). In the 1966 Parkfield, California, earthquake it has been suggested that the inferred timing of the largest motion observed in the perpendicular array is consistent with the with a disturbance located at Gold Hill, 10 km to the north of the array and not from the slip which occurred nearest the array (Lindh and Boore, 1973). In this section we examine the consequences on attenuation relationships using the closest slip measure of distance if the motion is actually due to a stress concentration on some other point on the fault surface.

Suppose we are given the geometry in Figure 3.1 and the largest motions radiate from the origin as in the previous cases. If slip on the fault were evident along the fault strike, the distance from the source would usually be taken from the horizontal axis and not from the origin as in the previous plots. Figures 3.9 and 3.10 show the attenuation of motion from the fault strike at distances of one, two and three source depths from the actual source for two rupture velocities. Note that in each case, we observe a "roll-over" or change in slope in the rate of decay with distance as one approaches the fault plane. Such an effect has been hypothesized for the near-field (Donovan, 1973; for example), and appears consistent with some data sets like the 1979 Imperial Valley earthquake. The constant dislocation models examined in the previous section did not show such prominent roll-over in near-field attenuation of acceleration.

If one compares the observed maximum horizontal accelerations from the Imperial Valley earthquake located along a perpendicular line from the fault (Stations 1 through 13) to the decay suggested by the initiation of a crack located at the published hypocenter (Porcella and Matthiesen, 1979), one finds very good agreement (Figure 3.11). For purposes of this calculation, a rupture velocity of 0.8 β was assumed and amplitudes are scaled to match the average of stations 6 and 7 at a distance of 1 km. The agreement here is not to suggest that a concentrated release of energy is necessarily

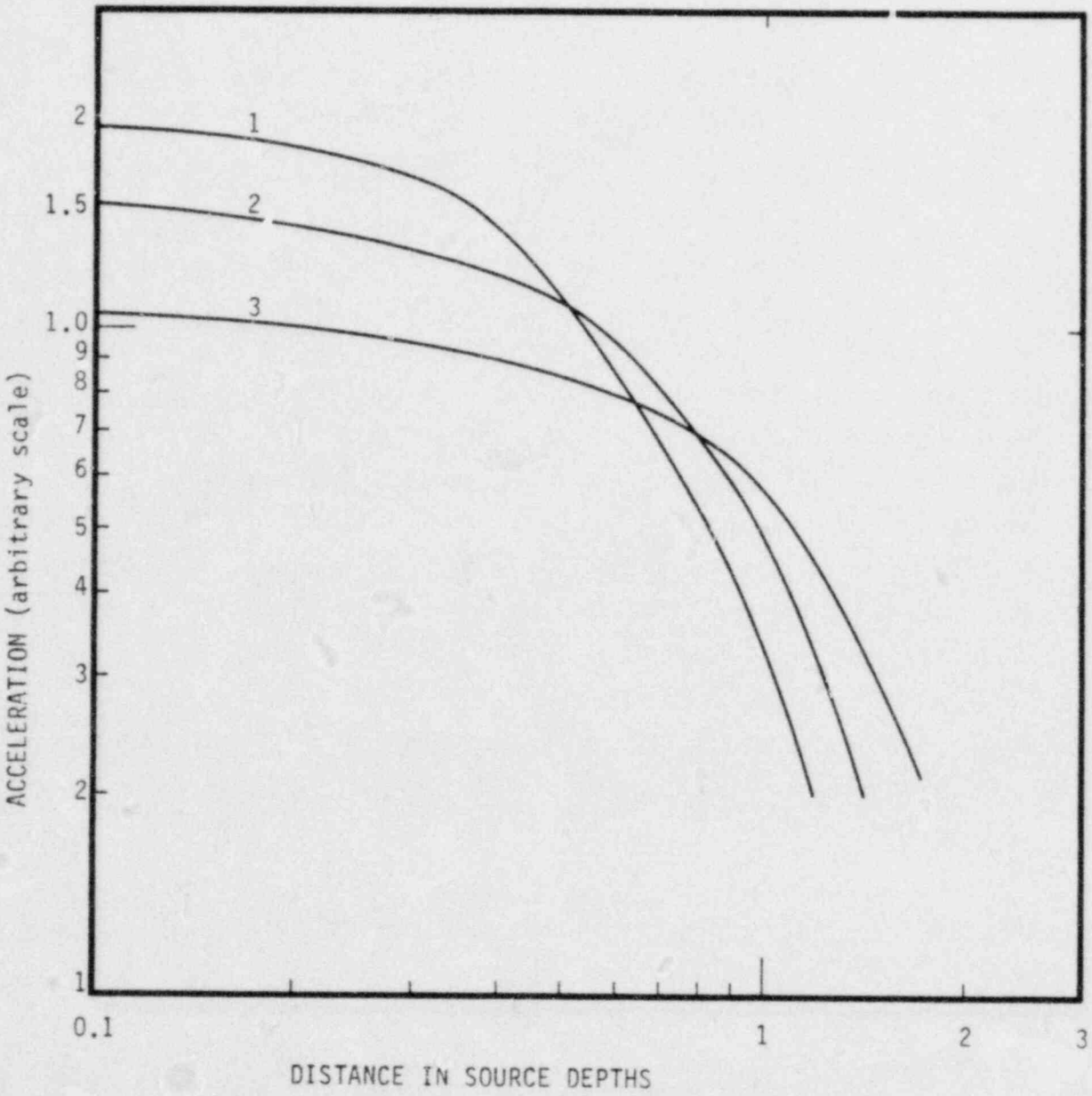

Figure 3.9. Acceleration versus distance along a perpendicular line from the fault strike for a vertical strike slip fault. Curves are labeled by the number of source depths from the epicenter along the fault strike to the profile. Rupture velocity is 0.88.

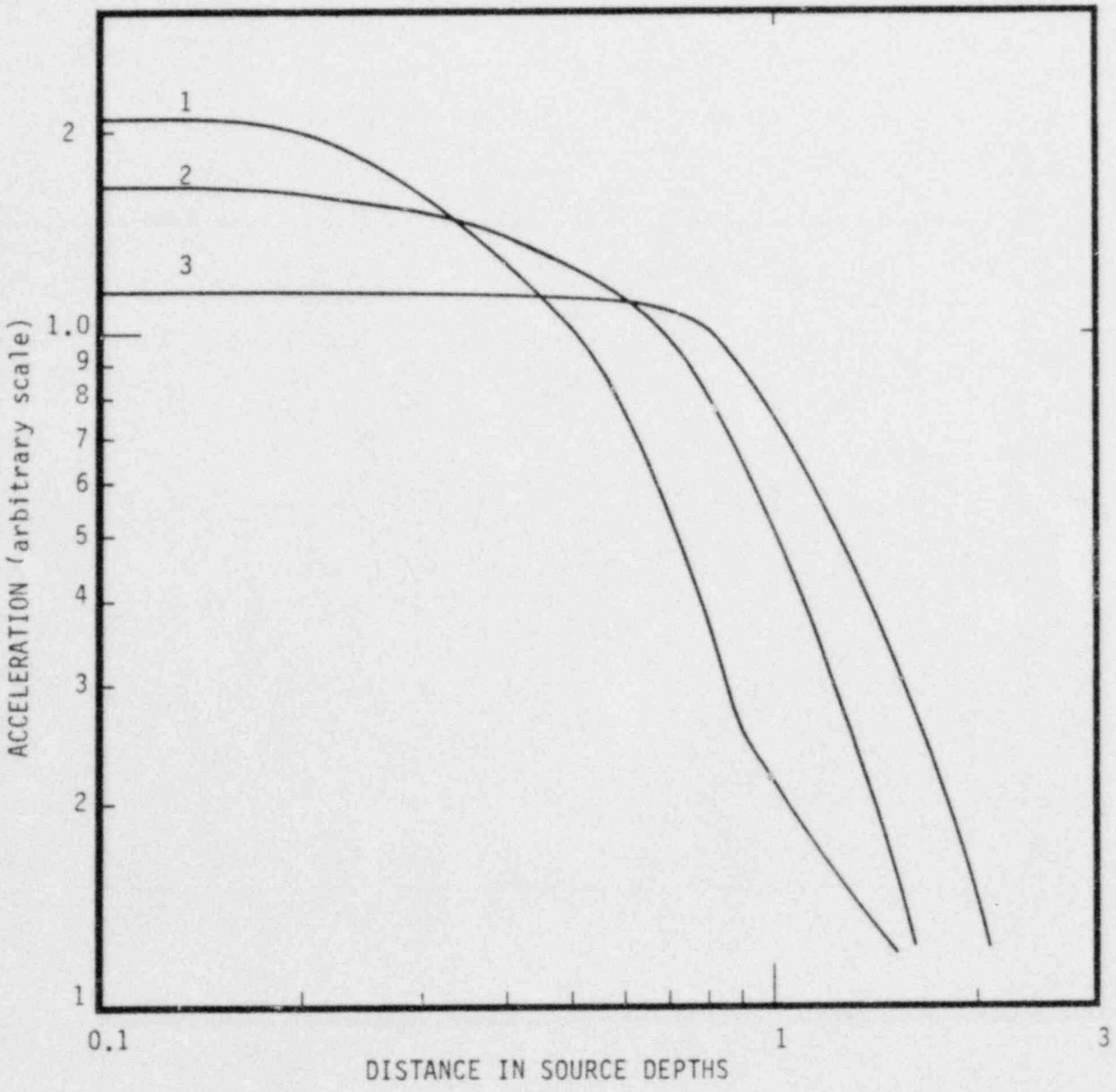

Figure 3.10. Acceleration versus distance along a perpendicular line from the fault strike for a vertical strike-slip fault. Curves are labeled by the number of source depths from the epicenter along the fault strike to the profile. Rupture velocity is 0.9β.

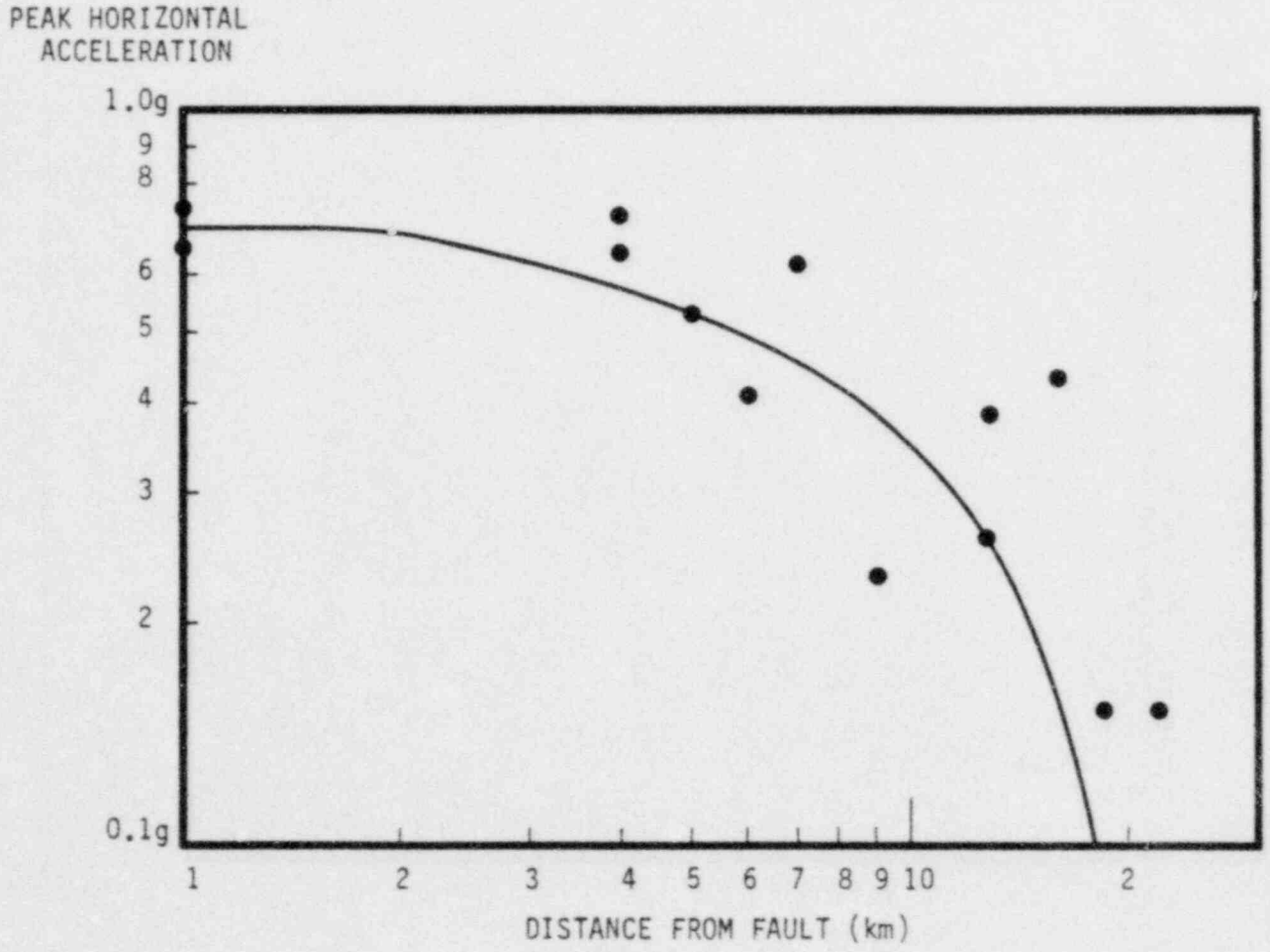

Figure 3.11. Decay of peak acceleration predicted from the initiation of a crack at the published hypocenter to the peak horizontal accelerations observed at Stations Number 1 through Number 13 in the 1979 Imperial Valley earthquake. Computed accelerations scaled to the average of Stations Number 6 and 7. Rupture velocity is 0.88.

a good model of this particular earthquake, but it demonstrates that an isolated stress concentration can produce reasonable near-field rates of attenuation. For vertical strike-slip faulting, the use of closest distance from the fault as a distance parameterization may not be reasonable unless one anticipates a scatter in the amplitudes of possibly a factor of two, if indeed the energy radiates primarily from localized sources.

3.5 AMPLITUDES OF NEAR-FIELD ACCELERATION AND LOCAL CONCENTRATIONS OF STRESS

In the previous sections, only the relative spatial dependence of the computed peak amplitudes were examined. In this subsection, the absolute amplitudes of near-field acceleration suggested by kinematic models of stress concentrations will be considered. In most models of the stress release, there are two distinct facets to the radiation of high frequencies which must be considered separately, namely, contributions due to the initiation and termination of the rupture. Boore (personal communication, 1980) has examined various kinematic models of localized stress concentrations and noted that all of the well known models of this type tend to emphasize either the starting or stopping effects of the rupture propagation. Those models emphasizing one or the other effect tend to give results which are consistent with other models employing the same basic assumptions.

The model of Sato and Hirasawa (1973) includes contributions from both the starting and stopping of rupture and this model will be emphasized here. Expressions for the radiation from the initiation of rupture were presented earlier. The stopping of the rupture is assumed to be instantaneous over the entire fault surface. This could be considered an extreme case. There are many other ways in which stopping can be treated, and Boatwright (1980) suggests a variety of possible alternatives.

The expression for the acceleration due to crack initiation was given in Section 3.3. That formula relates acceleration to the

velocity of slip at the initiation point on the fault and this quantity is nearly proportional to stress drop. Complicated expressions relating the two quantities were first derived by Kostrov (1964) and, subsequently, Danlen (1974) evaluated these expressions from various rupture velocities. A good approximate relationship for rupture velocities considered here is

$$\dot{D}_0 \approx 0.8\, V \frac{\sigma}{\mu}$$

where $\dot{D}_0$ is the slip at the center of the fault, V is the rupture velocity, σ is the stress drop and μ the material shear modulus.

Using the above approximation, we have evaluated the acceleration peak amplitudes radiated from the rupture initiation as a function of rupture velocity and azimuth for a fixed stress drop and observation distance. The results are shown in Figure 3.12 for the case in which the stress drop was fixed at 100 bars and the distance at 10 km. A shear velocity of 3.3 km/sec and density of 2.7 km/cm^3 were selected for purposes of illustration. The double-couple radiation pattern, which is always less than unity, is not included. The response of the earth, particularly the interaction at the earth's surface, would, in general, increase the amplitudes given here by a factor on the order of two.

For fixed stress-drop there is clearly a strong dependence on rupture velocity. At the fault normal, the amplitudes are proportional to rupture velocity cubed. In the plane of the fault amplitudes vary by a factor of five for rupture velocities between 0.8 and 0.9 times the shear velocity. If the initiation of rupture at a stress concentration is the cause of large accelerations, high stress drop and/or rupture velocities near the shear velocity are implied.

The amplitudes of the stopping phases predicted by the Sato and Hirasawa (1973) model are somewhat more difficult to quantify since the model suggests singular accelerations. The shear wave accelerations radiated in this case can be expressed by the relation

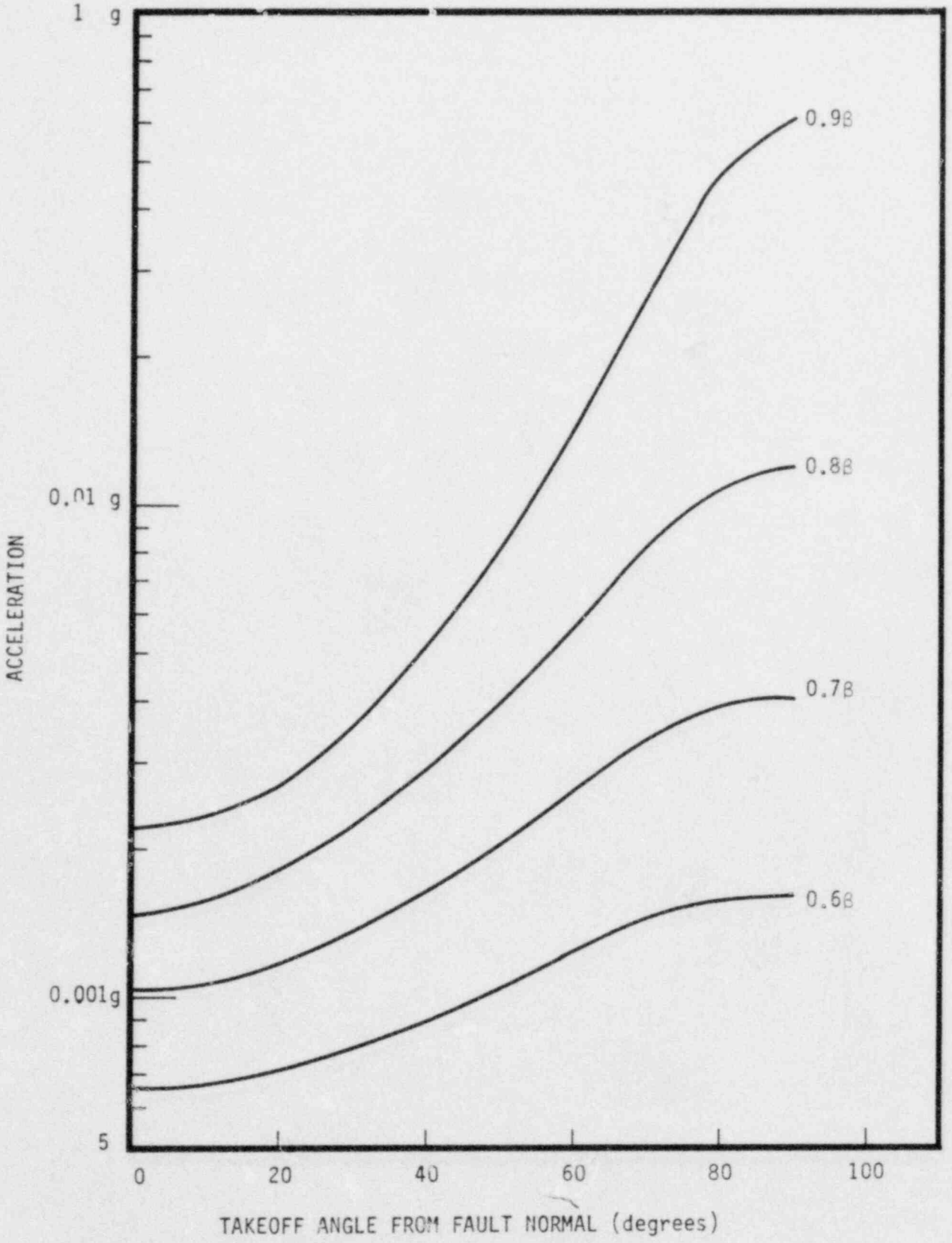

Figure 3.12. Peak acceleration from the initiation of a shear crack with a stress-drop of 100 bars observed at a hypocentral distance of 10 kilometers for various rupture velocities and takeoff angles.

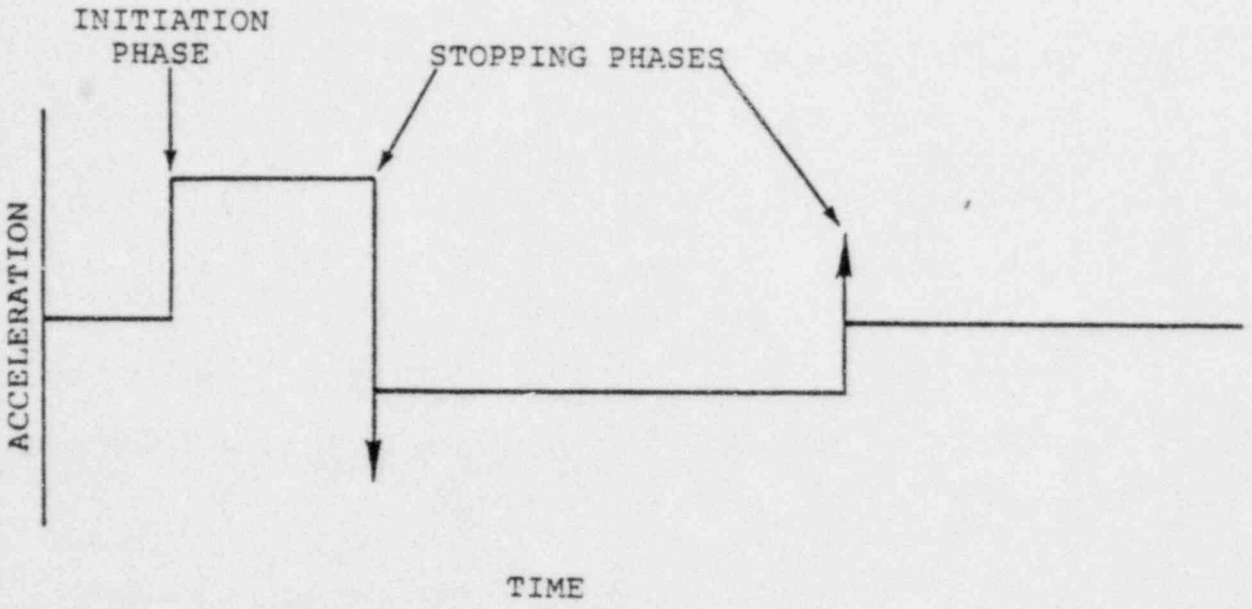

Figure 3.13. Typical shape of the Sato and Hirasawa model geometrical far-field acceleration. Arrows represent delta functions.

$$\ddot{\vec{u}}(t) = \frac{\dot{D}_0 V^2 \vec{R}_s}{\beta r (1-K^2)^2} \left| H(t') - H(t' - \frac{L}{V}(1-K)) \right|$$

$$- \frac{\dot{D}_0 V^2 \vec{R}_s}{4\beta r K(1+K)^2} \left| H(t' - \frac{L}{V}(1-K)) - H(t' - \frac{L}{V}(1+K)) \right|$$

$$- \frac{\dot{D}_0 V L \vec{R}_s}{4\beta r K(1-K)} \delta(t' - \frac{L}{V}(1-K))$$

$$+ \frac{\dot{D}_0 V L \vec{R}_s}{4\beta r K(1+K)} \delta(t' - \frac{L}{V}(1+K))$$

where L is the fault radius, $K = V/\beta \sin\theta$, $t' = t - r/\beta$ and $\delta(t)$ is the Dirac-delta-function. The characteristic shape of this far-field ($r >> L$) acceleration is shown in Figure 3.13 where it can be seen that the singular behavior of this motion leads to unrealistic ground motions. The response of the earth will probably not permit accelerations to become too large, and, in any case, the frequency band of interest in hazard assessment is limited.

However, even when the accelerations predicted by this stopping model are viewed through a realistic passband, the absolute level of the peak accelerations can become unreasonably large (>10 g) at some azimuths suggesting that this model is not plausible.

3.6 CONCLUSIONS

In this Section we have examined the consequences of high frequencies radiated from isolated stress concentrations using kinematic approximations to the dynamic stress release process. The major conclusions of this Section are:

1. If the high frequency motion is dominated by radiation from isolated sources rather than from uniform radiation from the entire fault surface, there is likely to be considerable variability in

the peak motions within a few source depths of the disturbance due to radiation pattern alone. Thus, in such a case, a single close in station may not be representative of the largest motions from the source.

2. Coherent rupture accompanying the stress release will increase the variability of the motion by increasing the radiation in the plane of the fault independent of the length scale over which the rupture is coherent.

3. The distance attenuation relationship derived using closest distance to the entire fault (not the stress concentration), can lead to very reasonable looking results, but the relationships obtained may not be representative of the levels of motion over the entire fault.

4. When stopping of rupture is included in these models, the stopping phases radiated dominate the high frequency motions. The levels of motion suggested by existing kinematic approximations are too large to be realistic. That is, as is the case of the constant dislocation models considered in Section II, abrupt termination of the rupture propagation leads to unreaslistic near-field ground motion characteristics.

IV. DYNAMIC EARTHQUAKE MODELS WITH FIXED-RUPTURE-VELOCITY

4.1 INTRODUCTION

Dynamic earthquake models are models in which the initial stresses acting along a fault are assumed known; in contrast to kinematic models, no *a priori* assumptions are made about the form of the fault slip. The fault slip is obtained as part of the dynamic modeling process.

We can distinguish two types of dynamic earthquake models which have been investigated. In the first type, the rupture history, i.e., the growth of the fault surface, is prescribed. This will be referred to as the fixed-rupture-velocity model. In the second type, the constitutive properties of the fault plane, or fault zone, are prescribed, and the subsequent growth of the rupture is not prescribed *a priori*, but results from the constitutive properties, the prestress, and the ensuing dynamic stresses in the medium. This will be referred to as the spontaneous rupture model.

The current section deals with the fixed-rupture-velocity model. In particular, we will attempt to characterize the slip function for the dynamic model, compare this "dynamic" slip function with slip functions previously used in kinematic modeling, and assess the importance of various modeling assumptions in controlling the near-field ground motion characteristics predicted by this type of model. All but the most elementary dynamic crack problems (those for which closed-form solutions exist) require extensive numerical computation in order to obtain ground motion predictions. Since such numerical computation is beyond the scope of this study, we will focus primarily on analyzing numerical results obtained in earlier dynamic studies.

Closed-form theoretical solutions are available for only the most idealized cases. Restricting consideration to three-dimensional analyses, probably the most advanced and useful of such analytical results is the solution of Burridge and Willis (1969). That solution gives the slip history on an elliptical shear crack

which initiates at a point in a prestressed whole-space and grows at a fixed rupture velocity without stopping. While this theoretical result is very useful for interpreting the results of more complex numerical studies, it cannot be applied directly to strong motion simulation, since it cannot account for effects of the stopping of rupture growth and the cessation of slip which ensues.

Numerical methods have been applied to investigate fixed-rupture-velocity faulting in which rupture is confined to circular regions (Madariaga, 1976), semi-circular regions (Archuleta and Frazier, 1978), and rectangular surfaces (Madariaga, 1977; Day, 1979; Archuleta and Day, 1980). Generally, in these simulations, rupture is prescribed to originate at a point and to grow at constant rupture velocity until a prescribed region of the fault plane is encompassed (an exception was the study by Madariaga (1977), in which rupture was initiated simultaneously across the fault width, in order to facilitate comparison with the kinematic model of Haskell (1964)).

The simulations performed by Day (1979) will provide the basis for the subsequent analysis. The main reason for this emphasis is that high-frequency, near-source motion was the particular focus of that investigation. The other work cited focused on the far-field waveform and/or on low to intermediate frequency (say one Hertz) ground motion.

Following the investigations cited above, we will characterize the fixed-rupture-velocity dynamic model by the following assumptions:

1. Rupture initiates at a point.
2. Subsequent rupture growth occurs at constant, prescribed rupture velocity until a prescribed region of the fault plane is encompassed.
3. Stress-drop is prescribed to be uniform over the fault plane.
4. Rupture growth stops abruptly at the fault edge.

5. Material behavior outside the rupture surface is linear, so that the solutions scale with the prescribed stress-drop.

The remainder of this chapter is divided into four parts. Section 4.2 deals with the slip functions predicted by the fixed-rupture-velocity earthquake model. The role of fault dimension in controlling the slip is particularly emphasized, and the final product is a closed-form approximation to the slip function predicted from the fixed-rupture-velocity dynamic model.

The slip function derived in Section 4.2 is compared in Section 4.3 with some constant-dislocation kinematic models previously employed in ground motion simulation studies. In Section 4.4, we examine the consequences of some of the main modeling assumptions. We note the sensitivity of the ground motion predictions to the prescribed rupture velocity, as well as the dominance of stopping phases. Section 4.5 summarizes our assessment of the fixed-rupture-velocity models.

4.2 SLIP FUNCTIONS FOR FIXED-RUPTURE-VELOCITY MODELS

4.2.1 Introduction

Our primary objective in this section is to develop an approximate analytical expression for the slip function for the fixed-rupture-velocity dynamic model. Actually, the slip function obtained from dynamic modeling is spatially varying over the fault surface. It is found, however, that the initial onset of slip, for points on the fault more than one fault width removed from the hypocenter, is spatially quite uniform. This slip function will be designated the "dynamic slip function," s_d, and will be compared in the subsequent section to some slip functions which have been widely employed in kinematic modeling studies, but which are not based on rigorous dynamic solutions.

4.2.2 Dependence of Slip Function on Stress Drop and Fault Width

As a first step, we analyze the relationship of the slip function to fault width and stress drop, on the basis of the

parametric study by Day (1979). In that study, several finite difference simulations were performed for a fixed-rupture-velocity, rectangular fault surface in a uniform wholespace, with rupture initiated at the center of the rectangular fault, as shown in Figure 4.1. The prestress direction was aligned with the long dimension of the fault in each case. The fault width w was varied, while the following parameters were held fixed for all calculations:

P wave velocity	α	= 6.0 km/sec
S wave velocity	β	= 3.46 km/sec
Density	ρ	= 2.7 gm/cm^3
Rupture velocity	V_R	= 3.12 km/sec
Stress drop	$\Delta\sigma$	= 100 bars

Stress Drop Scaling: Stress drop, $\Delta\sigma$, is here defined to be the difference between the shear prestress and the sliding frictional stress. This quantity has also been called "effective stress" by some investigators. For the fixed-rupture-velocity dynamic model, as defined in Section 4.1, the slip time function which is obtained as a result of the modeling process scales directly with the assumed value of $\Delta\sigma$.

The relationship of $\Delta\sigma$ to the so-called static stress drop is a possible source of confusion. In the dynamic model results discussed here, static stress drop is nearly equal to $\Delta\sigma$ over most of the fault, since no physical mechanism is incorporated into the model to pin the fault at a stress level higher than the prescribed sliding frictional level. In practice, however, seismic estimates of static stress drop are actually estimates of average static offset divided by gross fault dimension. If an earthquake leaves unbroken patches, or if some regions heal at stress levels above the dynamic friction level, then the seismically inferred static stress drop may be substantially lower than $\Delta\sigma$. Static stress drop estimates represent, in general, a lower bound on $\Delta\sigma$.

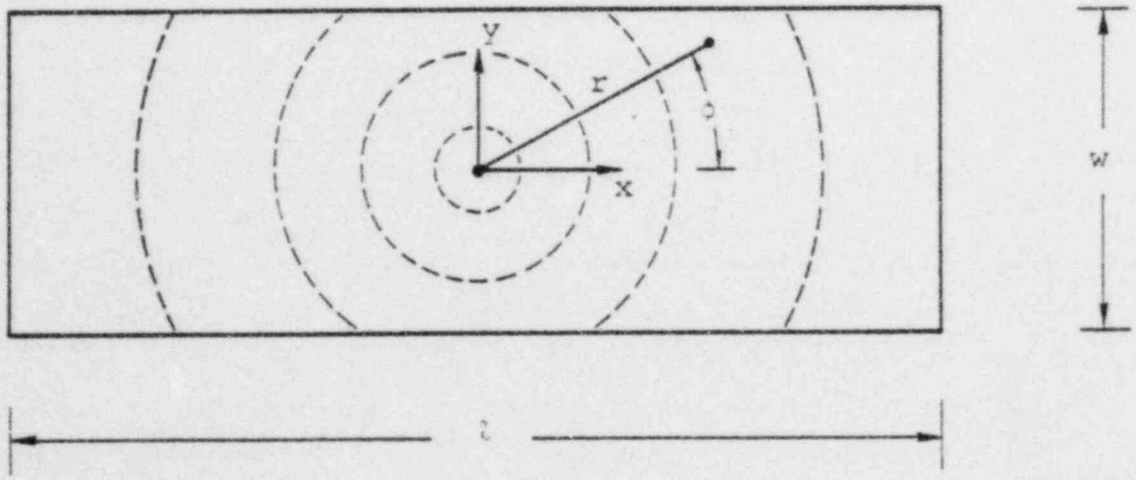

Figure 4.1. Rupture geometry and coordinate system for fixed-rupture-velocity model.

Effect of Fault Width: We will use the static slip and the rise time to characterize the low-to-intermediate frequency behavior of slip in the dynamic simulations. Peak slip velocity will be used to characterize the high-frequency behavior of the slip function, which is of primary importance for predicting high frequency ground motion.

Figure 4.2 shows the static slip along the fault centerline for fault width w = 4 km and w = 1.5 km (with fault length ℓ = 8 km in both cases). The horizontal lines show the static solution for an infinitely long fault (Knopoff, 1958). Except near the end of the fault, the static slip is essentially constant along the length of the fault, and is very well predicted from Knopoff's static solution, according to which the static slip on the fault centerline is

$$S(\infty) = \frac{\Delta\sigma}{\rho\beta^2} \, w \quad . \tag{4.1}$$

Figure 4.3 shows the slip rise times τ_R along the fault centerline for w = 4 km and w = 1.5 km (ℓ = 8 km). Rise time was defined to be the time required to attain 90 percent of the static value of slip. The horizontal lines represent the time for a shear wave to travel from the edge to the centerline. For w = 1.5 km, the rise time at first decreases with distance from the hypocenter, then approaches a constant level of $w/2\beta$. For w = 4 km, the rise time again decreases with distance from the center, but the effects of the end of the fault interfere to further reduce the rise time before a constant level can be established. It appears that an appropriate value for the rise time, for points on the fault centerline more than a fault width away from the hypocenter, is approximately

$$\tau_R = \frac{w}{2\beta} \tag{4.2}$$

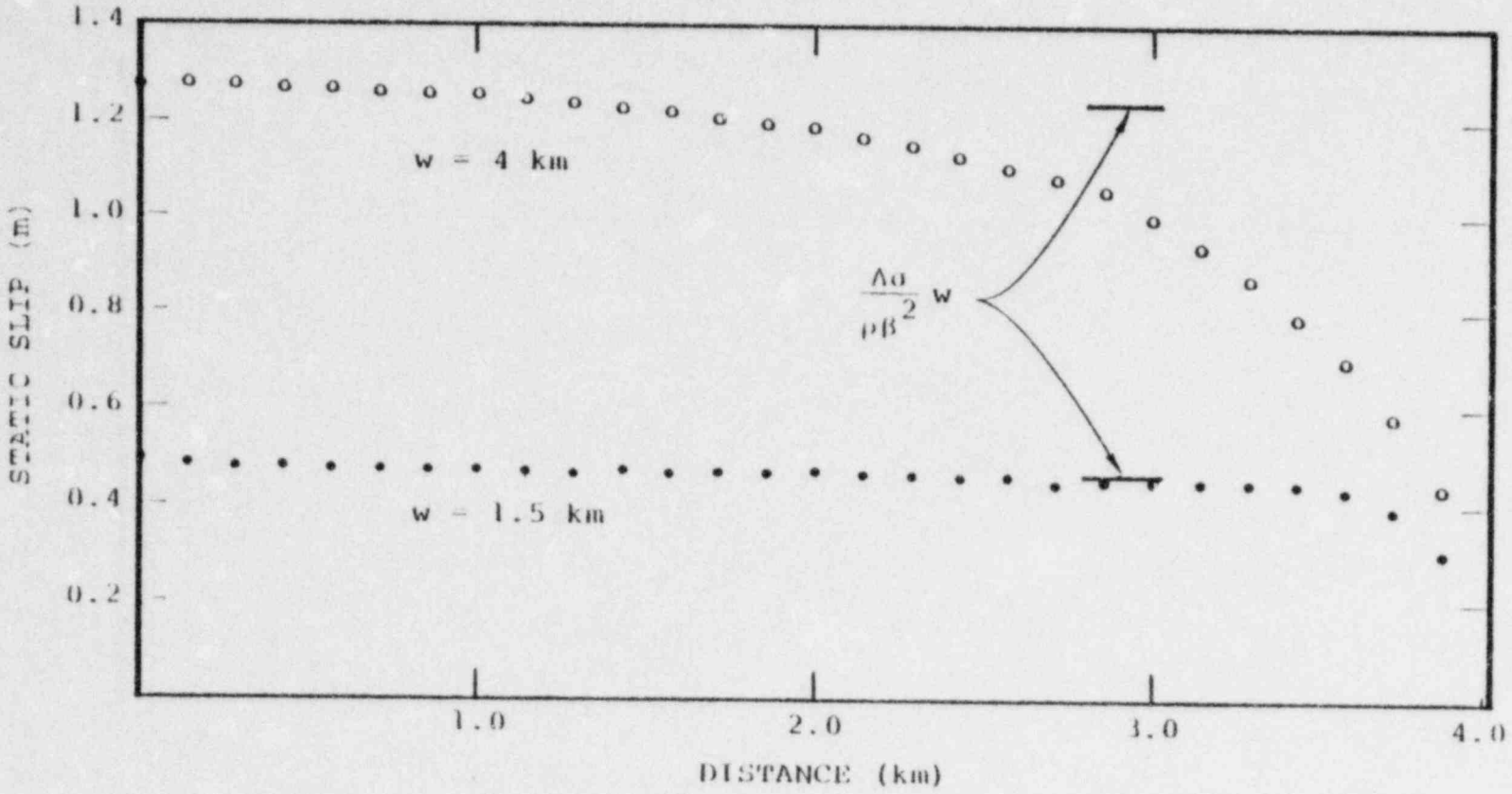

Figure 4.2. Static slip along the center-line of the fault, as a function of distance from the focus, the 4 km x 8 km and 1.5 km x 8 km faults.

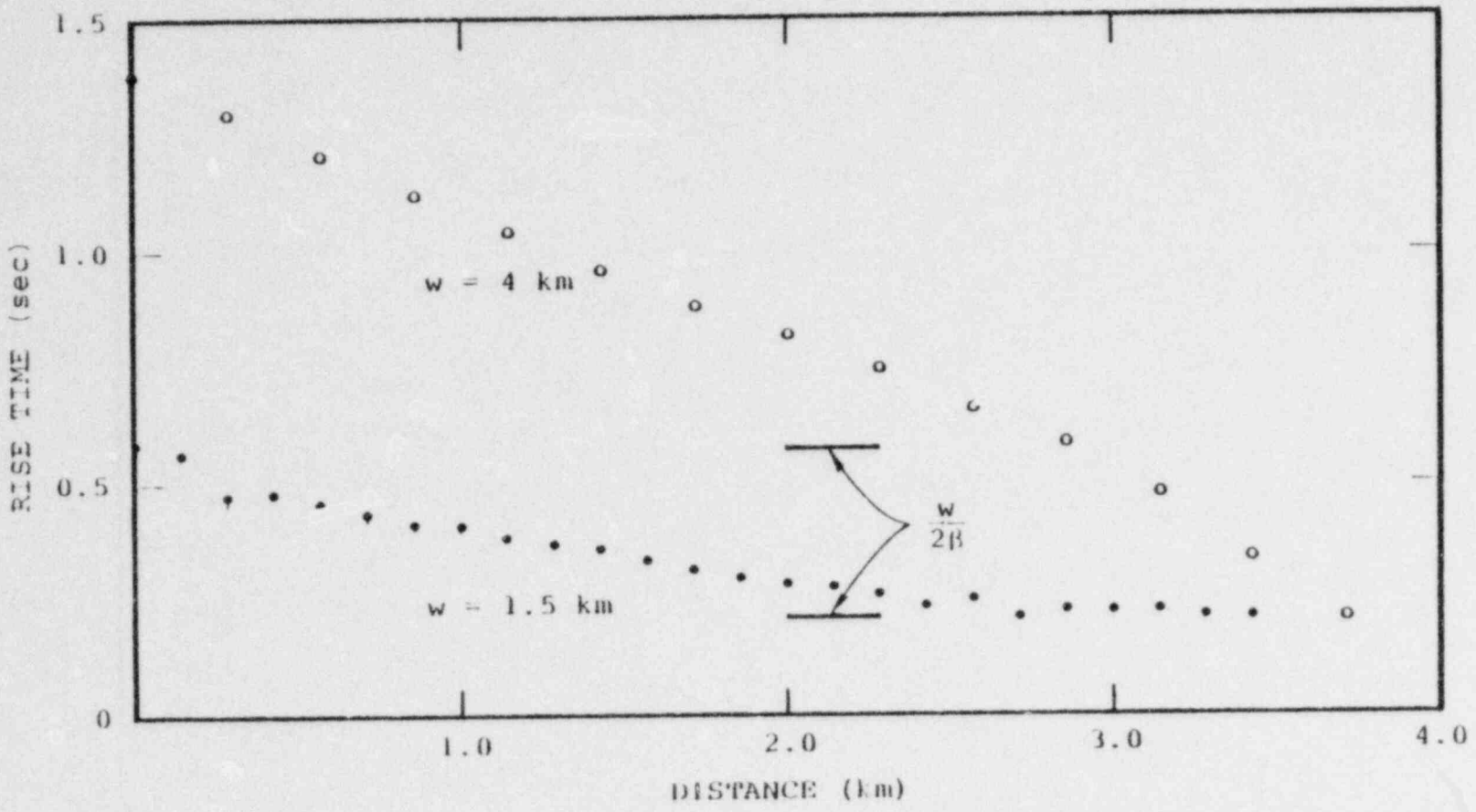

Figure 4.3. Rise time obtained along the center-line of the fault, for the 4 km x 8 km and 1.5 km x 8 km faults.

We turn our attention now to the high frequencies. Here it is appropriate to focus on the slip velocity function, and particularly on the peak slip velocity. The potential importance of peak slip velocity for strong motion prediction has been demonstrated by the kinematic earthquake simulation studies of TERA/DELTA (Del Mar Technical Associates, 1978). They found that near-field response spectral predictions, for frequencies above about 1 Hz, were proportional to the assumed peak slip velocity in their earthquake model.

Figure 4.4 illustrates the spatial variation of peak slip velocity for the dynamic models. The broken curves represent the peak slip velocities (low-pass filtered, with a 5 Hz cutoff, since the numerical solution is valid only up to approximately this frequency) obtained along the fault centerline for 1.5 km x 8 km and 4 km x 16 km fault simulations, respectively. In both cases, the peak slip velocity apparently approaches a uniform level with increasing hypocentral distance.

Day (1979) interpreted these results for peak slip velocity with the aid of the closed-form analytical solution of Kostrov (1964) for an expanding circular crack, which is plotted as a solid curve on Figure 4.4. He concluded the following for the fixed-rupture-velocity model:

1. Peak slip velocity increases with distance from the focus up to a distance of about one fault width. In that region, the peak low-pass filtered slip velocity $\bar{s}$ is well approximated by

$$\bar{s} = C \frac{\Delta\sigma}{\rho\beta} (2rf/V_R + 1)^{1/2} \qquad (4.3)$$

   where f is the cutoff frequency, r is the distance from the center of the crack to the observation point, and C is a constant (derived from Kostrov's solution) which equals approximately $0.9\ V_R/\beta$ for a Poisson's ratio of 0.25 (Dahlen, 1974).

2. Peak slip velocity then remains nearly uniform over the remainder of the fault plane.

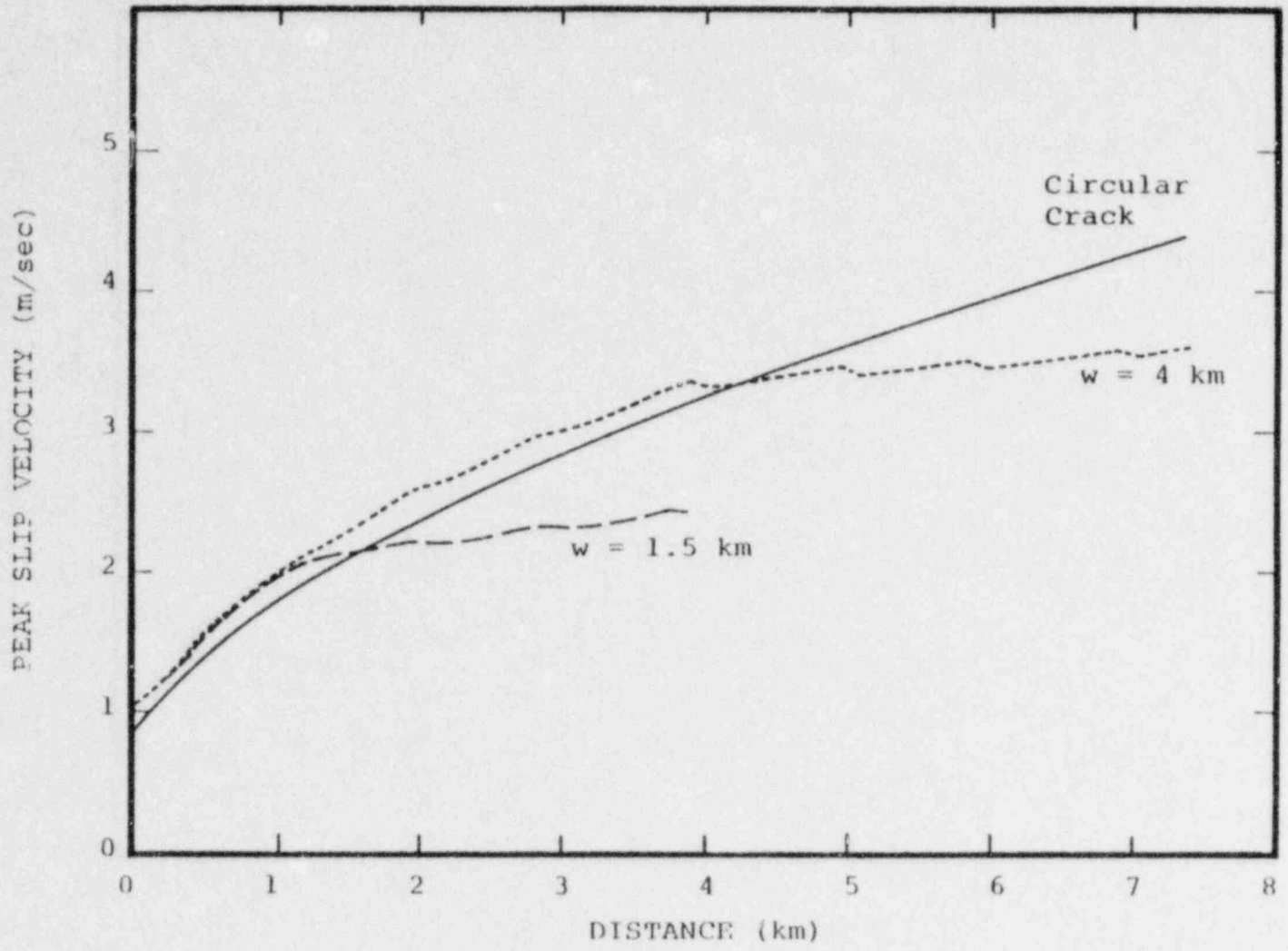

Figure 4.4. Peak slip velocity as a function of focal distance, along the center of the long dimension of the fault. The large-dashed curve is for the 1.5 km x 8 km case, the small-dashed curved is for the 4 km x 16 km case. The solid curve represents the analytic solution for an expanding circular crack. Peak velocities were determined from low-pass filtered slip histories with a 5 Hz cutoff.

3. Over most of its length, a long, narrow fault will experience a peak slip velocity (after low-pass filtering with cutoff frequency f) of approximately

$$\dot{\bar{s}} = \sqrt{\frac{2fw}{\beta}} \frac{\Delta\sigma}{\mu} \tag{4.4}$$

4.2.3 Analytic Approximation to the Slip Function

Now we are ready to derive a closed-form expression to approximate the slip function obtained from the dynamic model. The rise times τ_R plotted in Figure 4.3 can be approximated by the expression

$$\tau_R = t_s - \frac{1}{V_R}\sqrt{y^2 + x^2}$$

where

$$t_s = \min \begin{cases} \frac{1}{V_R}\sqrt{x^2 + \frac{w^2}{2}} + \frac{1}{\beta}\left(\frac{w}{2} - |y|\right) \\ \frac{1}{V_R}\sqrt{\frac{\ell^2}{2} + y^2} + \frac{1}{\beta}\left(\frac{\ell}{2} - |x|\right) \end{cases}$$

Referring to Figure 4.5, t_s is a rupture arrest time given by the smaller of (1) the sum of the rupture travel time over path A plus the shear wave travel time over path A', or (2) the sum of the rupture travel time over path B plus the shear wave travel time over path B'. The criteria for peak slip velocity set out in points 1 to 3 above are met by the expression

$$C \frac{\Delta\sigma}{\rho\beta} \sqrt{\tau_L \tau + 2 \min (r,w)/V_R]} \quad ,$$

where τ is the retarded time $t - r/V_R$. Finally, this expression, evaluated at τ_R, approximates very well the static slip values shown in Figure 4.2. Thus, our completed approximate expression for the slip function, s_d, is

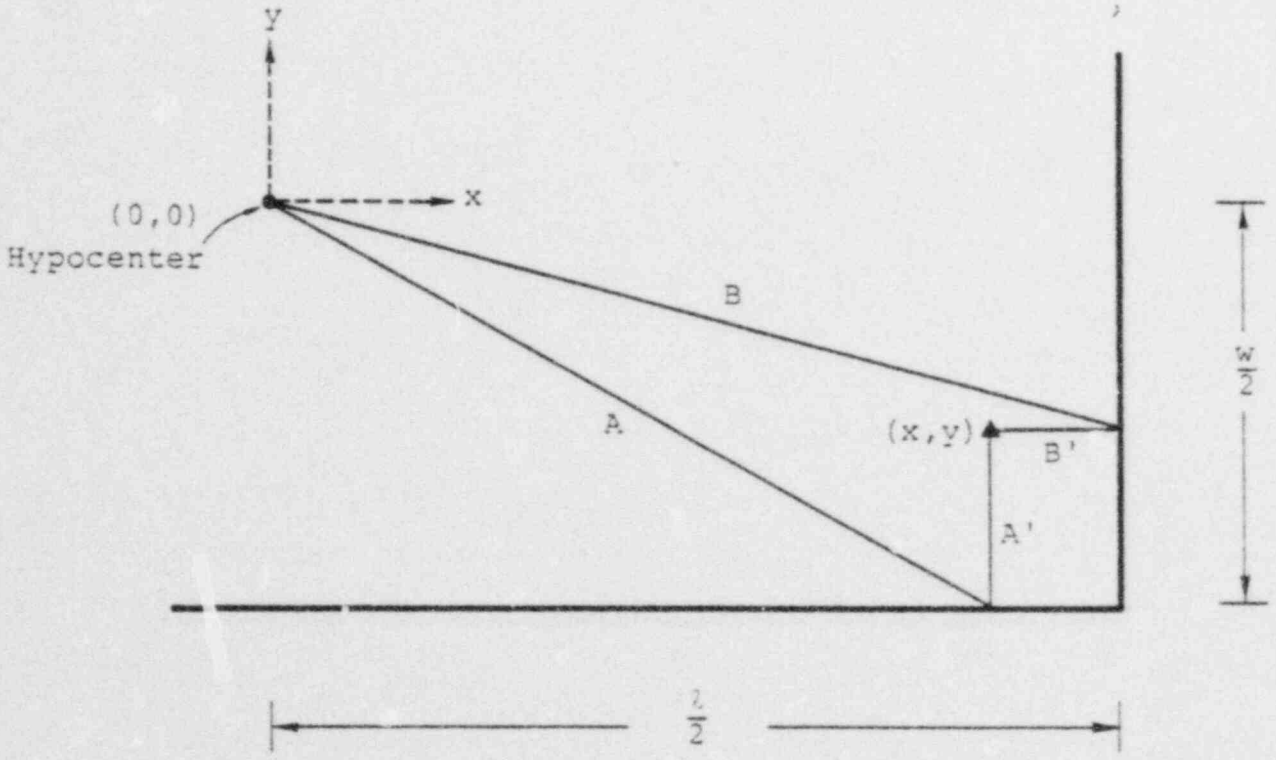

Figure 4.5. Geometry for estimating stopping phase arrival time.

$$s_d(\tau) = \begin{cases} C \frac{\Delta\sigma}{\rho\beta} \sqrt{\tau [\tau + 2 \min (r,w)/V_R]} & 0 < \tau < \tau_R \\ C \frac{\Delta\sigma}{\rho\beta} \sqrt{\tau_R [\tau_R + 2 \min (r,w,)/V_R]} & \tau > \tau_R \end{cases} \quad (4.5)$$

For points on the fault which are more than one fault width removed from the hypocenter, and for retarded time τ less than the rise time, s_d is spatially uniform. In the subsequent section we compare s_d, which we will call the "dynamic" slip function, with some slip functions which have previously been employed in kinematic earthquake modeling.

4.3 COMPARISON TO KINEMATIC MODELS

4.3.1 Introduction

Dynamic earthquake modeling provides a tool to assist in interpreting existing kinematic earthquake models in terms of physical parameters. In this section, we compare the dynamic slip function of Section 4.2 with (1) the TERA/DELTA three-parameter slip function and (2) the two-parameter ramp slip function. The objective of the comparison is to determine the relationship of the kinematic slip-function parameters to the dynamic model parameter $\Delta\sigma$.

4.3.2 The TERA/DELTA Slip Function

In the kinematic modeling studies of TERA/DELTA (Del Mar Tecnical Associates, 1979), a three-parameter slip function, which we will call s_{TD}, has been used to approximate earthquake dynamics. This slip function incorporates the parameters s_∞, τ_R, and v_0, which are, respectively, the final slip, the rise time, and the peak slip velocity. It is given by the expression

$$s_{TD}(\tau) = \begin{cases} A\tau^\alpha & 0 < \tau < \tau_R \\ A\tau_R^\alpha & \tau > \tau_R \end{cases}$$

where, for time step Δt, the constants α and A are

$$\alpha = \frac{\ln\left[\frac{s_\infty}{\Delta t \; v_0}\right]}{\ln\left[\frac{\tau_R}{\Delta t}\right]}$$

$$A = \Delta t^{1-\alpha} v_0$$

The following procedures have consistently been followed in the TERA/DELTA modeling:

1. The slip function is assumed to be spatially uniform.

2. The peak slip velocity v_0 has been assumed to be independent of τ_R and s_∞, and is fixed at 8 m/sec.

3. The time step Δt has been taken as 0.025, so that the Nyquist frequency is 20 Hz.

In its general charcteristics, the slip function s_{TD} resembles the dynamic slip function derived in Section 4.2.3 and given in Equation 4.5. In both cases, the slope is singular at $\tau = 0$ and monotonically decreases until $\tau = \tau_R$. We know from Section 4.2.2 that the assumption of spatial uniformity of slip is, in general, inconsistent with the results of dynamic modeling. However, for points on the fault more than one fault width away from the hypocenter, and for time short compared with the rise time, s_d is spatially uniform. It is reasonable, then, to compare the TERA/DELTA slip function with Equation 4.5, for hypocentral distance greater than w and for the initial few tenths of a second. It is this onset which controls the ground motion prediction in the high-frequency range which is of primary importance for the design of nuclear power plants.

In Figure 4.6, the TERA/DELTA slip function is shown for 2 sets of model parameters, the set employed to model design motion for the San Onofre Nuclear Generating Station, and the set used to model the 1966 Parkfield earthquake. These are summarized in Table 4.1. The dynamic slip function is shown in Figure 4.6 for V_R = 3.1 km/sec, β = 3.46 km/sec, w = 9 km and for hypocentral distance

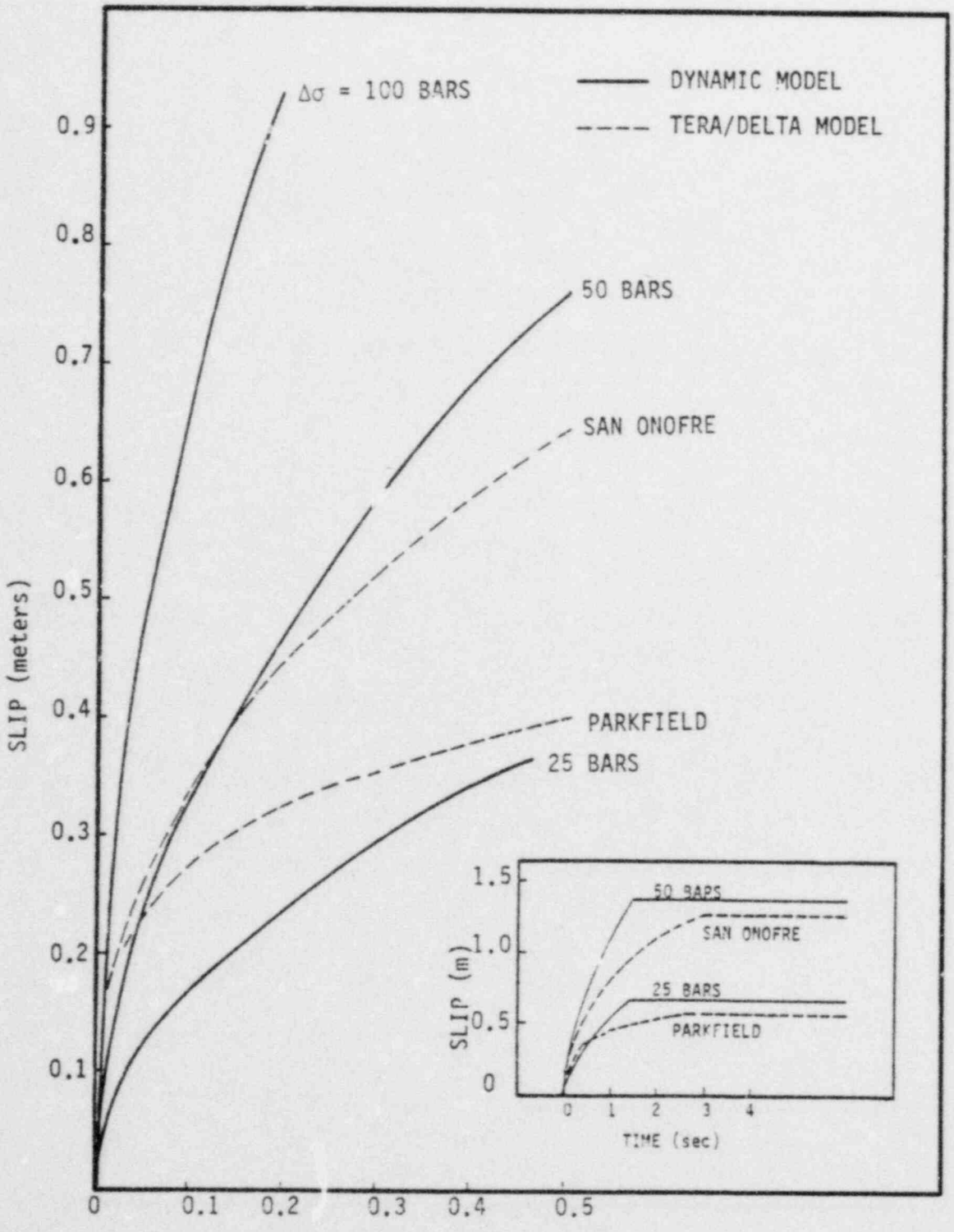

Figure 4.6. Comparison of dynamic slip function for three values of $\Delta\sigma$, with the TERA/DELTA slip functions for the San Onofre and Parkfield simulations. The dynamic slip function is for a point on the fault centerline, at a focal distance greater than the fault width w.

TABLE 4.1

PARAMETERS IN SLIP FUNCTIONS EMPLOYED IN FIGURES 4.5 TO 4.9

Dynamic	TERA/DELTA San Onofre	TERA/DELTA Parkfield
$W = 9$ km	$S_\infty = 1.3$ m	$S_\infty = 0.6$ m
$V_R = 3.1$ km/sec	$\tau_R = 2.9$ sec	$\tau_R = 2.7$ sec
$\beta = 3.46$ km/sec	$V_o = 8$ m/sec	$V_o = 8$ m/sec
$\rho = 2.7$ gm/cm^3		

greater than w. It is evident that s_d and s_{TD} are substantially different in detailed shape, so that we cannot use the comparison to uniquely identify the value of stress drop implicit in the TERA/DELTA slip function. At early time, s_{TD} follows the high-stress drop curves, and as time progresses, it crosses over to lower stress-drop, reflecting the fact that the dynamic slip function initially behaves at $\tau^{1/2}$, whereas the TERA/DELTA slip functions have exponents α less than 1/2.

To make this comparison more meaningful, we consider the response spectra of the slip velocity functions, since it has been argued (Del Mar Technical Associates) that high-frequency ground acceleration varies with frequency in a manner similar to that of slip velocity. As shown in Appendix B, the (undamped) pseudo-velocity response spectrum V_d of the dynamic slip function, for oscillator period T_0 less than approximately twice the rise time, is

$$V_D(T_0) = \frac{0.95\ C\Delta\sigma}{2\rho\beta} \sqrt{\frac{2w}{V_R}}\ T_0^{1/2} \qquad (4.6)$$

and the response spectrum V_{TD} of the TERA/DELTA slip velocity, also for T_0 less than about 2 T_R, is

$$V_{TD}(T_0) = \alpha A\ (2\pi)^{-\alpha} \left[\frac{T_0}{\pi\Delta t}\ \sin(\pi\Delta t/T_0) \right] \left\| \theta_\alpha \right\|\ T_0^\alpha \qquad (4.7)$$

The term in brackets results from the discretization of s_{TD}, and approaches 1 for $T_0 >> \Delta t$ and $2/\pi$ for $T_0 = 2\Delta t$; $\left\| \theta_\alpha \right\|$ is a constant which depends on α.

Figure 4.7 compares the response spectrum for the TERA/DELTA San Onofre slip function with that of the dynamic slip function. This figure indicates that the TERA/DELTA model slip function, in the 0.05 to 0.5 second period range, behaves approximately as does the slip function of a dynamic model with a stress-drop of about 50 bars. The discretization effect in Equation 4.7 is in considerable

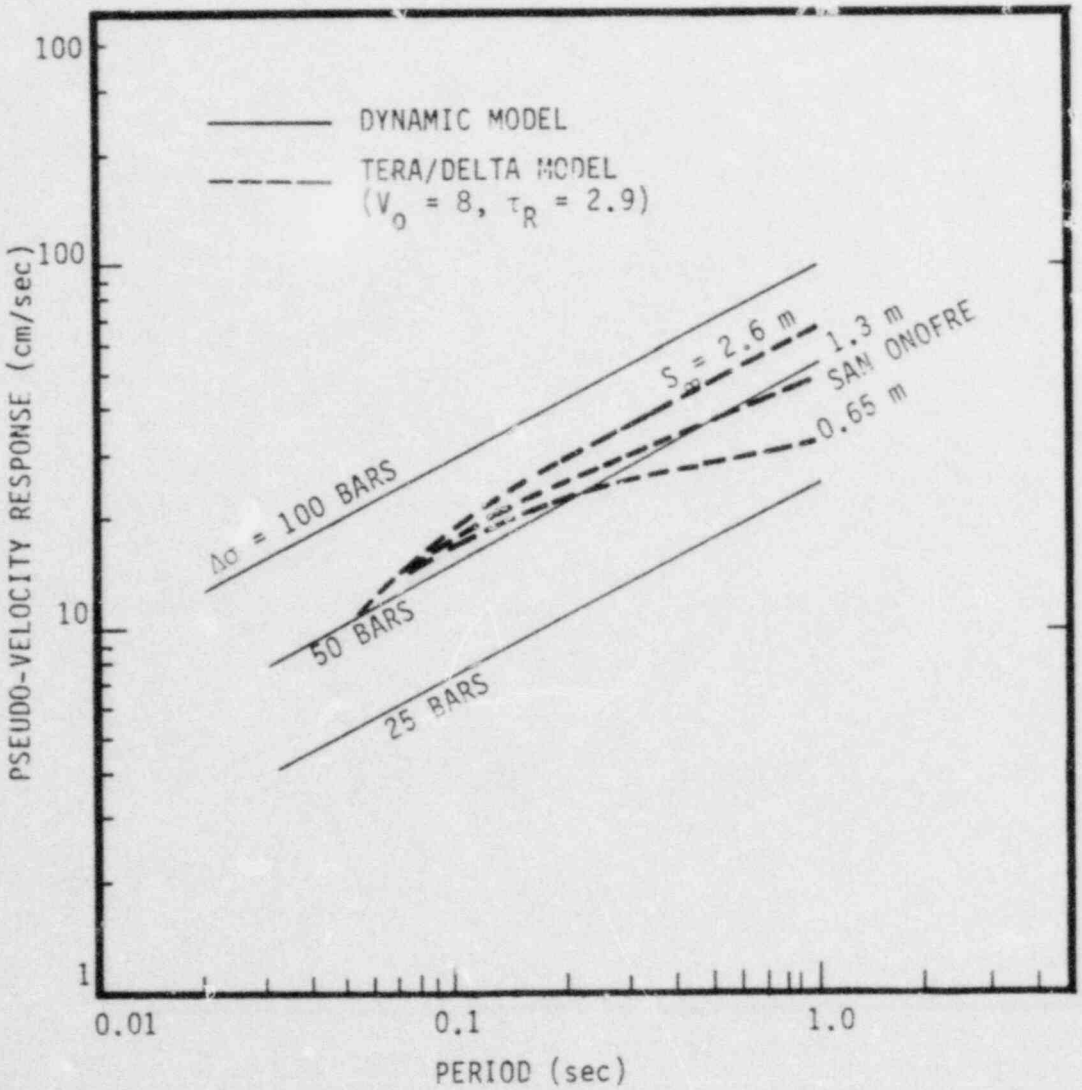

Figure 4.7. Comparison of response spectrum of the dynamic slip function with that of the TERA/DELTA San Onofre slip function.

measure responsible for the fact that the TERA/DELTA spectral shape conforms moderately well to that of the dynamic model in this period range. This is also shown, in terms of Fourier spectra, in Figure 4.8.

As far as energy at 0.05 to 0.5 second periods is concerned, then, the TERA/DELTA slip function for San Onofre is a reasonable representation of the dynamic slip function scaled to $\Delta\sigma$ = 50 bars. As Figure 4.7 indicates, the sensitivity to s_∞ is minimal in this range for the TERA/DELTA slip function. In fact, it has been shown (Del Mar Technical Associates, 1979), that the TERA/DELTA slip function spectral level in this period range is essentially proportional to v_0; this is also demonstrated by Figure 4.9. On the other hand, the spectral level of the dynamic slip function in this range scales directly with $\Delta\sigma$. Thus, the TERA/DELTA modeling assumption (2) above, that v_0 is invariably equal to 8 m/sec, is approximately the same as assuming that $\Delta\sigma$ is invariant and equals about 50 bars.

4.3.3 The Ramp Slip Function

A large number of kinematic earthquake simulation studies (for example, Aki, 1968; Kawasaki, 1975; Bouchon, 1979) have employed a slip time function s_R with the form of a ramp with constant slip velocity v_0 and duration τ_R:

$$S_R = \begin{cases} v_0 & 0 < \tau < \tau_R \\ v_0 \ \tau_R & \tau > \tau_R \end{cases}$$

The response spectrum of this function, for oscillator periods shorter than twice the rise time, is

$$V_R(T_0) = \frac{V_0}{\pi} \ T \qquad (4.8)$$

Figure 4.10 compares this response spectrum with that of s_d. The ramp slip function differs substantially in spectral shape from the

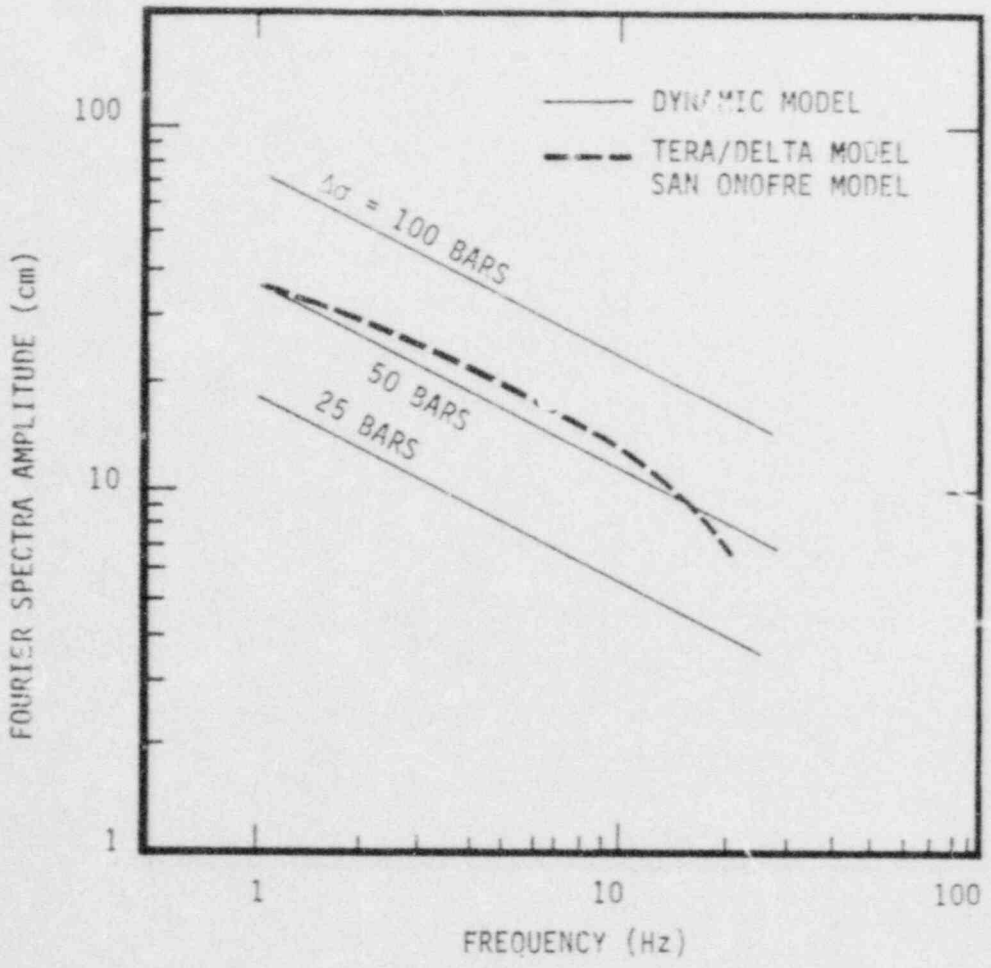

Figure 4.8. Fourier spectrum of the dynamic slip function, compared with that of the TERA/DELTA San Onofre slip function.

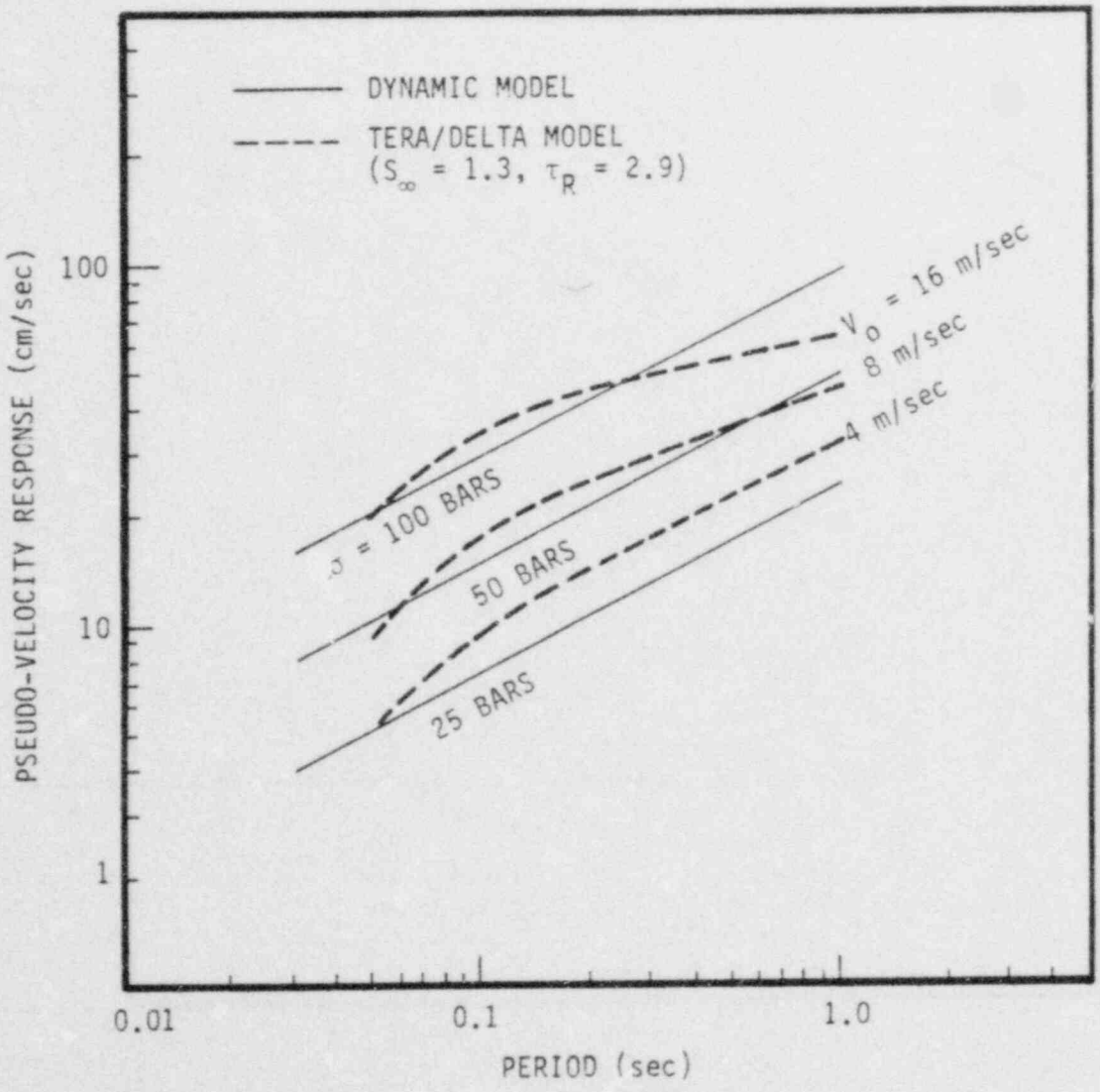

Figure 4,9. Response spectrum of the dynamic slip function, compared with that of the TERA/DELTA slip function.

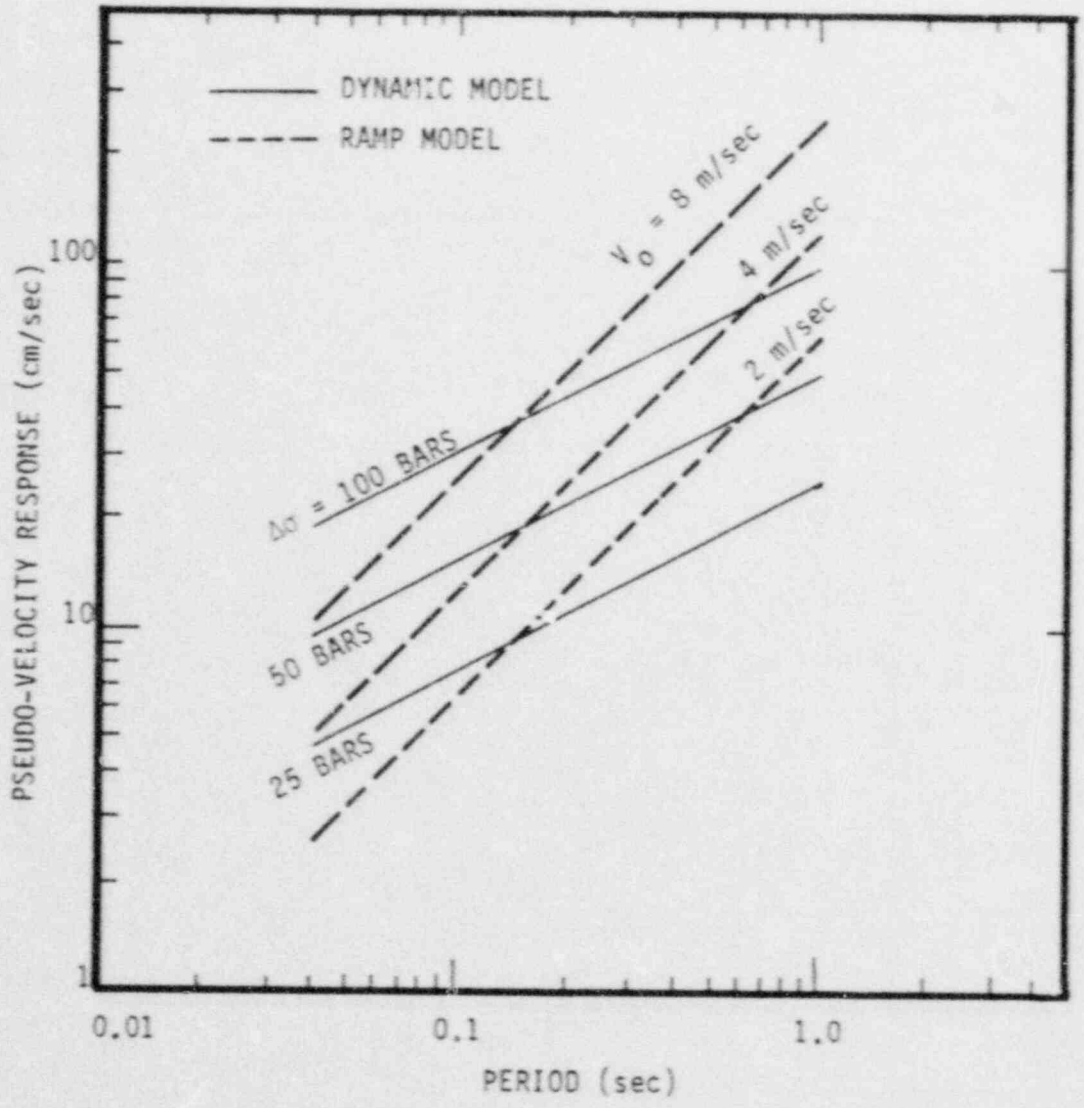

Figure 4.10. Comparison of response spectrum of the dynamic slip function with that of the ramp slip function.

dynamic slip function over the period range of engineering importance. Its deficienty in short period energy relative to the dynamic model probably renders the ramp time function unsuitable for design motion simulation, except perhaps over a narrow frequency band.

Del Mar Technical Associates (1979) attempted to model the Parkfield earthquake using the ramp slip function. They reported difficulty in matching observed response spectra over a broad period range with this slip function. In order to fit observed short-period spectral levels of ground motion, with reasonable rise times, it was necessary to tolerate a large overestimate at long periods. The above comparison with the dynamic model provides a physical basis for this result.

4.4 ASSESSMENT OF MODELING ASSUMPTIONS

In this section, we attempt to assess the importance of the main modeling assumptions. The sensitivity of computed ground motion to assumed rupture velocity is first considered. Then we evaluate the importance of the assumption of abrupt stopping of rupture growth.

To assess the behavior of the fixed-rupture-velocity dynamic model, we apply Equation 4.5 to compute ground acceleration near a buried strike-slip fault. Figure 4.11 shows the fault geometry and receiver location. The fault is 15 km long, 5 km wide, buried between the depths of 2.5 and 7.5 km. The receiver is located at the surface, in the plane of the fault, so that the only non-zero component of motion is in a direction normal to the fault plane, and is predominantly shear waves. A two-dimensional numerical integration over the fault surface was performed, using the integral solution of Haskell (1969) with the slip function of Equation 4.5. The integration mesh was sufficient to retain accuracy for frequencies up to 10 Hz. The calculation was for a uniform wholespace (with the free surface effect approximated by doubling the computed motion). The computed acceleration was scaled to represent a stress-drop of 25 bars.

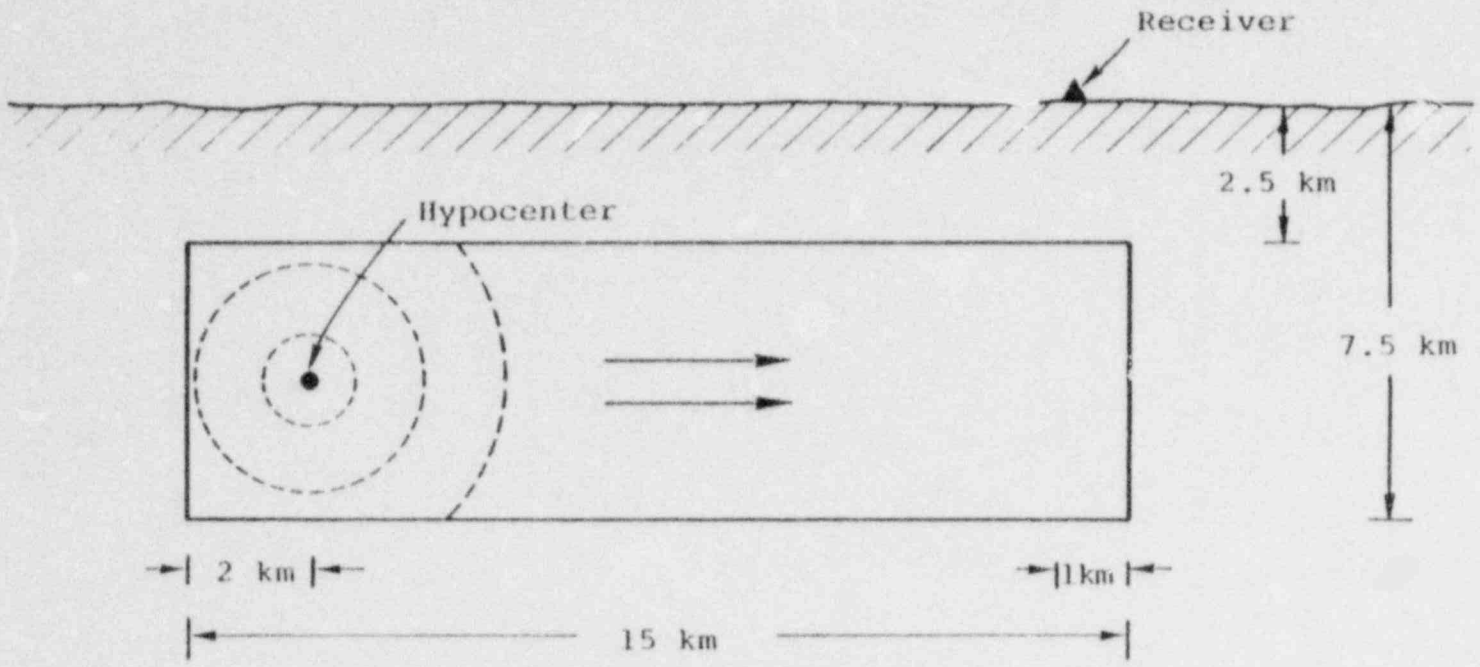

Figure 4.11. Problem geometry for accelerogram synthesis. The observer lies in the plane of the fault.

First we consider the sensitivity of ground motion predictions to the assumed rupture velocity. This is a model input which is only rougnly constrained by observational evidence. Figure 4.12 shows the computed accelerations for three choices of rupture velocity, all well within tne range of plausibility. Peak acceleration increases with rupture velocity, ranging from 0.24 g to 0.90 g. Without some independent constraint on rupture velocity, then, there is substantial uncertainty in the model's ground motion prediction.

The main acceleration peak in each accelerogram in Figure 4.12 can be clearly identified with the first-arriving stopping phase radiated when the rupture front impinged on the upper edge of the fault surface. The two peaks near the end of each record are first-arriving stopping phases from the right edge and bottom edge, respectively. The predominant acceleration signal, then, is controlled by the admittedly artificial assumptions of uniform rupture velocity and abrupt stopping.

Further support for this assessment is provided by Figures 4.13 and 4.14. These show far-field waveforms, computed at 2 particular azimuths, for a simulation of a 4 x 8 fault. Again, sharp, discrete stopping phases from each edge of the fault are the dominant features of the acceleration records, and the remainder of the acceleration record is relatively quiet. This simple character is in poor qualitative accord with observed earthquake accelerograms. Complexity in observed accelerograms results from some combination of complexity in the response of the earth model and complexity in the source model; since these near- and far-field calculations employed a highly simplified earth model, they do not offer conclusive evidence tnat the source model is inconsistent with data.

4.5 CONCLUSIONS

In this chapter we have reviewed results of fixed-rupture-velocity dynamic earthquake modeling. The first objective was to characterize the slip function resulting from his model. In this connection, the following conclusions are obtained:

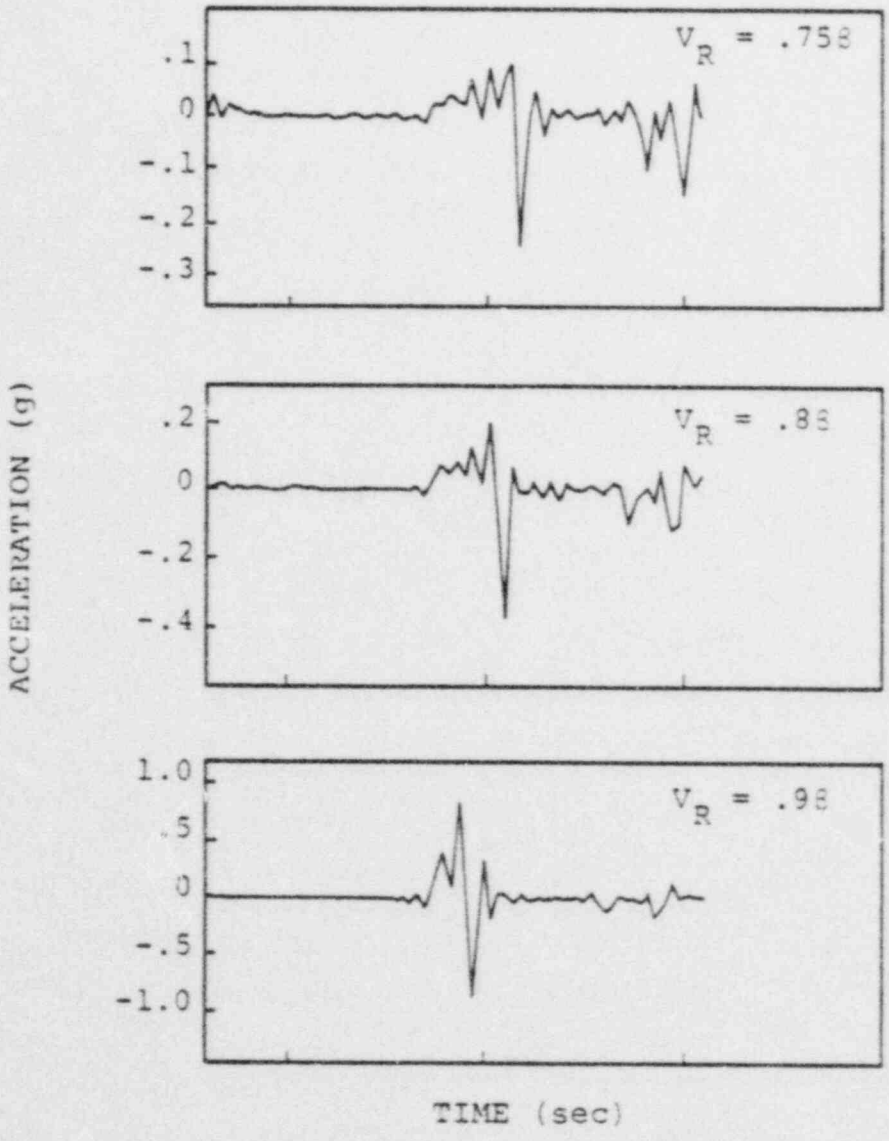

Figure 4.12. Synthetic accelerograms computed with equation, for three different rupture velocities V_R.

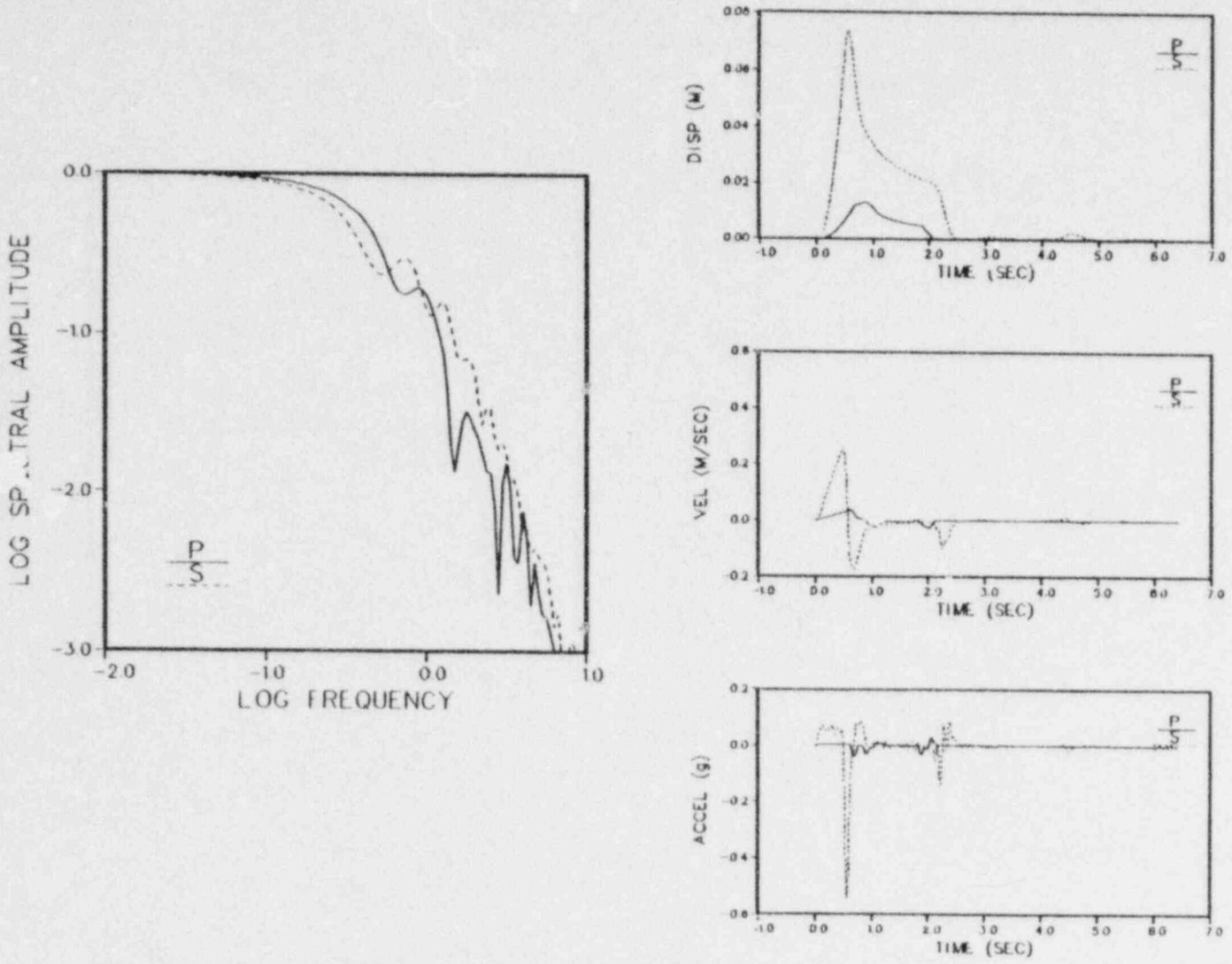

Figure 4.13. Far-field displacement, velocity and acceleration pulses and displacement spectra obtained for a 4 km x 8 km fault. Observer is at spherical coordinates $\theta = 45$, $\phi = 0$, relative to fault normal, amplitudes are normalized to a stress drop of 100 bars and a hypocentral distance of 10 km, and the double-couple radiation pattern has been factored out.

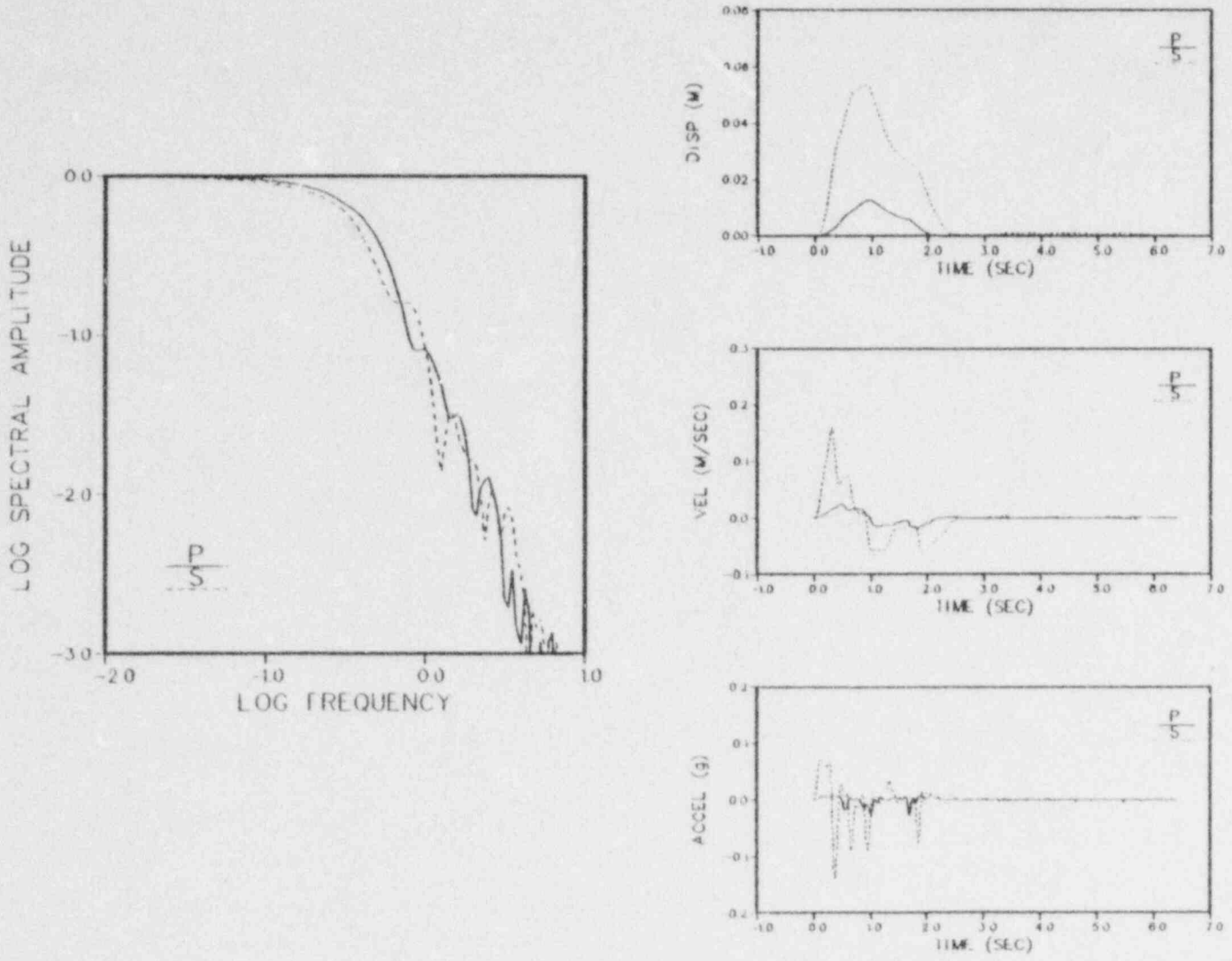

Figure 4.14. Far-field displacement, velocity and acceleration pulses and displacement spectra obtained for a 4 km x 8 km fault. Observer is at spherical coordinates $\theta = 45$, $\phi = 45$, relative to fault normal, amplitudes are normalized to a stress drop of 100 bars and a hypocentral distance of 10 km, and the double-couple radiation pattern has been factored out.

1. High-frequency content of the slip function increases with the stress-drop $\Delta\sigma$, which in turn is bounded below by the static stress drop.

2. The slip function resulting from the dynamic model varies spatially over the fault surface. For points on the fault more than one fault width away from the hypocenter, however, and for time short compared to the slip rise time, the slip function is spatially quite uniform.

3. Static slip, along the fault centerline, is about the same as given by Knopoff's two-dimensional static solution:

$$s(\infty) = \frac{\Delta\sigma}{\rho\beta^2} w$$

4. The slip rise time τ_R, along the fault centerline at distance greater than w, is approximately

$$\tau_R = \frac{w}{2\beta} .$$

5. The onset of slip has the form of a square root singularity, and the peak, low-pass filtered slip velocity s, for points more than a fault width from the hypocenter, is well approximated by

$$\bar{s} = \sqrt{\frac{2wf}{\beta}} \frac{\Delta\sigma}{\rho\beta} ,$$

where w is the fault width, β the shear speed, ρ the density, $\Delta\sigma$ the stress-drop, and f the cutoff frequency.

6. A relatively simple analytic expression, Equation 4.5, approximates the spatial and temporal behavior of the slip function reasonably well.

A second objective was to use results from dynamic modeling to interpret kinematic earthquake models in terms of physical parameters. It is found that

1. The TERA/DELTA 3-parameter slip function (San Onofre model) is representative, in its spectral

content in the 0.05 to 0.5 second period range, of the slip function from the dynamic model scaled to a stress-drop of about 50 bars.

2. The ramp slip function is deficient in short-period energy relative to the dynamic slip function.

The third objective was to assess the sensitivity of simulated ground motion to the main modeling assumptions. The conclusions are:

1. Predictions of peak acceleration are highly sensitive to the specification of rupture velocity, which is a poorly constrained model input.

2. The predominant acceleration pulses predicted by the model are controlled by the model assumptions of uniform rupture growth and abrupt stopping of rupture.

V. DYNAMIC EARTHQUAKE MODELS WITH SPONTANEOUS RUPTURE

5.1 INTRODUCTION

The dynamic earthquake model considered in Section IV assumes that rupture velocity and stress-drop are uniform over the fault plane, and stopping of rupture occurs abruptly at the fault edges. Large stress concentrations were permitted to develop at the rupture front. We have seen that these assumptions lead to a slip function which is well approximated by a square root singularity, for frequencies of engineering interest. The peak (low-pass filtered) slip velocity is proportional to the stress drop ("effective stress") and to the square root of the fault width. A small number of discrete stopping phases are responsible for the main acceleration pulses radiated by the model, and this is true in both the near-field and the far-field.

In this chapter we examine the consequences of relaxing these constraints. We will look at slip functions and acceleration pulses from dynamic earthquake simulations with spontaneous rupture. In such simulations, rather than specifying a rupture velocity, one specifies a failure criterion and permits rupture to ensue spontaneously. For the numerical simulations (Day, 1979) that form the basis for this chapter, the failure criterion is such that shear stress in the fault plane is limited to a prescribed strength, σ_0. In Section 5.2, we briefly overview the rupture model used in those simulations.

In Section 5.3, we consider the slip functions from spontaneous-rupture simulations. It is inferred from these simulations that the main conclusions regarding the scaling of the slip function for the fixed-rupture-velocity model are still valid for the spontaneous rupture case. This conclusion may require modificaton when more advanced constitutive models for the fault zone are available; simulations incorporating higher values for the cohesive stress (excess of strength above the prestress) might also result in a modification of this conclusion.

In Section 5.4 we compare acceleration pulses predicted from spontaneous-rupture simulations with those predicted from the fixed-rupture-velocity model. It is found that when fault growth accelerates, decelera.es, and stops spontaneously in response to stress inhomogeneity, the acceleration time histories are more complex than in the fixed-rupture-velocity case, and no longer dominated by a few discrete stopping phases.

Section 5.5 summarizes the conclusions from spontaneous-rupture dynamic modeling.

5.2 FAULT CONSTITUTIVE MODEL

Very little work has been done to date on the three-dimensional simulation of spontaneous rupture. Our analysis is based on the simulations performed by Day (1979) using a three-dimensional finite difference method. Here, we briefly overview the slip-weakening fault-plane constitutive model used in that study.

In the slip-weakening model, shear traction on the fault plane, which is initially σ_T, is limited by a frictional strength σ_0. When the shear traction reaches σ_0, further stress buildup is relieved by fault slip. The slip velocity at a point is opposed by a frictional traction which is a prescribed, decreasing function of the total slip which has occurred at the point. When the total slip reaches a constant, d_0, cohesion is considered destroyed, and the frictional traction is held at a fixed "sliding friction" level σ_f.

The quantity $\sigma_T - \sigma_f$ we will continue to call the stress-drop ($\Delta\sigma$), as in Chapter 4, although it has often been called "effective stress." The quantity $\sigma_0 - \sigma_T$, the "cohesive stress," represents the amount by which the shear traction at a point must be elevated, due to slip elsewhere on the fault, before rupture ensues. The quantity $\sigma_0 - \sigma_f$ we will call "dynamic stress drop," since this is the sense in which that term is used by a number of authors (for example, Cherry et al., 1976; Del Mar

Technical Associates, 1978). The dynamic stress drop is, then, the difference between peak shear traction and sliding frictional traction on the fault plane. It has been suggested by some investigators (for example, Ida, 1973; Brune, 1976) that the dynamic stress drop should control the high-frequency behavior of the slip function; this contrasts with the fixed-rupture-velocity model, in which the high frequencies scale with $\Delta\sigma$. This hypothesis about the role of dynamic stress drop is important, because, unlike $\Delta\sigma$, dynamic stress drop is independent of the tectonic stress, and may ultimately be predictable from rock properties.

At the present, estimates of the appropriate distribution of cohesive stress for large earthquakes are somewhat speculative. The three-dimensional simulations considered in this chapter were performed assuming relatively low average values of cohesion.

5.3 SLIP FUNCTION FOR SPONTANEOUS RUPTURE

5.3.1 Uniform Prestress

Figure 5.1 shows rupture front contours at 0.3 second intervals for a spontaneous rupture simulation. In this particular simulation, both the stress drop and the cohesive stress are uniform, and rupture has been artificially restricted to a rectangular region 4 km by 16 km in dimension. For this simulation, the material parameters α, β and ρ and 6.0 km/sec, 3.46 km/sec, and 2.7 gm/cm^3, respectively, and d_o = 0.08 m, $\Delta\sigma$ = 100 bars, and the dynamic stress drop is 1.5 $\Delta\sigma$. This represents fairly low cohesion, and the analyses of Das and Aki (1977) and Andrews (1976) would predict rupture velocities in excess of the shear speed. This is indeed the case, as seen from the contour spacing in the figure. The very high average rupture velocity, nearly 4 km/sec, suggests that, on the average, an unrealistically low value of cohesion has been used.

Low-passed (5 Hz) slip velocities along the x axis are shown in Figure 5.2. Over the 8 km distance range, the peak slip velocity has not yet settled at a nearly constant value, as occurred for the same fault geometry at fixed rupture velocity (Figure 4.4). This is

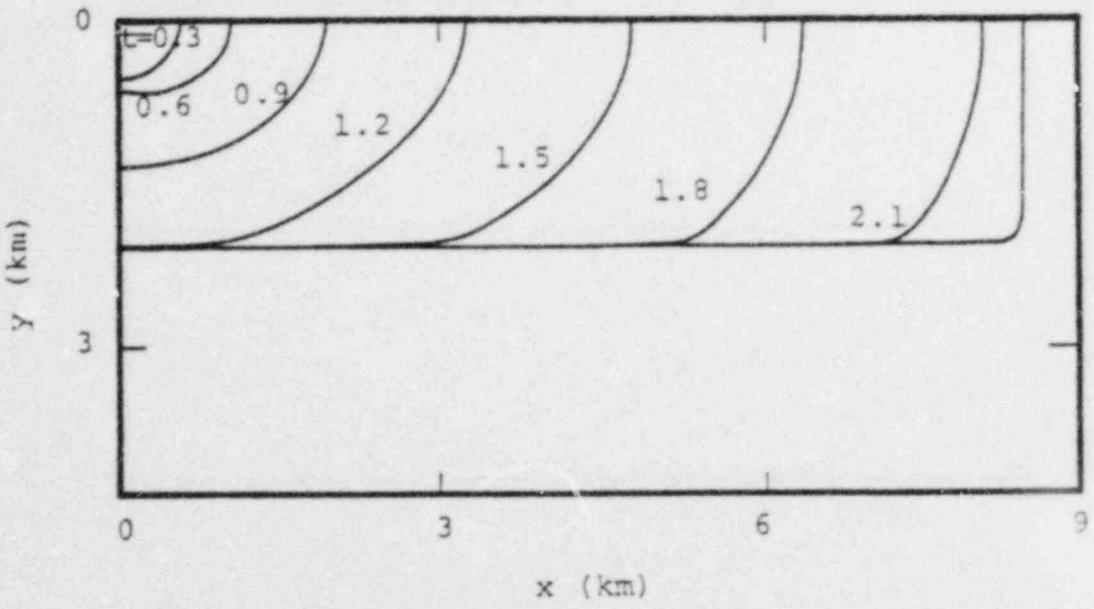

Figure 5.1. Rupture front contours at 0.3 second intervals, for spontaneous rupture simulation in the uniform stress-drop case.

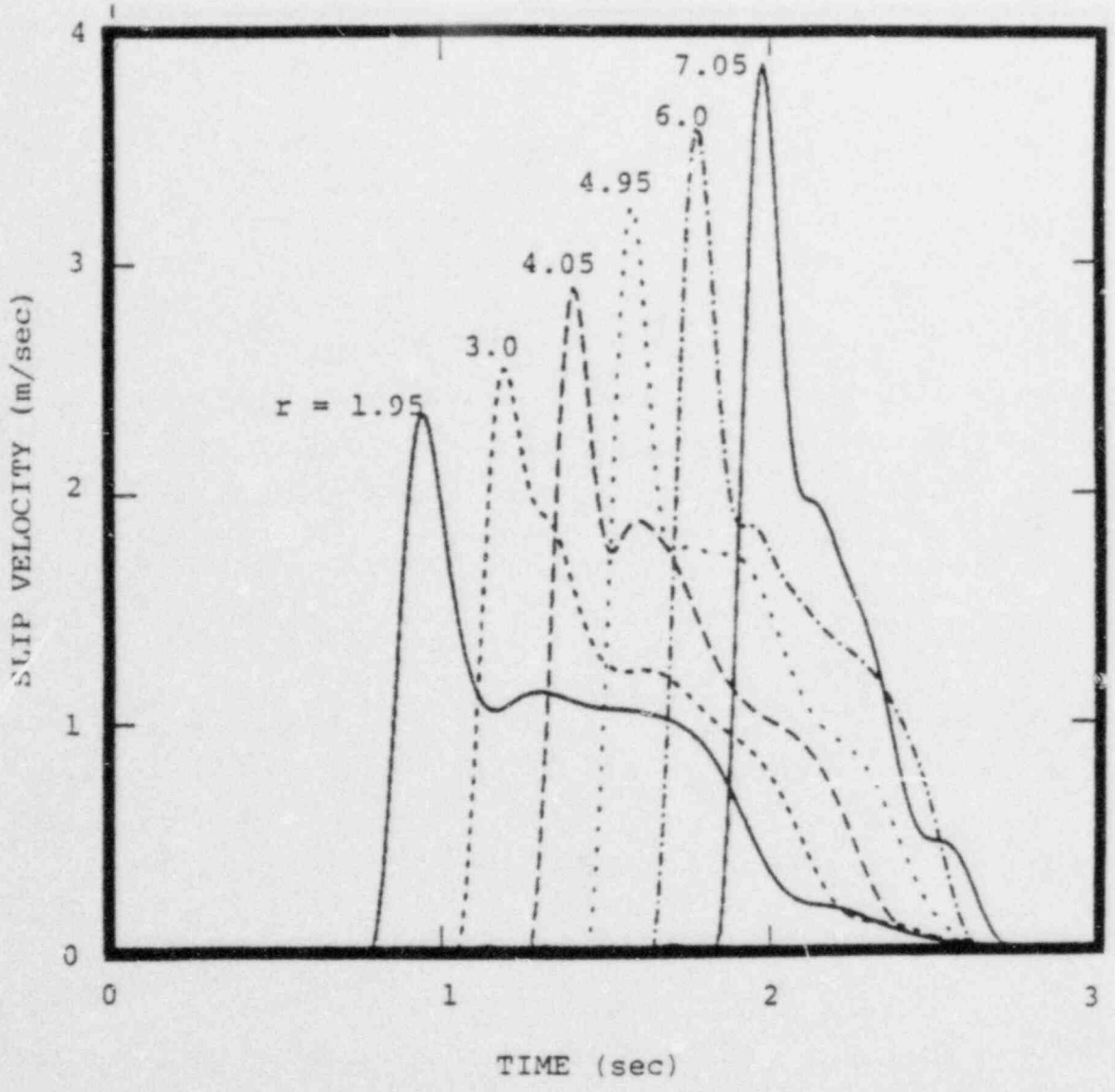

Figure 5.2. Slip velocities along the x axis, for spontaneous rupture with uniform stress drop. Time histories have been low-pass filtered with a 5 Hz cutoff.

apparently due to the fact that the rupture velocity is still accelerating, even at 8 km focal distance. Figure 5.3 demonstrates that the peak slip velocity is nearly uniform across the fault width, as for the fixed rupture velocity case. Recall that stress-drop is uniform, and rupture termination has been artificially enforced at the fault edges.

Peak values of slip velocity from Figures 5.2 and 5.3 are very close to the estimate of

$$\dot{\bar{s}} = \sqrt{\frac{2wf}{\beta}} \frac{\Delta\sigma}{\rho\beta} \tag{5.1}$$

deduced in Section 4.2.2 for the fixed-rupture-velocity case. At 6 km focal distance, for example, peak slip velocities from Figures 5.2 and 5.3 agree within a few percent with the value 3.6 m/sec given by Equation (5.1). This is appreciably larger than would be predicted from the hypothesis that high-frequency slip is controlled exclusively by dynamic stress drop. For example, Ida's (1973) formula for peak slip velocity in terms of dynamic stress drop is

$$\dot{\bar{s}} = \frac{\sigma_0 - \sigma_f}{\rho\beta^2} V_R \tag{5.2}$$

which gives a value about 70 percent of that shown in Figures 5.2 and 5.3 at a distance of 6 km (taking V_R in Equation (5.2) to be the "local" rupture velocity of about 5.5 km/sec). Furthermore, the peak slip velocities in Figures 5.2 and 5.3 are lower limits, by virtue of the 5 Hz frequency cutoff. Thus, the high-frequency components of the slip function for the spontaneous rupture model appear to scale with stress-drop, as predicted by Equations 4.5 and 5.1, rather than being independent of stress-drop, as predicted by Equation 5.2.

There is really no theoretical discrepancy here, since Ida's formula was derived on the assumption, among others, that dynamic stress-drop is much greater than $\Delta\sigma$. Equation (5.2) can then be viewed as an asymptotic limit on peak slip velocity, appropriate as dynamic stress drop becomes very large relative to $\Delta\sigma$.

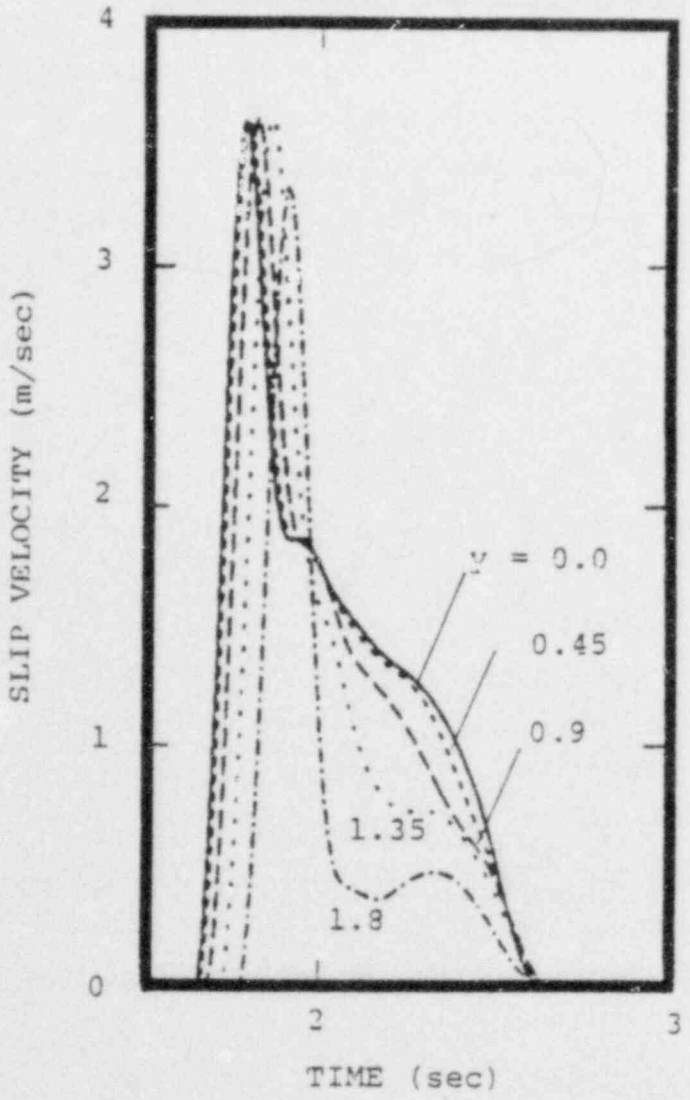

Figure 5.3. Slip velocities across the width of the fault at x = 6 km, for spontaneous rupture simulation with uniform stress drop. Time histories have been low-pass filtered with a 5 Hz cutoff.

The simulation under discussion was performed for a very low value of dynamic stress-drop, as discussed above. The asymptotic formula (5.2) predicts increasing peak slip velocity with increasing dynamic stress-drop, although the increase may be offset somewhat by a decrease in rupture velocity. Additional simulations, incorporating a range of cohesion values, would be useful to quantify the relationship between stress-drop, dynamic stress-drop, and high-frequency content of the slip function. Given our current understanding of this relationship, however, we have no theoretical basis in earthquake dynamics for reducing the high-frequency content of the slip function below that of Equation (4.5).

5.3.2 Non-Uniform Prestress

As a further step toward understanding the slip functions for spontaneous rupture, we consider the three non-uniform prestress configurations, denoted A, B and C, shown in Figure 5.4. In each case, rupture initiated at the origin. In cases A and B, rupture growth was permitted to stop spontaneously. In case C, rupture growth decelerated considerably as it progressed into the low stress-drop region, but still reached pre-specified strength barriers which delimited a 6 km x 18 km rectangular region.

For case A, the stress drop is 100 bars over a circular region 1.43 km in radius, and is equal to zero outside that region. The dynamic stress drop is uniform, 120 bars. Figure 5.5 shows contours of the rupture front at 0.3 second intervals. The rupture accelerates rapidly over the 100 bar stress-drop patch, then abruptly decelerates as it breaks into the zero-stress-drop region. In the y direction, deceleration is very abrupt, and the rupture penetrates only about 150 meters into the low-stress region. In the x direction, however, the rupture penetrates about 500 meters into the low-stress region. By 1.5 seconds, rupture growth has ceased.

Figure 5.6 shows both peak slip velocity (low-passed, 5 Hz) and rupture velocity along the x axis. We note that the two

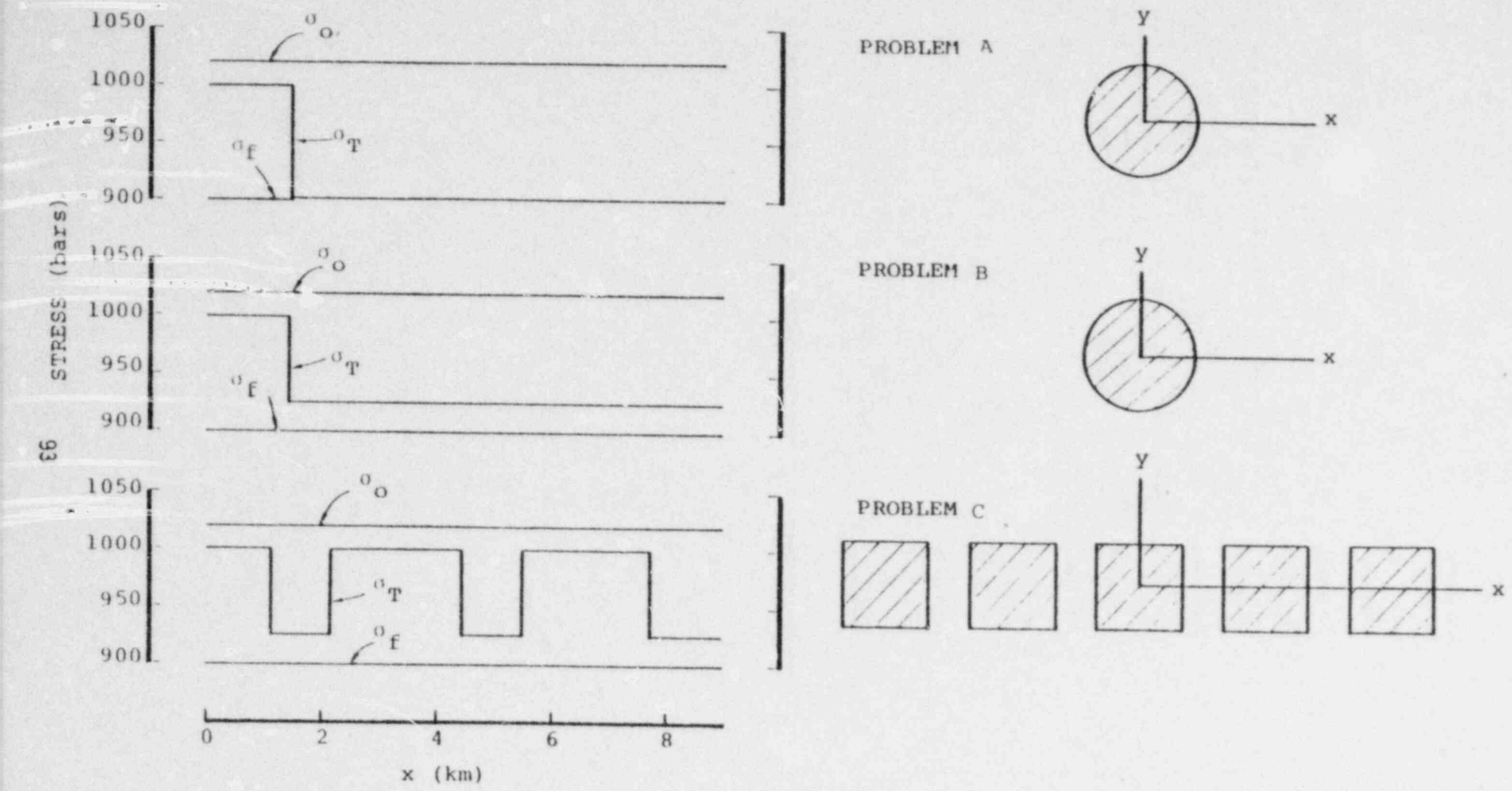

Figure 5.4. Nonuniform stress configurations A, B, and C.

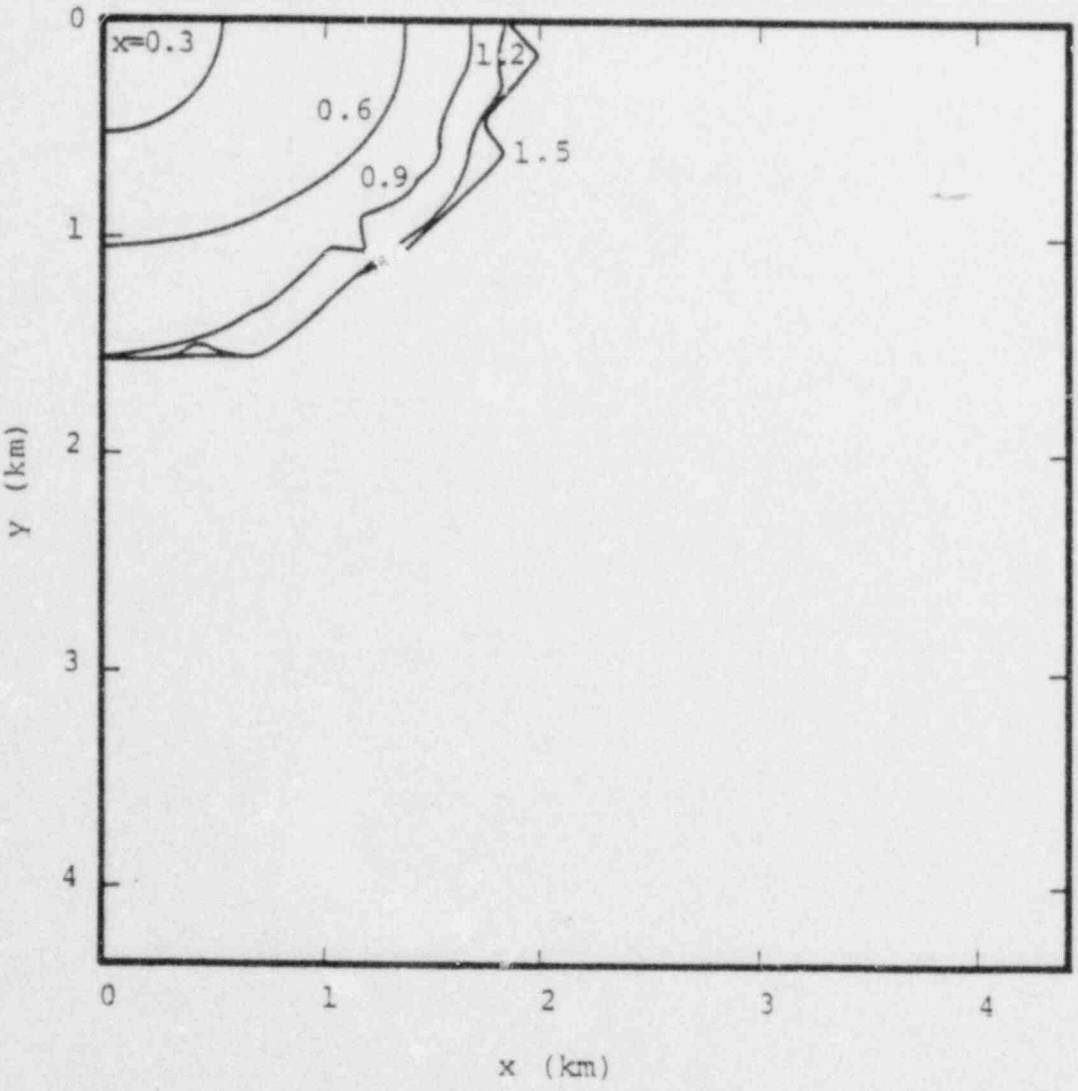

Figure 5.5. Rupture front contours for Case A, at 0.3 second intervals.

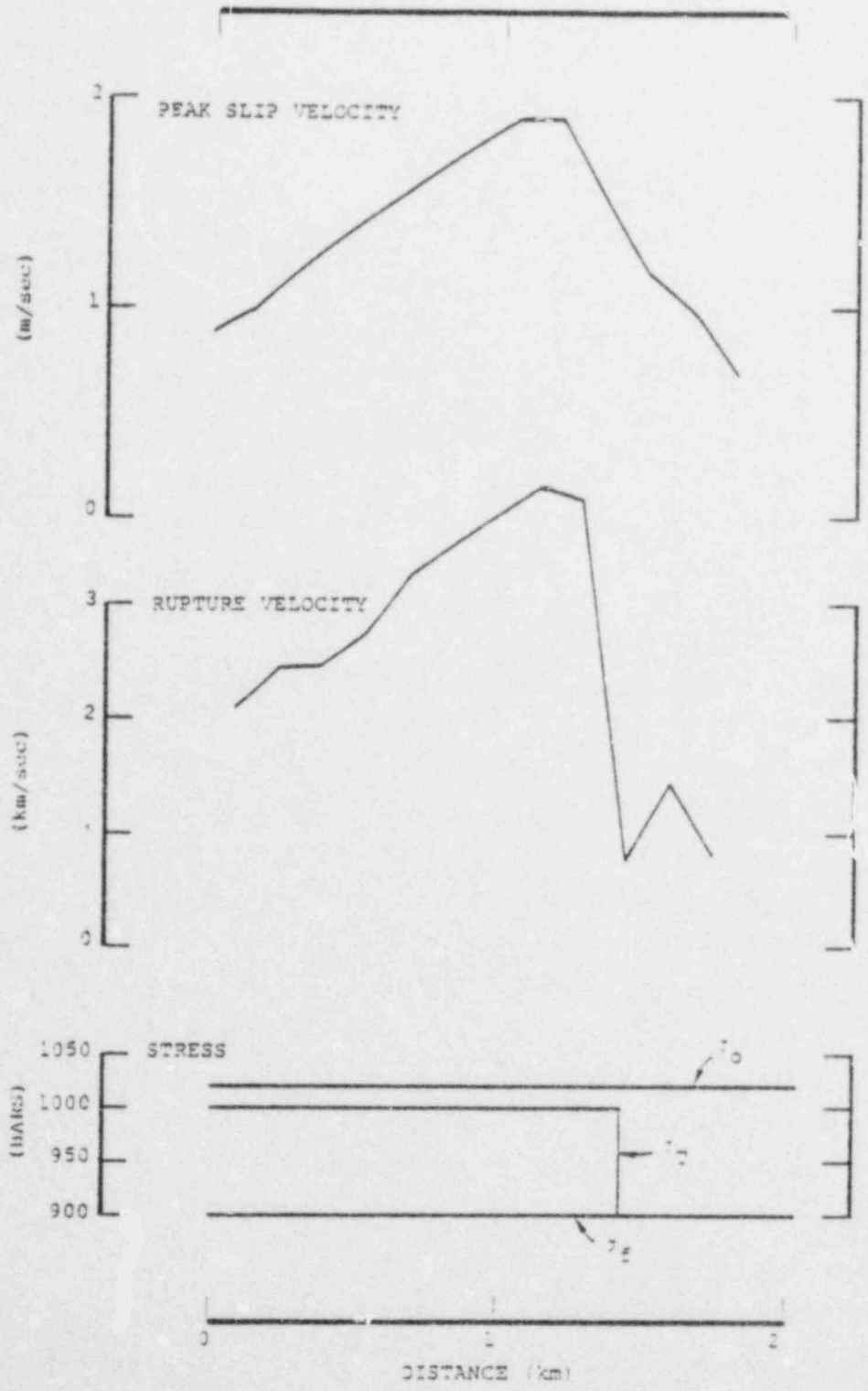

Figure 5.6. Peak slip velocity (low-passed, 5 Hz cutoff) and rupture velocity along the x axis, for Case A.

quantities roughly parallel each other. When the rupture decelerates, the peak slip velocity falls off. A maximum rupture velocity of 4 km/sec is reached at the edge of the prestressed zone.

Case B differs from case A only in having a stress-drop of 25 bars outside the circular 100 bar stress-drop patch. Dynamic stress drop is again uniformly 120 bars. In spite of this non-zero stress-drop, we see from Figure 5.7 that the rupture still stops spontaneously, this time at about 2.1 seconds. Rupture again decelerates outside the high-stress patch, but overshoots it by 0.6 km in the y direction and 1.5 km in the x direction.

Figure 5.8 again demonstrates the strong linkage between peak slip velocity and rupture velocity. Rupture velocity in the x direction peaks at about 4 km/sec, drops sharply at the edge of the circular patch, then recovers to about 1.7 km/sec and smoothly decelerates to zero. The slip velocity mirrors this behavior.

Case C contains several patches of 100 bar stress-drop, surrounded by a 25 bar stress-drop region, with dynamic stress-drop uniform at 120 bars (see Figure 5.4). Figure 5.9 shows the rupture front contours at 0.1 second intervals. A fairly complex pattern of rupture develops. Along the y axis, for example, rupture stops just after 1 second. As rupture advances on the other parts of the fault plane, however, the stress intensity along the y axis increases, and rupture recommences at about 1.8 seconds. Along the x axis, rupture accelerates rapidly as it breaks each high-stress patch, and decelerates between patches. At 1.1 seconds, and then again at 1.9 seconds, the rupture front "jumps," leaving unbroken areas behind, which subsequently break.

In case C, the average value of stress-drop over the 6 x 18 km fault is about 42 bars. On the average, the cohesive stress is considerably higher relative to the stress-drop than it was for the uniform stress-drop model studied in Section 5.3.1; on the average, the dynamic stress-drop is about 2.9 $\Delta\sigma$ for case C, compared to 1.5 $\Delta\sigma$ for the uniform stress-drop model. As a result, the average rupture velocity has been reduced from well above the shear wave

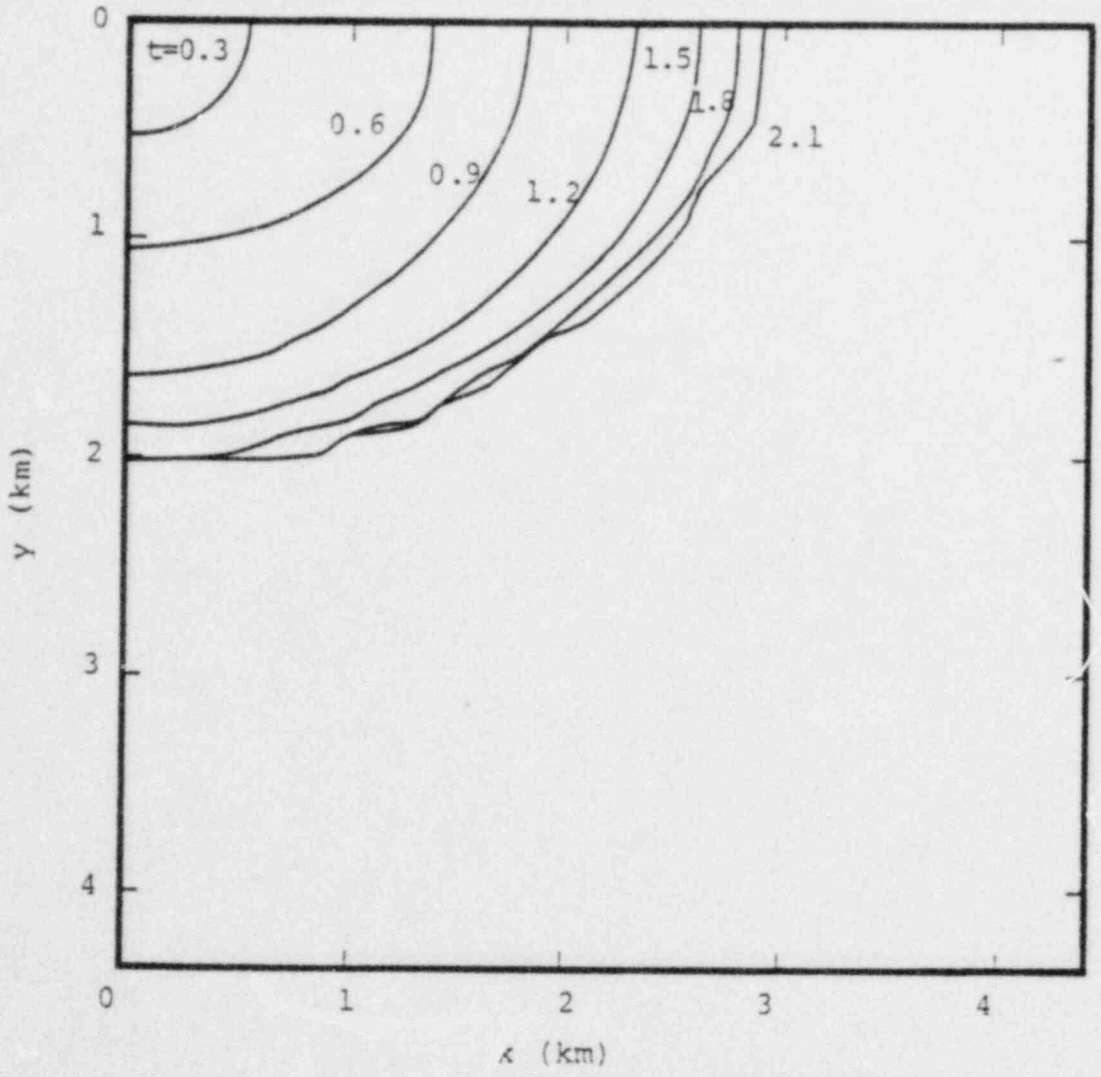

Figure 5.7. Rupture front contours for Case B, at 0.3 second intervals.

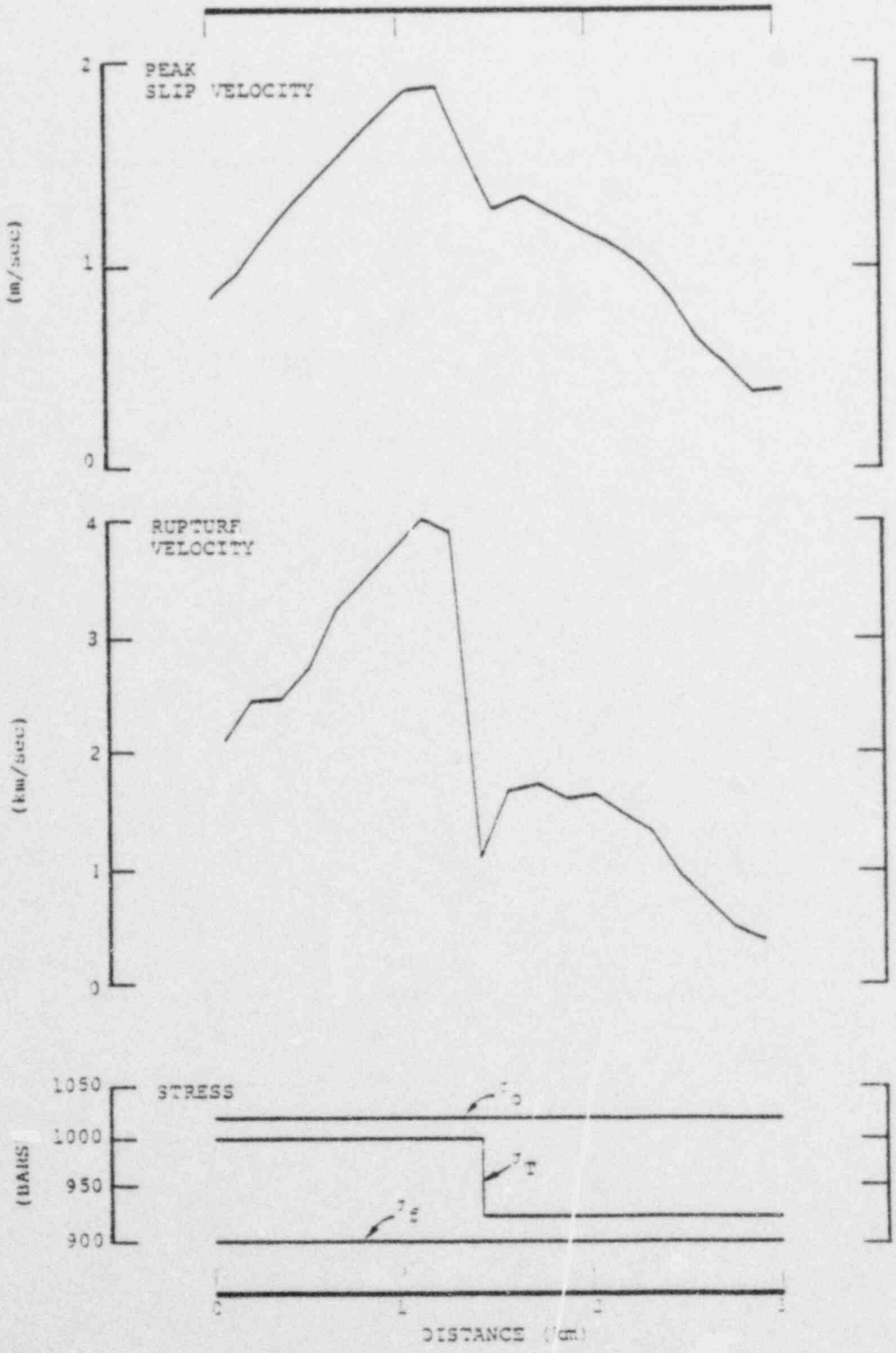

Figure 5.8. Peak slip velocity (low-passed, 5 Hz cutoff) and rupture velocity along the x axis, for Case B.

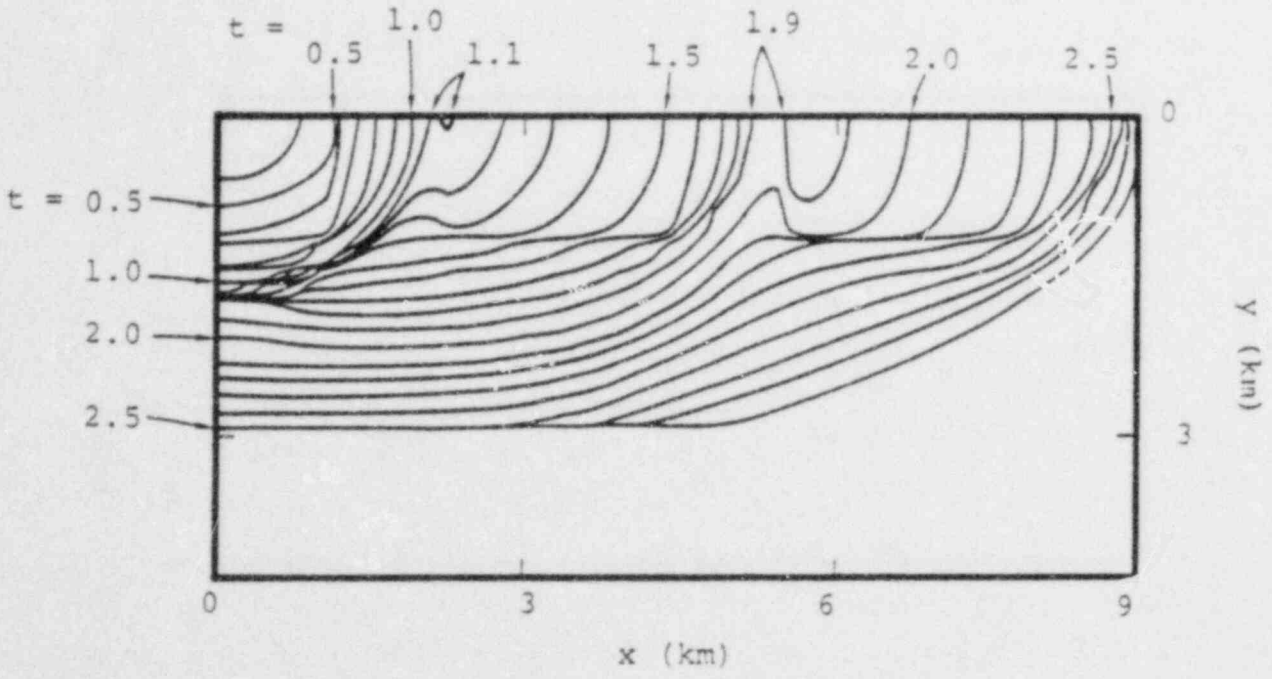

Figure 5.9. Rupture front contours for Case C, at 0.1 second intervals.

speed to about 5 percent below the shear wave speed. This result agrees well with the analyses of Das and Aki (1977) and Andrews (1976), which predict sub-shear rupture velocity when the dynamic stress drop exceeds 2.63 $\Delta\sigma$. It is gratifying that their theoretical predictions, which were based on two-dimensional formulations and uniform stress-drop conditions, are in reasonable accord with the gross average behavior of the three-dimensional, non-uniform stress-drop model.

Figure 5.10 shows slip velocities and rupture velocities along the x axis. The close relationship between slip velocity and rupture velocity is especially visible here. The dashed portions of the rupture velocity curve represent regions that ruptured out of sequence as the rupture front jumped ahead to a high-stress-drop patch.

Also shown in the top section of Figure 5.10 are peak slip velocity as estimated two different ways from Equation (5.1). The line labelled a was obtained using the dimension of the high-stress-drop patches (2.2 km) in place of w in Equation (5.1), and using 100 bars for the value of $\Delta\sigma$ in that equation. Line a seems to be a rather good prediction of peak slip velocity in the high-stress-drop regions. Line b was obtained setting w equal to the overall fault width (6 km) and $\Delta\sigma$ equal to its overall average value (42 bars). This level, in turn, appears to be quite representative of the average value of peak slip velocity. In contrast, Equation (5.2), in terms of dynamic stress-drop, would predict substantially lower peak slip velocities than those shown in Figure 5.10. Using the average rupture velocity of 3.2 km/sec, for example, Equation (5.2) gives the low value of 1.2 m/sec for peak slip velocity. Thus, in the case of non-uniform stress-drop, the spontaneous rupture model continues to support our earlier conclusion that the high-frequency behavior of the slip function scales with $\Delta\sigma$.

5.4 EFFECT OF NON-UNIFORM STRESS-DROP ON FAR-FIELD RADIATION

In Section 4.4, it was noted that the fixed-rupture-velocity model produces near- and far-field acceleration pulses which are

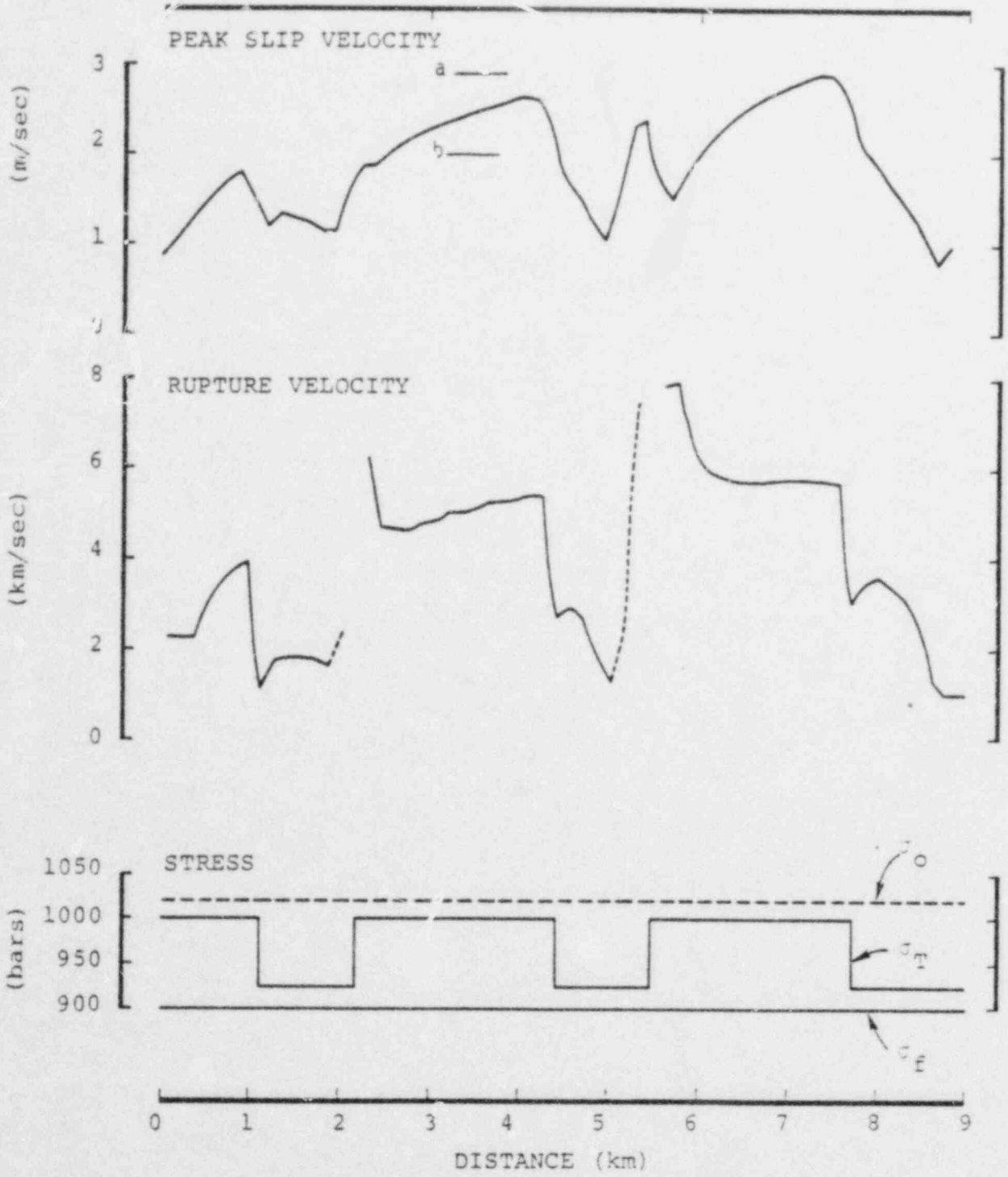

Figure 5.10. Peak slip velocity (low-passed, 5 Hz cutoff) and rupture velocity along the x axis, for Case C. Dashed curves for rupture velocity indicate regions which ruptured out of sequence. For example, rupture occurred at x = 5.6 km while the region between 5.0 and 5.6 km was still intact. The horizontal line labeled a represents peak slip velocity as it would be estimated from Equation 5.1, using 100 bars for $\Delta\sigma$ and the dimension of the high-stress-drop patches (2.2 km) in place of w. The line b was obtained from Equation 5.1 using the actual fault width (6 km) and the average stress-drop (42 bars) in Equation 5.1.

dominated by a few sharp stopping phases. In the spontaneous rupture model, we have relaxed the artificial constraints that rupture growth occur at constant velocity and rupture deceleration at the fault edges be instantaneous. As Figures 5.5 to 5.10 show, when rupture is halted by stress inhomogeneities, rupture deceleration is somewhat spread out in time, and we might expect this mechanism to deemphasize the stopping phases.

Figures 5.11 and 5.12 show far-field accelerations computed from spontaneous rupture cases A and B of Section 5.3. In both cases, acceleration time histories are considerably more complex than in the case of fixed rupture velocity, and thus in better qualitative agreement with strong motion observations (figures 5.11 and 5.12 cannot be directly compared quantitatively with 4.14 and 4.14, however, because the source dimension is considerably smaller for the spontaneous rupture calculations).

Encouraging as this is, we are still faced with the problem of assigning realistic distributions of stress and strength to the fault, and here there may be substantial uncertainty. For example, seismic investigations have suggested that local stress concentrations can lead to stress-drops as high as 500 to 1000 bars over fault dimensions of the order of a few kilometers (for example, Hanks, 1974; Hartzell and Brune, 1979); on the other hand, the average stress-drops for large earthquakes are generally less than 100 bars (Kanamori and Anderson, 1975). Large localized stress-drops undoubtedly would imply large local accelerations, but their importance for surface strong ground motion has not been rigorously examined. Parametric studies of near-field ground motion generation by the spontaneous rupture model are required before we can adequately assess the sensitivity of the model predictions to the model inputs. If the ground motion predictions are highly sensitive to the details of the stress-drop and cohesive stress distributions, then the utility of the model will ultimately depend on constraining these values on the basis of rock mechanics and strong ground motion data.

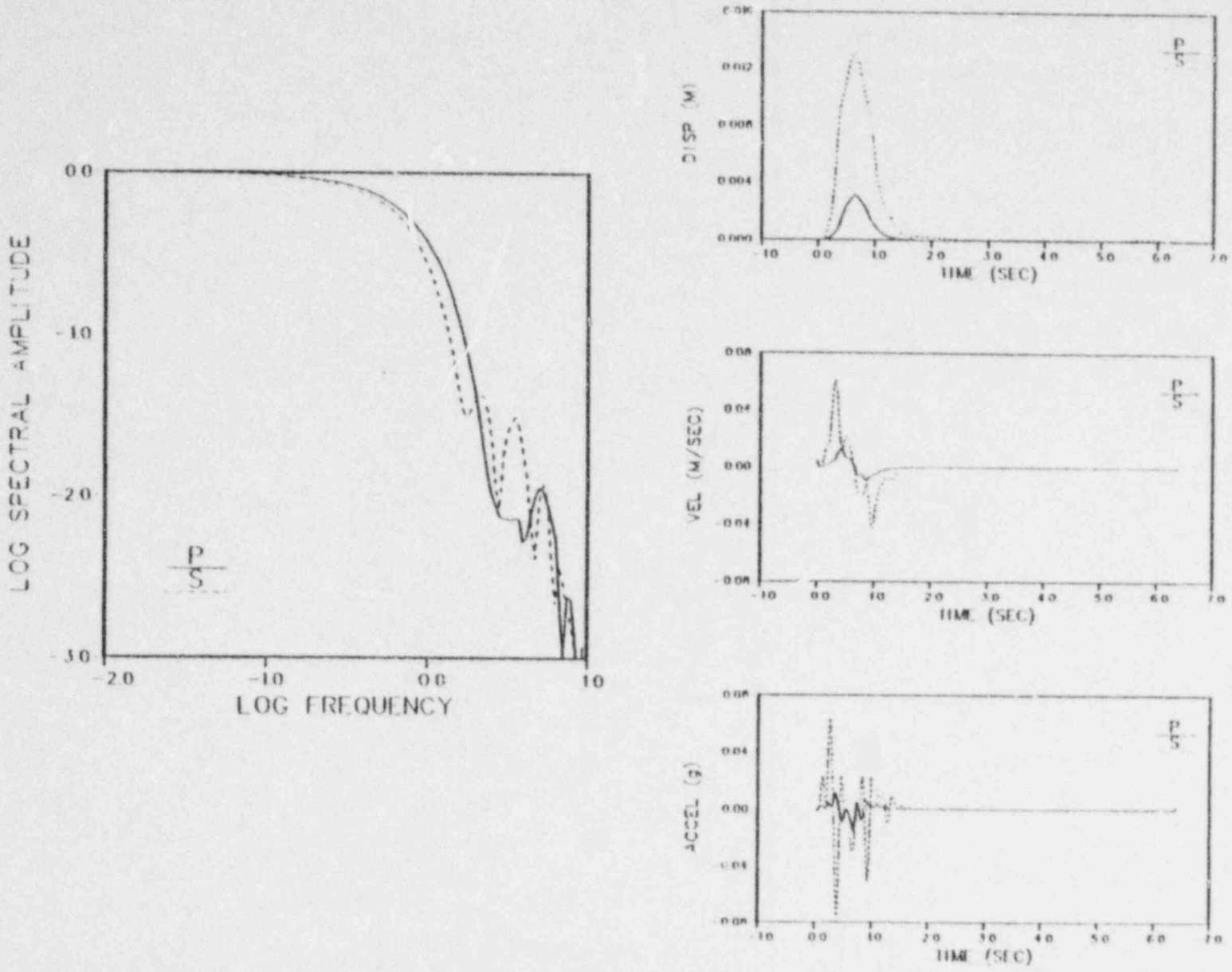

Figure 5.11. Far field displacement, velocity and acceleration pulses and displacement spectra obtained from spontaneous rupture simulation Case A. Observer is at spherical coordinates $\theta = 45$, $\phi = 45$, relative to fault normal, amplitudes are normalized to a hypocentral distance of 10 km, and the double-couple radiation pattern has been factored out.

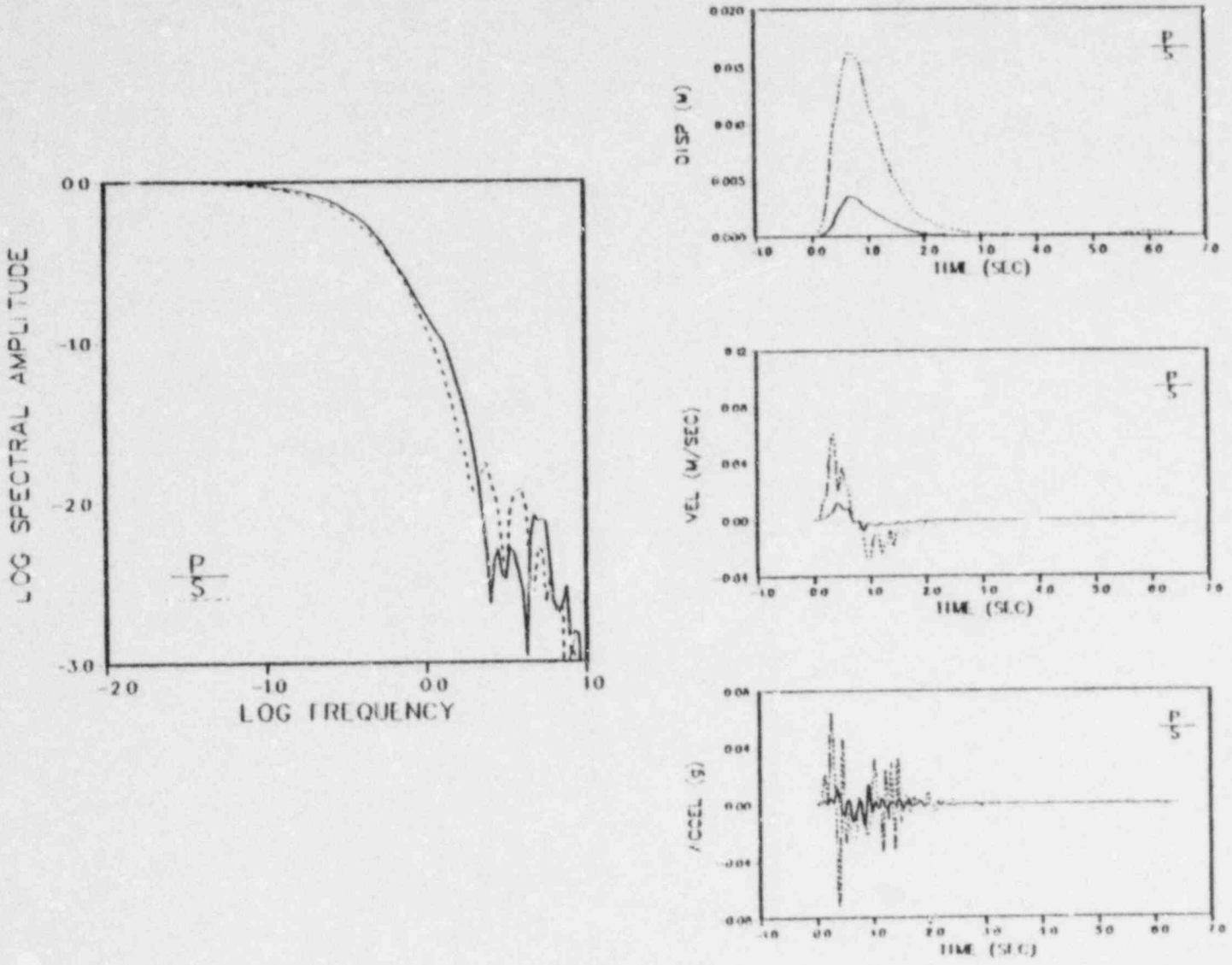

Figure 5.12. Far field displacement, velocity and acceleration pulses and displacement spectra obtained from spontaneous rupture simulation Case B. Observer is at spherical coordinates $\theta = 45$, $\phi = 45$, relative to fault normal, amplitudes are normalized to a hypocentral distance of 10 km, and the double-couple radiation pattern has been factored out.

5.5 CONCLUSIONS

In this chapter we have considered one of the more sophisticated spontaneous-rupture dyramic earthquake models which is currently available. We have examined the dependence of the spatial and temporal distribution of predicted slip on the assumed distribution of stress on the fault, as well as on the mechanism by which rupture is made to stop. The main conclusions from this study are:

1 The high-frequency behavior of the slip functions predicted by the spontaneous-rupture model appear to scale with stress-drop. For the rupture model considered here, Equation 5.1 in terms of stress-drop ("effective stress") is a better approximation to the peak slip velocity than is Equation 5.2, which instead involves dynamic stress-drop. This conclusion may require modification when more advanced constitutive models for the fault zone are developed; future model studies incorporating higher values for the cohesive stress (excess of strength above the prestress) might also result in a modification of this conclusion.

2 When the stress-drop varies spatially on the fault plane, a relatively complex pattern of rupture growth can develop. Rupture accelerates in regions of high stress-drop, decelerates in regions of low stress-drop, and can stop, even if stress-drop is everywhere positive. Even for fairly simple stress configurations, rupture can "jump," leaving unbroken patches, slip at a point can cease and subsequently recommence, and rupture velocity can locally exceed that of P waves (average rupture velocity is, of course, always subsonic). Spatial variations of peak slip velocity and rupture velocity are strongly coupled.

3 Results of spontaneous rupture modeling with spatially varying stress-drop further support the conclusion that high frequencies in the slip function increase with increasing stress-drop. Again, Equation 5.1, interpreted in terms of average stress-drop and fault width, provides a more accurate characterization of the slip function onset than does Equation 5.2.

4 Far-field acceleration pulses computed from the spontaneous-rupture dynamic model are substantially more complex than those computed from the fixed-rupture-velocity dynamic model, and the accelerations are not dominated by a few large stopping phases.

VI. SUMMARY, CONCLUSIONS AND RECOMMENDATIONS

6.1 SUMMARY

This report, together with the first annual report (Swanger et al., 1980) present a summary of the results of a two-year investigation into the applicability of theoretical earthquake source modeling to the definition of design motion environments for nuclear power plants located in the near-field of potentially active faults. The first annual report presented results of a systematic literature search in which various empirical and theoretical models which have been proposed for use in estimating near-field earthquake ground motion parameters were reviewed, compared and evaluated.

During the past year, our research effort has centered on the analysis of various theoretical earthquake models and the characteristics of near-field motion suggested by these models. Our objectives have been to determine the applicability of the models for simulation of near-field ground motions and to assess the uncertainties in applying such models to new situations, that is, to hypothetical design earthquakes which may differ substantially in source characteristics from the recorded earthquakes to which the model was normalized.

Four distinct classes of source models were examined to determine to which features of each source model the near-field high-frequency ground motion is sensitive. In Section II, the characteristics of the near-field ground motion predicted by constant dislocation kinematic models were examined. It was found that the simplest model of this type, employing coherent rupture propagation terminating instantaneously on prescribed boundaries, did not produce reasonable behavior of near-field accelerations. The degree of rupture incoherence together with the mode of rupture stopping, are very important to the nature of high frequency radiation. It was concluded that an important consideration when extrapolating to a larger magnitude is the assumed dependence of the slip function on fault dimension.

In Section III kinematic models of stress concentrations were examined. As in constant dislocation models, coherent, sudden stopping of rupture results in unrealistic near-field ground motion characteristics. When stopping effects are suppressed, these models do predict reasonable spatial variations in near-field accelerations.

Dynamic earthquake models were considered in Section IV and V. Section IV examined dynamic models with uniform stress-drop and prescribed rupture propagation. These models predict that the high-frequency content of the slip function increases with increasing stress-drop ("effective stress"). Also these models predict an increase in the high frequency content of the slip function with an increase of the narrower fault dimension. These models also exhibit a strong dependence of the predicted near-field motions on the prescribed rupture velocity and the sudden termination of rupture propagation.

Dynamic models with spontaneous rupture propagation were examined in Section V. In these models the history of rupture propagation is a direct consequence of the prescribed pre-stress and medium constitutive properties, rather than an a priori input of the model. The rupture growth predicted by these models accelerates in regions of high stress-drop, decelerates in regions of low stress-drop, and can stop spontaneously as a result of stress-drop inhomogeneity. Locally, rupture velocities can be supersonic (greater than the shear velocity). The spontaneous rupture modeling results further support the conclusion that the high-frequency content of the slip function increases with increasing stress-drop.

6.2 CONCLUSIONS

The analysis summarized above has noted several distinct characteristics of theoretical models of earthquakes which affect the high frequency radiation predicted by such models, and these model characteristics must be scrutinized carefully when applying such models to the simulation of motion from a hypothetical design

earthquake. These characteristics are poorly constrained by a lack of current understanding of certain earthquake processes important to high-frequency radiation.

The lack of proper constraints of theoretical model parameters is closely related to similar difficulties with empirical procedures. For example, the near-field data set for magnitudes larger than seven is very sparse and different assumptions about proper extrapolation procedures lead to a highly variable estimate of near-field ground motion levels (Swanger et al., 1980).

By the same token, the magnitude dependence of the slip function theoretical models is not constrained by the data, but there are physical considerations which might constrain such a dependence to some extent. Another difficulty which is common to both empirical approaches and theoretical earthquake modeling involves assumptions as to the inherent similarity of earthquake processes from one event to another. Observational evidence suggests that some events appear to radiate high-frequency energy from a few discrete regions of the fault surface, like the 1971 San Fernando earthquake, while others show little evidence of such features, like the 1966 Parkfield earthquake. One would expect the characteristics of near-field motion to be quite different for these two cases.

Given a theoretical earthquake source model which has demonstrated its ability to reproduce characteristics of the existing near-field data, there are several elements of the model which have some degree of uncertainty when applied to the simulation of ground motion from a hypothetical design earthquake:

1. Rupture history characterization -- It was shown that models with uniform rupture growth which stops instantaneously on a regular boundary are probably not representative of earthquakes in terms of their predicted high-frequency radiation. This observation has been used for justification of incoherent rupture propagation. It is not yet known over what spatial scale earthquake rupture can remain coherent. It may be that some earthquakes have reasonably coherent rupture propagation but the rupture terminates gradually.

2. Slip function characterization -- There are three issues to be addressed concerning the construction of a slip function; whether it should be spatially uniform over the entire fault surface, how it should scale with stress-drop and how it should scale with magnitude.

   a). Spatial uniformity of the slip function -- Dynamic earthquake simulations predict a slip function which is spatially varying. The only case where dynamic simulations suggest some degree of spatial uniformity is the case of long narrow faults for which the predicted high frequency portion of the slip is uniform over much of the fault surface. In such cases, the assumption of a spatially uniform slip function may be reasonable if one is simulating a uniform stress-drop earthquake. In modeling of spatially varying stress-drop sources, this assumption may not be appropriate.

   b). Scaling with stress-drop -- Dynamic earthquake simulations indicate that the high-frequency content of the slip function scales with the stress-drop (i.e., shear prestress minus frictional sliding stress, sometimes called "effective stress"), which in turn is bounded below by the static stress-drop. Dynamic modeling studies performed to date do not support the hypothesis that the spectral content of the slip function, in the frequency range of design importance, is independent of stress-drop and proportional instead to dynamic stress-drop (i.e., rock shear strength minus frictional sliding stress). This conclusion may require modification when more advanced constitutive models for the fault zone are developed; future dynamic model studies incorporating higher values for the cohesive stress (excess of strength above the shear prestress) might also result in a modification of this conclusion.

c.) Scaling with magnitude -- Dynamic simulations predict that the high frequency content of the slip function, for a particular value of stress-drop, should increase with increasing fault width.

3. Uniformity of assumed pre-stress -- Most modeling performed to date has assumed that the characteristics of slip are controlled by some average stress-drop which is representative of the entire fault surface. It has been demonstrated, by means of seismic modeling studies, that some events, notably the 1971 San Fernando earthquake, are clearly not uniform stress-drop events. Such earthquakes have regions where local stress-drops are considerably larger than the average, and the possibility of such circumstances in a hypothetical design earthquake should be considered.

6.3 RECOMMENDATIONS

We recommend that the definition of design motion environments for nuclear power plants located in the near-field of potentially active faults be supported by site-specific computer modeling of earthquake ground motions if the modeling studies satisfy the following conditions:

1. Normalization of the earthquake source model to existing data should include comparisons to strong motion data beyond 20 kilometers distance from the fault. Beyond this distance empirical studies have identified well established trends which a source model, in conjunction with appropriate techniques for simulating wave propragation in stratified media, should duplicate. This normalization can be used as an independent verification of the earth Q (intrinsic attenuation) models used in the simulations.

2. Comparisons of simulated near-field ground motions with recorded strong motion data should include time domain comparisons to verify duration and timing of largest motions. Detailed modeling of observed velocity and displacement time histories is strongly recommended.

3. Quality of fit to observed ground motions should be quantified statistically to assess uncertainties in model normalization.

4. When extrapolating to a hypothetical design earthquake, the principles obtained from dynamic earthquake simulations should be employed. Scaling of the slip properties with stress-drop and fault dimension should be compatible with existing dynamic modeling results, unless support for less conservative scaling can be demonstrated on the basis of improved dynamic modeling studies in conjunction with detailed analysis of strong motion recordings.

5. Possible deviations from the normalized model obtained from comparison to a few events must be considered. Two important considerations are the presence of local regions of higher than average stress-drop and the presence of extensive (dimensions greater than 1 km) regions of coherent rupture propagation.

6. Sensitivity studies should be made on all model parameters which affect the high-frequency response and results of such sensitivity studies should be used to obtain a quantitative estimate of the uncertainties of the model in its application to a site-specific prediction.

7. Ground motion predictions obtained through theoretical modeling should be considered complementary to existing empirical estimates. Substantial differences between empirical and modeling predictions should be justified on a site specific basis and should be supported by independent laboratory and field data.

Given our existing near-field strong motion data set, there are means by which some of the uncertainties in the high-frequency source characteristics can be partially resolved. More emphasis on the analysis of time domain characteristics of strong motion velocities and accelerations may give more detailed information about rupture processes and stress-drop configurations associated with the earthquakes. At present, there are only a few events for which the locations of the origins of recorded high frequency strong motion have been identified. With the computational tools developed

recently for rigorously modeling the seismic response of a stratified geologic structure, the analysis of these earthquakes can certainly be improved upon. This kind of information could also prove valuable for the refinement of empirical procedures. The time domain characteristics should also put bounds on the spatial extents over which coherent rupture can be maintained.

Dynamic earthquake simulations have proved valuable to the construction of reasonable slip function characteristics, but there still remains several unanswered questions which can be addressed by future studies. For example, the effect of material strength on the scaling properties of the slip function should be further quantified. This information, along with the properties of earth materials measured in the laboratory and deduced from seismic observations, may constrain the slip function behavior. Dynamic simulations can also provide an improved understanding of the manner in which earthquake ruptures stop.

As is indicated in Appendix A, the near-field strong motion data sample has recently grown to the point where it can be used as a basis to test at least some of the assumptions implicit in the theoretical source and propagation models. Therefore, it is our recommendation that a program be initiated to use the best avalable dynamic source models in conjunction with the best avalable propagation models to attempt to synthesize the near-field ground motions which have been recorded from a variety of the better-documented recent Western United States earthquakes. The results of such an investigation might well help to narrow the range of credible values of the more important dynamic source parameters and lead to a capability to place reasonable bounds on the types of near-field motions to be expected from future earthquakes on faults of the type considered.

REFERENCES

Aki, K. (1968), "Seismic Displacements Near a Fault," JGR, 73, 5359-5376.

Aki, K. (1979), "Characterization of Barriers on an Earthquake Fault," JGR, 84, 6140-6148.

Aki, K, and P. G. Richards (1980), Quantitative Seismology: Theory and Methods, W. H. Freeman and Company, San Francisco.

Alewine, R. W., III, (1974), "Application of Linear Inversion Theory Toward the Estimation of Seismic Source Parameters," Ph.D Thesis, California Institute of Technology.

Allen, C. R., G. R. Engen, T. C. Hanks, J. M. Nordquist and W. R. Thatcher (1973), "Main Shock and Larger Aftershocks of the San Fernando Earthquake, February 9 - March 1," U.S.G.S Professional Paper 733.

Anderson, J. G. (1974), "A Dislocation Model for the Parkfield Earthquake," BSSA, 64, 671-686.

Andrews, D. J. (1976), "Rupture Velocity of Plane-Strain Shear Cracks," JGR, 81, 5679-5687.

Archuleta, R. J. (1979), "Rupture Propagation Effects in the Coyote Lake Earthquake," EOS, 60, 46, November 13.

Archuleta, R. J. and G. A. Frazier (1978), "Three-Dimensional Numerical Simulations of Dynamic Faulting in a Half-Space," BSSA, 68, 541-572.

Archuleta, R. J. and S. M. Day (1980), "Dynamic Rupture in a Layered Medium: 1966 Parkfield Earthquake," in press, BSSA.

Bache, T. C. and T. G. Barker (1978), "The San Fernando Earthquake - A Model Consistent with Near-Field and Far-Field Observations at Long and Short Periods," Systems, Science and Software Final Technical Report submitted to the U.S.G.S., SSS-R-79-3552, January 1979.

Benioff, H. (1938), "The Determination of the Extent of Faulting with Application to the Long Beach Earthquake," BSSA, 28, 2, 77-84.

Boatwright, J. (1980), "A Spectral Theory for Circular Seismic Sources; Simple Estimations of Source Dimension, Dynamic Stress-Drop and Radiated Seismic Energy," BSSA, 70, 1-28.

Boore, D. M. and M. D. Zoback (1974), "Two-Dimensional Kinematic Fault Modeling of the Pacoima Dam Strong-Motion Recordings of the February 9, 1971 San Fernando Earthquake," BSSA, 64, 555-570.

Bouchon, M (1978), "A Dynamic Source Model for the San Fernando Earthquake," BSSA, 68, 1555-1576.

Bouchon, M. (1979), "Predictability of Ground Displacement and Velocity Near an Earthquake Fault: An Example: The Parkfield Earthquake of 1966," JGR, 84, 6149-6156.

Brune, J. N. (1976), "The Physics of Earthquake Strong Motion" in C. Lomnitz and E. Rosenblueth (ed.), Seismic Risk and Engineering Design, Elsevier Sc. Publ. Co., New York, 141-177.

Brune, J., J. Prince, F. Vernon, E. Mena and R. Simons (1979), "Strong Motion Data Recorded in Mexico for the October 15, 1979, Imperial Valley Earthquake," draft manuscript dated December 21, 1979.

Burridge, R. and J. R. Willis (1969), "The Self-Similar Problem of the Expanding Elliptical Crack in an Anisotropic Solid," Proc. Cambridge Phil. Soc., 66, 443-468.

Canitez, N. and M. N. Toksöz (1972), "Static and Dynamic Study of Earthquake Source Mechanism: San Fernando Earthquake," JGR, 77, 2583-2594.

Cherry, J. T., E. J. Halda and K. G. Hamilton (1976), "A Deterministic Approach to the Prediction of Free Field Ground Motion and Response Spectra from Stick-Slip Earthquakes," Earthquake Engng. and Struct. Dyn., 4, 315-332.

Chopra, A. and P. Chakrabarti (1973), "The Koyna Earthquake and the Damage to Koyna Dam," BSSA, 63, 381-398.

Danlen, F. A. (1974), "On the Ratio of P-Wave to S-Wave Corner Frequencies for Shallow Earthquake Sources," BSSA, 64, 1159-1180.

Das, S. and K. Aki (1977), "Fault Plane with Barriers: A Versatile Earthquake Model," JGR, 82, 5658-5670.

Day, S. M. (1979), "Three-Dimensional Simulation of Rectangular Fault Dynamics," Interim Report prepared for the Institute for Advanced Computation, Systems, Science and Software Report SSS-R-80-4161, September.

Del Mar Technical Associates (1978), "Simulation of Earthquake Ground Motions for San Onofre Nuclear Generating Station Unit 1," Final Report for Southern California Edison Company, submitted for review to the Nuclear Regulatory Commission.

Del Mar Technical Associates (1979), "Simulation of Earthquake Ground Motions for San Onofre Nuclear Generating Station, Unit 1: Supplement I,: report for Southern California Edison Company, submitted for review to the Nuclear Regulatory Commission.

Dillinger, W. H. (1973), "Focal Mechanism of the San Fernando Earthquake" in The San Fernando Earthquake of 2/9/71, U.S. Department of Commerce, NOAA.

Donovan, N. C. (1973), A Statistical Evaluation of Strong Motion Data Including the February 9, 1971 San Fernando Earthquake," paper presented at the Fifth World Conference on Earthquake Engineering, Rome, Italy.

Geller, R. J. (1976), "Scaling Relations for Earthquake Source Parameters and Magnitude," BSSA, 66, 1501-1524.

Gorbunova, I. V., N. V. Kondorakaya, and N. S. Landyneva (1970), "On the Determination of the Extent of an Indian Shock Origin by Kinematic Data," Geophys. J., 20, 457-471.

Guha, S. K., S. P. Agarwal, and P. D. Gosavi (1972), "Accelerogram of Koyna Earthquake of 12/11/67," BSSA, 62, 413-414.

Gupta, H. K., B. K. Rastogi and H. Narain (1971), "The Koyna Earthquake of 12/10/67: A Multiple Seismic Event," BSSA, 61, 167-176.

Gupta, H. K., B. K. Rastogi and H. Narain (1972), "Some Discriminatory Characteristics of Earthquakes Near the Kariba, Kremasta, and Koyna Artificial Lakes," BSSA, 62, 493-508.

Hadley, D. M. and D. V. Helmberger (1980), "Simulation of Strong Ground Motions," BSSA, 70, 617-630.

Hanks, T. C. (1974), "The Faulting Mechanisms of the San Fernando Earthquake," JGR, 79, 1215-1229.

Hanks, T. C. and D. A. Johnson (1976), "Geophysical Assessment of Peak Acceleration," BSSA, 66, 959-968.

Hanks, T. C., J. A. Hileman, and W. Thatcher (1975), "Seismic Moments of the Larger Earthquakes of the Southern California Region," Geological Society of America Bulletin, 86, 1131-1139.

Hartzell, S. H. and J. N. Brune (1979), "The Horse Canyon Earthquake of August 2, 1975 - Two-Stage Stress-Release Process in a Strike-Slip Earthquake," BSSA, 69, 1161-1174.

Harding, S. T. and W. Rinehart (1966), "The Parkfield California Earthquake of June 27, 1966," Preliminary Seismological Report, U.S. Coast and Geodetic Survey.

Haskell, N. A. (1964), "Total Energy and Energy Spectral Density of Elastic Wave Radiation from Propagating Faults," BSSA, 54, 1811-1841.

Haskell, N. A. (1969), "Elastic Displacements in the Near-Field of a Propagating Fault," BSSA, 59, 865-908.

Heaton, T. H. and D. V. Helmberger (1977), "A Study of the Strong Ground Motion of the Borrego Mountain, California, Earthquake," BSSA, 67, 315-330.

Heaton, T. H. and D. V. Helmberger (1978), "Synthesis of San Fernando Strong-Motion Records," Earthquake Notes, 49, No. 1.

Heaton, T. H. and D. V. Helmberger (1979), "Generalized Ray Models of the San Fernando Earthquake," BSSA, 69, 1311-1342.

Ida, Y. (1973), "The Maximum Acceleration of Seismic Ground Motion," BSSA, 63, 959-968.

Jungels, P. H. and G. A. Frazier (1973), "Finite Element Analysis of the Residual Displacements for an Earthquake Rupture: Source Parameters for the San Fernando Earthquake," JGR, 78, 5062-5083.

Kanamori, H. and D. L. Anderson (1975), "Theoretical Basis of Some Empirical Relations in Seismology," BSSA, 65, 1073-1098.

Kawasaki, I. (1975), "On the Dynamic Process of the Parkfield Earthquake of June 28, 1966," J. Phys. Earth, 23, 127-144.

Knopoff, L. (1958), "Energy Release in Earthquakes," Geophys. J., 1, 44-52.

Kostrov, B. V. (1964), "Self-Similar Problems of Propagating Shear Cracks," J. Appl. Math. Mech., 28, 1077-1087.

Langston, C. A. (1978), "The February 9, 1971, San Fernando Earthquake: A Study of Source Finiteness in Teleseismic Body Waves," BSSA, 68, 1-30.

Levy, N. A. and A. K. Mal (1976), "Calculations of Ground Motion in a Three-Dimensional Model of the 1966 Parkfield Earthquake," BSSA, 66, 405-424.

Lighthill, M. J. (1958), Fourier Analysis and Generalized Functions, Cambridge University Press, Cambridge.

Lindh, A. G. and D. M. Boore, (1973), "Another Look at the Parkfield Earthquake Using Strong-Motion Instruments as a Seismic Array," (Abstract) presented at the 68th annual meeting at the Seismological Society of America.

Madariaga, R. (1976), "Dynamics of an Expanding Circular Fault," BSSA, 66, 639-666.

Madariaga, R. (1977), "Modeling of Three-Dimensional Earthquake Faults by Finite Differences," (Abstract) AGU Fall Meeting, San Francisco, December 5-9, 1977.

Madariaga, R. (1978), "The Dynamic Field of Haskell's Rectangular Dislocation Fault Model," BSSA, 68, 868-888.

McEvilly, T. V. (1966), "Parkfield Earthquakes of June 27-29, 1966, Monterrey and San Luis Obispo Counties California-Preliminary Seismic Data, June-July," BSSA, 56, 967-971.

McGarr, A., S. M. Spottiswoods, N. C. Gay and W. D. Ortlepp (1979), "Observations Relevant to Seismic Driving Stress, Stress-Drop and Efficiency," JGR, 84, 2251-2261.

Mikumo, T. (1973), "Faulting Process of the San Fernando Earthquake of February 9, 1971 Inferred from Static and Dynamic Near-Field Displacements," BSSA, 63, 249-264.

Narain, H. and H. Gupta (1968), "Koyna Earthquake," Nature, 217, 1138-1139.

Niazy, A. (1975), "An Exact Solution for Finte, Two-Dimensional Moving Dislocation in an Elastic Half-Space with Application to the San Fernando Earthquake of 1971," BSSA, 65, 1797-1826.

Porcella, R. L. and R. B. Mathhiesen (1979), "Preliminary Summary of the U.S.G.S. Strong-Motion Records from the October 15, 1979, Imperial Valley Earthquake," U.S.G.S. open file report 79-1654.

Porcella, R. L., R. B. Matthiesen, R. D. McJunkin, and J. T. Ragsdale (1979), "Compilation of Strong Motion Records from the August 6, 1979 Coyote Lake Earthquake," California Division of Mines and Geology Preliminary Report 25 and U.S.G.S. Open-File Report 79-385, October.

Richter, C. F. (1958), Elementary Seismology, W. H. Freeman and Co., San Francisco.

Sato, T. and T. Hirasawa (1973), "Body Wave Spectra from Propagating Shear Cracks," J. Phys. Earth, 21, 415-431.

Savage, J. C., R. O. Burford and W. T. Kinoshita (1975), "Earth Movements from Geodetic Measurements, San Fernando Earthquake of February 9, 1971," California Division of Mines and Geology, Bulletin 196.

Scholz, C. H., M. Wyss and S. W. Smith (1969), "Seismic and Aseismic Slip on the San Andreas Fault," JGR, 74, 714-728.

Shannon and Wilson, Inc., and Agbabian Associates (1978), "Data from Selected Accelerograph Stations at Wilshire Boulevard, Century City, and Ventura Boulevard, Los Angeles, California," U.S. Nuclear Regulatory Commission, NUREG/CR-0074.*

Shannon and Wilson, Inc., and Agbabian Associates (1979), "Geotechnical and Strong Motion Earthquake Data from U.S. Accelerograph Stations," U.S. Nuclear Regulatory Commission, NUREG-0029.*

Singh, D. D., B. K. Rastogi and H. K. Gupta (1975), "Surface-Wave Radiation Pattern and Source Parameters of Koyna Earthquake of December 10, 1967," BSSA, 65, 711-732.

Swanger, H. J., J. R. Murphy, T. J. Bennett, and R. Guzman, (1980), "State-of-the-Art Study Concerning Near-Field Earthquake Ground Motion," Systems, Science and Software Annual report prepared for the Nuclear Regulatory Commission SSS-R-80-4217.

TERA Corporation (1978), "Simulation of Earthquake Ground Motions for San Onofre Nuclear Generating Station, Unit 1," submitted to Southern California Edison, May.

Trifunac, M. D. (1972a), "Stress Estimates for the San Fernando, California, Earthquake of February 9, 1971: Main Event and Thirteen Aftershocks," BSSA, 62, 721-750.

Trifunac, M. D. (1972b), "Tectonic Stress and the Source Mechanism of the Imperial Valley, California, Earthquake of 1940," BSSA, 62, 1283-1302.

Trifunac, M. D. (1974), "A Three-Dimensional Dislocation Model for the San Fernando, California, Earthquake of February 9, 1971," BSSA, 64, 149-172.

Trifunac, M. D. and J. N. Brune (1970), "Complexity of Energy Release During the Imperial Valley, California, Earthquake of 1940," BSSA, 60, 137-160.

Trifunac, M. D. and F. E. Udwadia (1974), "Parkfield, California, Earthquake of June 27, 1966: A Three-Dimensional Moving Dislocation," BSSA, 64, 511-534.

Tsai, Y. and K. Aki (1971), "The Koyna, India, Earthquake of December 10, 1967," EOS, 52, p. 277.

Unrnamner, R. A. (1979), "Observations of the Coyote Lake, California, Earthquake Sequence of August 6, 1979," draft manuscript dated October, 1979.

Wesson, R. L., W. H. K. Lee and J. F. Gibbs (1971), "Aftershocks of the Earthquake," U.S.G.S. Professional Paper 733, 24-29.

Whitcomb, J. H. (1971), "Fault-Plane Solutions of the February 9, 1971, San Fernando Earthquake and Some Aftershocks," U.S.G.S. Professional Paper 733, 30-32.

Woodward-Lundgren and Associates (1973), "Geotechnical Data Compilation for Selected Strong Motion Seismograph Sites in California," NOAA, December.

Wyss, M. and T. C. Hanks (1972), "The Source Parameters of the San Fernando Earthquake Inferred from Teleseismic Body Waves," BSSA, 62, 591-602.

*Available for purchase from the National Technical Information Service, Springfield, VA 22161.

APPENDIX A

NEAR-FIELD GROUND MOTION DATA

Although the available near-field ground motion data sample is not complete enough to provide a definitive, empirical data base for engineering design purposes, it does provide the primary basis for assessing the applicability of various theoretical models and for testing competing hypotheses regarding the initiation and propagation of rupture. Table A-1 provides an updated list of earthquake strong motion data recorded in the geometrical near-field; i.e., in an area surrounding the source within a distance approximately equal to the dimensions of the fault rupture. The list consists of 63 observations from 27 different earthquakes covering the magnitude range from 4.5 (Hollister, 1945) to 7.2 (Gazli, 1976). The peak acceleration levels range from 0.05 (Long Beach, 1941) to 1.74 g (Imperial Valley, 1979).

This information, by itself, is of limited utility in choosing between competing theoretical models, because it does not identify many of the common model input parameters. In order to be definitive, it is necessary that the associated source and recording site parameters be known. The following information concerning the source and receiver is of interest:

EARTHQUAKE SOURCE CHARACTERIZATION

- epicenter, focal depth, magnitude
- orientation of fault, extent of rupture surface
- fault plane solution (i.e., sense of motion on fault determined from seismic data)
- determination of seismic moment, stress drop, rupture velocity, direction and nature (i.e., unilateral vs. bilateral) of rupture propagation, etc.

- location and near-surface geology of recording station
- instrumentation.

Complete information on all of the above parameters is available for very few of the earthquakes listed in Table A-1. However, representative data from seven of the better-studied events are presented in Tables A-2 through A-8. It can be seen that even for these few selected events, the amount of available information varies significantly (e.g., 1971 San Fernando versus 1933 Long Beach). Moreover, even for those events which have been extensively studied, the variations in the estimates of the source parameters between different investigators is quite large (cf. Table A-6a). This represents a fundamental limitation which will have to be overcome before a truly adequate near-field prediction capability can be developed.

TABLE A-1

NEAR-FIELD GROUND MOTION DATA SAMPLE

EARTHQUAKE		M	STATION	DISTANCE TO NEAREST FAULT SLIP, km	PEAK ACCELERATION, g
Long Beach	3-11-33	6.3	Public Util. Bsmt.	<5	0.29
Helena, Montana	10-31-35	6.0	Carrol College	<7	0.15
Ferndale	9-12-38	5.5	Ferndale City Hall	≅12	0.14
Imperial Valley	5-19-40	6.4	El Centro	5.5	0.35
Santa Barbara	7-01-40	6.0	Courthouse	≅10	0.24
Long Beach	11-14-41	5.4	Public Util. Bsmt.	<5	0.05
Hollister	5-17-45	4.5	City Hall Basement	<2	0.06
Old Gilroy	3-09-49	5.2	Hollister Library	≅15	0.20
Port Hueneme	3-18-57	4.7		≅10	0.17
San Francisco	3-22-57	5.3	Golden Gate Park	11	0.10
Cienega Rd. Winery	4-08-61	5.6	Hollister City Hall	≅15	0.18
Parkfield	6-27-66	5.5	Station #2	<1	0.49
			Station #5	5	0.43
			Station #8	9	0.28
			Station #12	15	0.06
			Temblor	6	0.35
Koyna	12-10-67	6.5	Koyna Dam	<1	0.62
Lytle Creek	9-12-70	5.4	Lytle Creek	≅12	0.20
San Fernando	2-09-71	6.4	Pacoima Dam	<5	1.17
			8244 Orion	<10	0.26
			15107 Van Owen	<10	0.12
Ancona, Italy	6-14-72	4.9	Rocca	5-6	0.40
Stone Canyon	9-04-72	4.6		8±1-2	0.71
Managua	12-23-72	6.2		5	0.38
Pt. Mugu	2-21-73	6.0		≅20	0.15
Horse Canyon	8-02-75	4.8	Anza Post Office	12	0.13
Oroville	8-06-75	4.7	Oroville Medical Center	11	0.43
			Johnson Ranch	14	0.70

TABLE A-1 (CONT'D)

NEAR-FIELD GROUND MOTION DATA SAMPLE

EARTHQUAKE		M	STATION	DISTANCE TO NEAREST FAULT SLIP,km	PEAK ACCELERATION,g
Friuli, Italy	5-06-76	6.3		≅20	0.36
Gazli	5-17-76	7.2	Karakyr Point	>20	1.30
Santa Barbara	8-13-78	5.1	UCSB North Hall	≅15	0.40
			UCSB Goleta	≅15	0.35
			Freitas Building	≅10	0.23
			Courthouse	≅10	0.20
Coyote Lake	8-06-79	5.9	Gilroy 6	1	0.42
			Coyote Creek	0	0.23
			Gilroy 4	3	0.44
			Gilroy 3	5	0.27
			Gilroy 2	7	0.26
			Gilroy 1	8	0.13
Imperial Valley	10-15-79	6.6	El Centro 6	1	1.74
			El Centro 7	1	0.65
			Aeropuerto	2	0.32
			Bonds Corner	3	0.81
			El Centro 8	4	0.64
			El Centro 5	4	0.71
			El Centro Differential	5	0.93
			El Centro 9	6	0.40
			El Centro 4	7	0.61
			Brawley Airport	7	0.22
			Holtville	8	0.31
			El Centro 10	9	0.23
			Calexico Fire Station	11	0.28
			El Centro 11	13	0.38
			El Centro 3	13	0.27
			Mexicali	13	0.46

TABLE A-1 (CONT'D)

NEAR-FIELD GROUND MOTION DATA SAMPLE

EARTHQUAKE		M	STATION	DISTANCE TO NEAREST FAULT SLIP,km	PEAK ACCELERATION,g
			Cucapah	14	0.31
			Parachute Test Site	15	0.20
			El Centro 2	16	0.43
			El Centro 12	18	0.15
Greenville Sequence	1-24-80	5.5	San Ramon, Eastman Kodak	16	0.15
	1-27-80	5.7	Morgan Territory Park	9	0.27
			Fagundes Ranch	6	0.25

TABLE A-2

LONG BEACH EARTHQUAKE OF MARCH 11, 1933

Origin Time	:	01:54:08 GMT
Epicenter	:	33°34.5'N, 117°59'W
Focal Depth	:	10 km
Magnitude	:	M = 6.3 (Richter, 1958)

Focal Mechanism: The event occurred on the Newport-Inglewood fault which strikes NW in the vicinity of Long Beach. No seismic focal mechanism is available, but historic displacements on this fault have included vertical as well as strike-slip components.

Source Parameters:

Seismic Moment M_o, dyne-cm:

2.0×10^{25} (Hanks et al., 1975)

2.8×10^{25} (Kanamori and Anderson, 1975)

Average Stress-Drop:

~ 8 bars (Kanamori and Anderson, 1975)

Rupture Propagation: No surface faulting was observed for this event and, consequently, the extent of faulting is not well defined. Benioff (1938) estimated that the faulting extended from the focus approximately 27 km in a northwesterly direction with an average rupture velocity of about 4.2 km/sec. Kanamori and Anderson (1975) have estimated the rupture area to be 450 km^2.

Strong Motion Recording: The single near-field strong motion record from this earthquake was measured in the basement of the Long Beach Utilities Building. This building is situated on a thick deposit of sandy soil overlying shale. Near-surface compressional wave velocities and densities have been determined by Woodward-Lundgren and Associates (1973).

TABLE A-3

IMPERIAL VALLEY EARTHQUAKE OF MAY 19, 1940

Origin Time	:	04:36:41 GMT
Epicanter	:	32°42'N, 115°30'W
Focal Depth	:	12 km (TERA, 1978)
Magnitude	:	M_S = 7.1 (Richter, 1958)
		M_L = 6.4 (Trifunac and Brune, 1970)
		M_S = 6.9 (TERA, 1978)

Focal Mechanism: The earthquake occurred on the Imperial fault which is a northwest trending fault of the San Andreas system in southern California.. Recent motion on this fault has been almost pure right lateral strike-slip (Trifunac and Brune, 1970).

Source Parameters:

Seismic Moment M_0, dyne-cm:

1.1 to 1.4 x 10^{26} (Trifunac and Brune, 1970)

2.9 to 4.4 x 10^{25} (Trifunac, 1972b)

5.6 x 10^{26} (Kanamori and Anderson, 1975)

3.0 x 10^{26} (Hanks et al., 1975)

3.6 x 10^{26} (TERA, 1978)

Average Stress-Drop:

~ 90 bars (Kanamori and Anderson, 1975)

Average Slip: 2.7 m (Trifunac, (1972b)

Rupture Propagation: According to Trifunac and Brune (1970), most of the seismic energy radiated from this earthquake was generated by a series of distinct events which propagated SE from the vicinity of the initial epicanter along a 25 km section of the fault. The total length of surface rupture was about 60 km and Kanamori and Anderson (1975) have estimated the rupture area to be 780 km^2.

Strong Motion Recording: The single near-field strong motion recording from this earthquake was measured at the ground level of a two-story building in El Centro. The site is situated on thick alluvium which extends to a depth of at least 300 m (Porcella and Matthiesen, 1979). Detailed geologic, geophysical and dynamic soil properties of the near-surface material at this site have been published by Woodward and Lundgren and Associates (1973) and Shannon and Wilson, Inc. and Agbabian Associates (1978).

TABLE A-4

PARKFIELD EARTHQUAKE OF JUNE 28, 1966

Origin Time	:	04:26:13.4 GMT
Epicenter	:	35°37'N, 120°30'W
Focal Depth	:	5 km (Harding and Rinehart, 1966)
Magnitude	:	M_L = 5.5 (Berke'
		M_L = 5.8 (Pa -na)
		M_S = 6.5 (Palisades)
		m_b = 5.3 (USGS)

Focal Mechanism: The P wave first motion data indicate right lateral strike-slip on a plane which strikes about N30°W and dips about 80°SW (McEvilly, 1966). This agrees with the strike of the observed surface cracking and with the local strike of the San Andreas fault zone.

Source Parameters:

Seismic Moment M_o, dyne-cm:

1.4×10^{25} (Aki, 1968)

1.9×10^{25} (Scholz et al., 1969)

4.4×10^{25} (Trifunac and Udwadia, 1974)

3.9×10^{25} (TERA, 1978)

Average Stress-Drop: 24 bars (TERA, 1978)

Average Slip:

60 cm (Aki, 1968)
30 cm (Scholz et al., 1969)
93 cm (Haskell, 1969)
25 cm (Anderson, 1974)
200 cm (Levy and Mal, 1976)

Rupture Propagation: A wide variety of rupture models have been proposed for this event. For example, Haskell (1969) used a fault

length of 19.8 km, a fault width of 2.48 km and a unilateral dislocation velocity of 2.2 km/sec while Anderson (1974) defined a bilateral rupture spreading 5 km NW and 33 km SE from the epicenter at a propagation velocity between 2.8 and 3.0 km/sec. Others such as Trifunac and Udwadia (1974) and TERA (1978) have proposed more complex faulting models for this event, consisting of several separate planes with different orientations.

Strong Motion Recordings: As is indicated in Table A-1, five near-field strong motion recordings were obtained from this event. All the stations appear to be sited on unconsolidated materials of varying thickness. Detailed geologic, geophysical and dynamic soil properties of the near-surface materials at these sites have been published by Woodward Lundgren and Associates (1973) and Shannon and Wilson, Inc., and Agbabian Associates (1978).

TABLE A-5

KOYNA EARTHQUAKE OF DECEMBER 10, 1967

Origin Time	:	21:31:17 GMT
Epicanter	:	17°31.1'N, 73°43.9'E
Focal Depth	:	10 km (Singh et al., 1975)
		12 km (Guha et al., 1971)
Magnitude	:	M_S = 6.3 (Singh et al, 1975)
	:	M_S = 6.2 (Narain and Gupta, 1968)
	:	M_S = 6.5 (Gorbunova et al., 1970)
		m_b = 6.0 (USCGS)

Focal Mechanism: A large number of solutions have been derived from various components of the seismic motion recorded from this event. The consensus of these studies appears to favor left-lateral strike slip faulting on a vertical fault plane striking approximately N-S (Singh et al., 1975)

Source Parameters:

Seismic Moment M_o, dyne-cm:

8.2×10^{25} (Singh et al., 1975)

1.8×10^{26} (Tsai and Aki, 1971)

Average Stress-Drop: 6 to 20 bars (Singh et al., 1975)

Average Slip, cm:

108 (Singh et al., 1975)
40 (Tsai and Aki, 1971)

Energy Release: 2.25×10^{21} ergs (Singh et al., 1975)

Rupture Propagation: Gupta et al., (1969, 1971) and Singh et al., (1975) estimated that the rupture propagated southward from the hypocenter over a 40 km segment of the fault plane. The average rupture propagation velocity was determined to lie in the range from 3.0 to 3.4 km/sec (Gupta et al., 1969; 1971).

Strong Motion Recording: The strong motion record was measured in a gallery of the Koyna Dam (Chopra and Chakrabarty, 1973). The dam is situated on the volcanic basalt rocks of Peninsular India known as the Deccan Traps. The lava flows are alternated by thin layers of trap ash or red boles.

TABLE A-6

SAN FERNANDO EARTHQUAKE OF FEBRUARY 9, 1971

Origin Time	:	14:00:41.8 GMT
Epicenter	:	34°24.7'N, 118°24'W (Allen et al., 1973)
		34°27'N, 118°24'W (Hanks, 1974)
Focal Depth	:	8.4 km (Allen et al., 1973)
		13 km (Hanks, 1974)
		14 km (Canitez and Toksoz, 1972)
Magnitude	:	M_L = 6.4 (Allen et al., 1973)
		M_S = 6.5 NOAA
		m_b = 6.2 MOAA

Focal Mechanism: According to Allen et al., (1973), the faulting during this earthquake corresponded to displacement on a thrust fault or zone of thrust faults dipping about 35° and striking about N70°W. The first motion data indicates that the initial rupture occurred along a plane striking about N65°W and dipping about 55° to the northeast (Dillinger, 1971; Whitcomb, 1971).

Source Parameters: A very large number of determinations of dislocation parameters have been made for this event. Some representative values are given in Table A-6a.

Rupture Propagation: Most investigators have concluded that the rupture surface is segmented, with a lower surface dipping at an angle of about 50° at depths below about 8 km and an upper surface dipping at an angle of about 30° and extending from the surface down to a depth of about 8 km (e.g., Bouchon, 1978; Niazy, 1975; Bache and Barker, 1978; Hanks, 1974). Furthermore, it is generally agreed that the earthquake initiated with a high stress drop event on the lower fault surface and propagated upward and southward toward the free surface. As is indicated in Table A-6a, the average rupture velocity has been estimated to lie in the range of 1.5 to 2.8 km/sec.

Strong Motion Recordings: More than 100 strong motion systems were triggered by this earthquake. However, as is indicated in Table A-1, only three of these are near-field according to the definition used in this appendix. The well-known Pacoima Dam recording was made on hardrock on the abutment to the dam. The other two sites, situated in the San Fernando Valley, were located on alluvium, the thickness of which exceeds 200 m at both sites. Detailed subsurface geologic and geophysical profiles have been determined for these sites and reported by Woodward-Lundgren and Associates (1973).

TABLE A-6a

ESTIMATED SOURCE PARAMETERS FOR THE 1971 SAN FERNANDO EARTHQUAKE

SOURCE OF DATA	STRIKE (deg)	DIP (deg)	AREA (km^2)	AVERAGE SLIP (cm)	SEISMIC MOMENT M_o (dyne-cm)	AVERAGE STRESS DROP (bars)	AVERAGE RUPTURE VELOCITY (km/sec)
Wesson et al. (1971)	N72W	50	440				
Wyss (1971)			1400	31	1.9×10^{26}		
			180	240	1.3×10^{26}		
			460	100	1.4×10^{26}	30	
Trifunac (1972a)			320	150	1.5×10^{26}	60	2.0
Canitez and Toksoz (1972)	N70W	52			0.75×10^{26}		
	N70W	52					
	N67W	52	196	280	1.64×10^{26}	70	
Savage et al. (1975)	N80W	45	120	283	1.0×10^{26}		
Wyss and Hanks (1972)			708	22	0.47×10^{26}	6	2.5
			440	67	0.88×10^{26}	21	
			440	100	1.3×10^{26}	34	
Mikumo (1973)	N64W	50	255	140	1.1×10^{26}	40	2.0
	N70W	52				65	2.5
Jungels and Frazier (1973)					6×10^{25}	24	
Trifunac (1974)	N72W	40	130	393	1.53×10^{26}		2.0

TABLE A-5a (CONT'D)

ESTIMATED SOURCE PARAMETERS FOR THE 1971 SAN FERNANDO EARTHQUAKE

SOURCE OF DATA	STRIKE (deg)	DIP (deg)	AREA (km^2)	AVERAGE SLIP (cm)	SEISMIC MOMENT M_o (dyne-cm)	AVERAGE STRESS DROP (bars)	AVERAGE RUPTURE VELOCITY (km/sec)
Boore and Zoback (1974)				100			1.86 2.5
Hanks (1974) (Initial Event)	N67±6W	52±3	28-113	4.6 9.2	1.7-.85 $\times 10^{26}$	350 1400	2.8
Niazy (1975)			400	100			1.5 2.5
Langston (1978)	N70±8W	53	230	110	.86±.33 $\times 10^{26}$		1.8
Bouchon (1978) (Initial Event)			7.07	250	3.5×10^{24}	460	2.0
Heaton and Helmberger (1978)					1×10^{26}		1.8
Bache and Barker (1978) (Initial Event)						600	

TABLE A-7

COYOTE LAKE EARTHQUAKE OF AUGUST 6, 1979

Origin Time	:	17:05:22.3 GMT
Epicenter	:	37°t.t'N, 121°31.8'W
Focal Deptn	:	9.6 km
Masgnitude	:	M_L = 5.9 (Uhrhammer, 1979)

Focal Mechanism: The earthquake occurred on the Calaveras fault. The focal mechanism as deduced from the first motion data indicates right-lateral strike slip on a vertical fault plane striking N27°W, in agreement with the observed orientation of the Calaveras fault in this area (Uhrhammer, 1979).

Source Parameters: (Uhrhammer, 1979)

Seismic Moment M_0: 6×10^{24} dyne-cm

Average Stress-Drop: ~ 9 bars

Average Slip: ~ 21 cm

Rupture Propagation: Discontinuous surface faulting was observed along a 14.4 km length of the Calaveras extending southeastward from a point about 6 km southeast of the epicenter (Archuleta, 1979). Thus, the total rupture length is estimated to have been about 20 km. The strong motion data has been interpreted to point to the fact that the rupture propagated unilaterally from the epicenter southeast toward the Gilroy strong motion instrument array (Archuleta, 1979).

Strong Motion Recordings: Six near-field stations recorded this earthquake. Of these, three are on rock sites (Coyote Lake, Gilroy 1 and Gilroy 6) and three are on alluvium sites (Gilroy 2, 3 and 4). Reflection surveys and downhole shear wave velocity studies are currently being conducted to determine the subsurface conditions at each of the Gilroy array stations.

TABLE A-8

IMPERIAL VALLEY (CALEXICO) EARTHQUAKE OF OCTOBER 15, 1979

Origin Time	:	23:16:54.3 GMT
Epicenter	:	32°38.6'N, 115°18.7'W
Focal Depth	:	5.9 km
Magnitude	:	M_L = 6.6
		M_S = 6.8

Focal Mechanism: This earthquake occurred on the same northwest trending Imperial fault which ruptured during the May 19, 1940 event. The sense of motion on this fault is predominantly right-lateral strike slip.

Source Parameters: (McNally, 1979)

Seismic Moment M_0: 6 x 10^{25} dyne-cm

Average Slip: 40 cm

Rupture Propagation: The rupture apparently propagated northwestward from the hypocenter in a unilateral mode. The length of observed surface rupture was approximately 30 km (McNally, 1979).

Strong Motion Recordings: Twenty of the strong motion instruments which were triggered (including 3 in Mexico) by this event are in the near-field according to the criterion used in this Appendix. As can be seen from Table A-1, this makes this earthquake the best documented event to date with regard to near-field ground motion characteristics. According to Brune et al., (1980) none of the three Mexican stations listed in Table A-1 was located on rock. Porcella et al., (1979) specify site geology for only six of the 17 North American stations in Table A-1 and each of these is characterized as being situated on more than 300 m of alluvium. Determination of detailed geological and geophysical profiles of these sites is in progress.

APPENDIX B

HIGH-FREQUENCY FOURIER AND RESPONSE SPECTRA OF SLIP FUNCTIONS

Each of the slip functions considered in Section 4 has singular behavior, near $\tau = 0$, of the form

$$s(\tau) \sim A\tau^{\alpha} H(\tau) \tag{B.1}$$

The high-frequency asymptotic Fourier spectrum of $\dot{s}$ is (Lighthill, 1958, p. 52)

$$\left|\overset{\tau}{s}(f)\right| \sim (2\pi)^{-\alpha} \alpha A \Gamma(\alpha) f^{-\alpha} \tag{B.2}$$

The zero-damping response spectrum of $\dot{s}$ can also be obtained analytically, when the oscillator period T_o is less than the slip rise time τ_R. The undamped oscillator response, prior to $t = \tau_R$, is

$$u(t) = \frac{\alpha A}{(2\pi)^{1+\alpha}} \theta_{\alpha}(2\pi t/T_o) T^{1+\alpha} \tag{B.3}$$

in which the time dependence θ_{α} is

$$\theta_{\alpha}(x) = \sin x \int^{x} \frac{\cos y}{y^{1-\alpha}} dy - \cos x \int_{0}^{x} \frac{\sin y}{y^{1-\alpha}} dy$$

$$= x^{1+\alpha} \sum_{n=0}^{\infty} C_n x^{2n} \tag{B.4}$$

The C_n satisfy the recursion relation

$$C_{-1} = -1$$

$$C_n = \frac{-C_{n-1}}{(\alpha+2n)(\alpha+2n+1)} \tag{B.5}$$

The pseudo-velocity response spectrum $V(T_o)$ is thus

$$V(T_o) = \alpha A (2\pi)^{-\alpha} \left\| \theta_\alpha \right\| T^\alpha, \tag{B.6}$$

where $\left\| \theta_\alpha \right\|$ represents the peak absolute value attained by $\theta_\alpha(x)$. In practice, the form of $\theta_\alpha(x)$ is such that Equation is valid for T_o less than about $2\tau_R$.

Dynamic Slip Function. In this case,

$$A = \frac{C\Delta\sigma}{\rho\beta}\sqrt{\frac{2W}{V_R}} \quad ,$$

$$\alpha = \frac{1}{2}$$

$$\left\| \theta_\alpha \right\| = 2.38$$

so that $\left| \bar{\dot{S}} \right|$ and V are, respectively,

$$\left| \bar{\dot{S}}(f) \right| \sim \frac{C\Delta\sigma}{2\rho\beta}\sqrt{\frac{W}{V_R}}\, f^{-1/2} \tag{B.7}$$

$$V(T_o) \sim \frac{0.95 C\Delta\sigma}{2\rho\beta}\sqrt{\frac{2W}{V_R}}\, T_o^{1/2} \tag{B.8}$$

Ramp Slip Function. In this case,

$$A = V_o$$

$$\alpha = 1$$

$$\left\| \theta_\alpha \right\| = 2.0$$

so that $\left| \bar{\dot{S}} \right|$ and V are, respectively,

$$\left|\bar{s}(f)\right| \sim \frac{V_o}{2\pi} f^{-1} \qquad (B.9)$$

$$V(T_o) \sim \frac{V_o}{\pi} T \quad . \qquad (B.10)$$

TERA/DELTA Slip Function. This slip function has three parameters, s_∞, τ_R, and V_o; α and A are given by

$$\alpha = \frac{\ln\left[\frac{s_\infty}{\Delta t V_o}\right]}{\ln\left[\frac{\tau_R}{\Delta t}\right]}$$

$$A = \Delta t^{1-\alpha} V_o \ ,$$

where Δt is the time step used to discretize the problem. In all modeling studies reported using this slip function, Δt has been set to 0.025 seconds. As a result of this choice, the Nyquist frequency in these studies is 20 Hz, and the discretization has an important effect on the spectrum of the slip velocity. The slip velocity function is the first difference of Equation B.1, so we have to introduce the factor $\sin(\pi\Delta tf)/(\pi\Delta tf)$ into Equation B.2 for the Fourier spectrum of the slip velocity. Also, the factor $\sin(\pi\Delta t/T_o)/(\pi\Delta t/T_o)$ is an excellent approximation to the discretization effect on the undamped response spectrum of the slip velocity; this is intuitively apparent, and can be verified by comparison with the numerically computed slip function response spectra given by Del Mar Technical Associates (1979). This leads to the following expressions for $\left|\bar{s}\right|$ and V:

$$\left|\bar{s}(f)\right| \sim (2\pi)^{-\alpha}\alpha A\,\Gamma(\alpha)\,[\sin(\pi\Delta tf)/(\pi\Delta tf)]f^{-\alpha} \qquad (B.11)$$

$$V(T_o) \sim (2\pi)^{-\alpha}\alpha A\left[\frac{\pi\Delta t}{T_o}\sin\left(\frac{\pi\Delta t}{T_o}\right)\right]\left\|\theta_\alpha\right\| T^\alpha \quad . \qquad (B.12)$$

For the TERA/DELTA slip function used in the San Onofre modeling study (Del Mar Technical Associates, 1979), $\alpha = 0.394$, $A = 0.855$, and $\|\theta_\alpha\| = 2.81$.

NRC FORM 335 (7.77) U.S. NUCLEAR REGULATORY COMMISSION

BIBLIOGRAPHIC DATA SHEET

1. REPORT NUMBER (Assigned by DDC)
NUREG/CR-1978

4. TITLE AND SUBTITLE (Add Volume No., if appropriate)
State-of-the-Art Study Concerning Near-Field Earthquake Ground Motion

2. (Leave blank)

3. RECIPIENT'S ACCESSION NO.

7. AUTHOR(S)
H.J. Swanger, S.M. Day, J.R. Murphy, & R. Guzman

5. DATE REPORT COMPLETED
MONTH: December YEAR: 1980

9. PERFORMING ORGANIZATION NAME AND MAILING ADDRESS (Include Zip Code)
Systems, Science and Software
P.O. Box 1620
LaJolla, California 92038

DATE REPORT ISSUED
MONTH: March YEAR: 1981

6. (Leave blank)

8. (Leave blank)

12. SPONSORING ORGANIZATION NAME AND MAILING ADDRESS (Include Zip Code)
Division of Reactor Safety Research
Office of Nuclear Regulatory Research
U.S. Nuclear Regulatory Commission
Washington, DC 20555

10. PROJECT/TASK/WORK UNIT NO.

11. CONTRACT NO.
FIN B6491
NRC-03-78-155

13. TYPE OF REPORT
Final Technical Report

PERIOD COVERED (Inclusive dates)
Sept., 1978 - Oct., 1980

15. SUPPLEMENTARY NOTES

14. (Leave blank)

16. ABSTRACT (200 words or less)

This report presents a summary of an investigation into the applicability of theoretical earthquake source modeling to the definition of design ground motion environments for nuclear power plants located in the near-field of potentially active faults. A variety of theoretical source models are examined to determine the characteristics of near-field ground motion predicted by such models and to isolate the sensitivities of high-frequency radiation characteristics to specific elements of the models. It is concluded that the high frequency ground motions predicted by the models are quite sensitive to particular details of implementation for which data and theory provide rather poor constraints. Examination of dynamic earthquake models suggests guidelines for extrapolation of model parameters to new stress-drops and magnitudes which are contrary to those procedures already in use. Guidelines for future modeling efforts which may better quantify the uncertainties in such procedures are recommended. Also recommended are studies which may offer constraints useful for both empirical and theoretical modeling procedures.

17. KEY WORDS AND DOCUMENT ANALYSIS

17a. DESCRIPTORS

17b. IDENTIFIERS/OPEN-ENDED TERMS

18. AVAILABILITY STATEMENT
Unlimited

19. SECURITY CLASS (This report)
Unclassified

21. NO. OF PAGES

20. SECURITY CLASS (This page)
Unclassified

22. PRICE
$